TECHNISCHE UNIVERSITÄT MÜNCHEN
Fakultät für Chemie
Lehrstuhl I für Technische Chemie

Reaction engineering and hydrodynamics of a rotor-stator spinning disc reactor

Julia Simone Daniela Kleiner

Vollständiger Abdruck der von der Fakultät für Chemie der Technischen Universität München zur Erlangung des akademischen Grades eines

Doktor-Ingenieurs (Dr.-Ing.)

genehmigten Dissertation.

Vorsitzender:	Hon.-Prof. Dr. Richard W. Fischer
Prüfer der Dissertation:	1. Prof. Dr.-Ing. Kai-Olaf Martin Hinrichsen
	2. Prof. Dr.-Ing. Harald Klein

Die Dissertation wurde am 09.01.2019 bei der Technischen Universität München eingereicht und durch die Fakultät für Chemie am 24.05.2019 angenommen.

Acknowledgments

I would like to thank Prof. Dr.-Ing. Kai-Olaf Hinrichsen for giving me the opportunity to work at his chair for the last couple of years, but more importantly I am grateful for the trust he put in me, the advice he gave when needed and the experience I could gain working within his research group and presenting research results on conferences.

Special thanks go to Prof. Dr. Richard Fischer for taking the chairmanship of my examination and to Prof. Dr.-Ing. Harald Klein for agreeing to be my second examiner. Also, I want to thank him for the support I could always find at his chair and for letting me be part of the APT family.

I want to express my gratitude to Heidi Holweck and Thomas Michel. Already during my studies I could count on Heidi's support and turn to her for help. I want to thank Thomas for basically being everybody's mentor, his constant interest in the spinning disc technology expressed at our biannual seminars and the interesting discussions at the morning coffee rounds or barbecues.

What I cherished during my time at the TC1 was the amazing group of colleagues and their team spirit. I always got help in the lab from either Franz, Moritz, Stefan, Thomas or Chris, with modeling issues from Flo, Johanna, Philipp, Sebastian and Daniel and all other problems and moral support when I needed it, which I am very thankful for; especially, I want to thank my office neighbors for their constant openness for discussion and the constructive and fun working atmosphere over the past couple of years. When I started at the TC1, I was very lucky to take over the reactor from Franz who really took his time to show me everything about the setup, get to know the spinning disc technology and he was always open to discuss any research questions I had on the topic, which I want to thank him for.

While I was at the TC1, I had many students working with me and I am grateful for their excellent work and personal effort; especially, I want to thank Christoph, Tatjana, Tobias, Korbinian, Benjamin, Felix, Markus, Amelie and Laura.

Working in the lab I was always dependent on functioning equipment, which is why I want to thank the team of the mechanics and electronics workshop, especially Michael Widhopf, for their support over the years.

While I was studying in Munich I got to know some very good friends, whom I want to thank for always being there and sharing the experience at the university, be it learning together or having fun at various undertakings.

Last but not least, I want to thank my family. I am grateful that my parents supported me when I went to Munich for my studies and I am very lucky that I grew up with two wonderful sisters, who, even though we did not see each other as much anymore over the last couple of years, were always there for me. Going to Munich was maybe the best decision I ever made, as it let me to meeting my husband and getting a second family who has welcomed me with open arms and supported Thomas and me a lot. My most profound thank goes to Thomas and I simply want to thank him for everything.

Abstract

Considering the challenges in energy production and environmental protection the world faces today, the term process intensification (PI) has strongly gained in importance in today's industrial applications. One innovative technology engineered within the scope of PI is the rotor-stator spinning disc reactor (RSSDR). Although several studies on this reactor type have already been conducted for a fundamental characterization, the RSSDR is still a young technology, the properties of which in terms of mixing, mass and heat transfer, etc., are not fully understood. It is rarely found in industrial applications; this is unfortunate, as the RSSDR presumably holds great process-intensifying potential for a variety of applications, but being a new technology it carries risks making it unattractive for industry so far. Therefore, a further characterization of the RSSDR's basic properties and its process-intensifying potential of industrially relevant reaction systems is essential.

In this thesis, an RSSDR was investigated in terms of reaction engineering and hydrodynamics, by means of studying the heat transfer properties via an experimental and a numerical approach. The latter involved the simulation of the flow behavior in the regarded reactor gap, before simulating the conjugate heat transfer of an RSSDR model. Moreover, the potential of the regarded RSSDR for intensification of a strongly exothermic reaction involving mixing of two immiscible fluids, i.e., the epoxidation of methyl oleate (MO) with hydrogen peroxide and formic acid, was studied.

In the experimental heat transfer study, the influence of rotational disc speed, dimensionless throughput, Prandtl number and the aspect ratio on the single-phase stator-side heat transfer in an RSSDR was examined. An increase in either one of the studied parameters leads to an increase in the stator-side Nusselt number for the selected parameter range. A laminar and a turbulent flow regime with respect to the rotational Reynolds number was observed, which coincides with a throughput- and a rotation-governed heat transfer regime, respectively. The experimental data was used to establish a Nusselt number correlation for the turbulent regime in dependence of the rotational Reynolds number, dimensionless throughput, Prandtl number and aspect ratio, which represents the data within 20 % accuracy. A significant intensification of the stator-side heat transfer coefficient and, as a consequence thereof, the overall volumetric heat transfer coefficient was observed by means of increasing the rotational disc speed of the RSSDR. The determined overall volumetric heat transfer coefficients are twice as high as the ones

measured at comparable conditions in a similar RSSDR setup, which are already more than five times higher than overall volumetric heat transfer coefficients of conventional tube reactors.

As the experimental investigation of the heat transfer in an RSSDR does not allow to easily regard local temperature fields and derive radially resolved heat transfer coefficients, and because experiments are expensive in labor, a numerical approach was pursued. A computational fluid dynamics study of the flow properties in the rotor-stator gap was performed using OpenFOAM®. A turbulence model study of different Reynolds-averaged Navier−Stokes (RANS) turbulence models revealed the *Lien-Leschziner* model to best describe the turbulent flow in the reactor gap simplified as a two-dimensional axisymmetric (2.5D) geometry for the studied parameter range. The cold-flow simulations were subsequently used in the simulation of the heat transfer of the studied RSSDR model with a modified heat transfer solver for conjugate heat transfer, which allows to consider dissipative power inputs. The radial and axial temperature distributions derived from the simulations are in qualitative agreement with literature. From the temperature fields, local stator-side heat transfer coefficients were determined, which increase with a rise in rotational disc speed and throughput, whereat the throughput influence ceases at higher radii. Area-averaged heat transfer coefficients were derived and compared to the experimental results of the first study of this thesis for validation, which showed good agreement; the study shows the possibility of characterizing hydrodynamics and heat transfer of an RSSDR by means of a 2.5D model geometry using a RANS approach for turbulence modeling in OpenFOAM®.

In a last study of this thesis, the intensification of the epoxidation of MO with hydrogen peroxide and formic acid carried out in an RSSDR was investigated in dependence of rotational disc speed, throughput and temperature with and without a catalyst-coated rotor disc. Optimum values with respect to either one of the studied parameters were found for the operation of the reaction in an RSSDR carried out in a semi-batch mode with recycle. Although the used catalyst yielded no beneficial results under the studied experimental conditions, a significant increase in epoxide yield and MO conversion was observed for the RSSDR in comparison to batch experiments carried out as benchmark. Average epoxide production rates were determined from the RSSDR and comparative batch experiments, which revealed that the RSSDR yields reaction rates which are four times the ones measured for the benchmark batch experiments. Comparing the reaction rates of the RSSDR of this study with literature results, the RSSDR matches and outperforms reaction rates of comparable reaction systems of microreactors found in literature; thus, it could be demonstrated that the RSSDR allows a distinct intensification of the epoxidation reaction due to its excellent mass transfer properties and up to a certain disc speed its eminent heat transfer characteristics.

Kurzzusammenfassung

Der Begriff Prozessintensivierung (PI) hat in Anbetracht der Herausforderungen bei der Energieerzeugung und dem Umweltschutz, denen sich die Welt gegenübersieht, in heutigen Industrieanwendungen stark an Relevanz gewonnen. Eine innovative Reaktortechnologie, die im Rahmen der PI entwickelt wurde, ist der Rotor-Stator-Spinning-Disc-Reaktor (RSSDR). Obwohl zahlreiche Studien zur grundlegenden Charakterisierung dieses Reaktors bereits durchgeführt wurden, ist der RSSDR noch eine neue Technologie, deren Vermischungs-, Stoff- und Wärmetransporteigenschaften etc. nicht vollständig verstanden sind und die selten in Industrieanwendungen zu finden ist. Dies ist bedauerlich, da der RSSDR vermutlich großes Prozessintensivierungspotenzial für eine Vielzahl an Anwendungen aufweist, der RSSDR als neue Technologie jedoch Risiken birgt, die ihn unattraktiv für die Industrie machen. Deswegen ist eine weitere Charakterisierung der grundlegenden Eigenschaften sowie des Prozessintensivierungspotenzials essenziell.

In dieser Arbeit wurden die Hydrodynamik und Reaktionstechnik eines RSSDRs untersucht, indem die Wärmetransporteigenschaften experimentell und numerisch betrachtet wurden, wobei der numerische Ansatz die Simulation des Strömungsverhaltens im Rotor-Stator-Spalt beinhaltete, bevor die Simulation des gekoppelten Wärmetransports eines RSSDR Modells erfolgte. Zudem wurde das Potenzial des RSSDRs für die Prozessintensivierung einer stark exothermen Reaktion, welche die Vermischung zweier nicht mischbarer Fluide einschließt, analysiert. Als Beispielreaktion wurde die Epoxidierung von Methyloleat (MO) gewählt.

In der experimentellen Wärmetransportstudie wurde der Einfluss von der Rotations-Reynoldszahl, dem dimensionslosen Durchfluss, der Prandtlzahl und dem Spaltverhältnis auf den einphasigen, statorseitigen Wärmetransport betrachtet. Eine Erhöhung eines der untersuchten Parameter führt im ausgewählten Parameterbereich zu einer Erhöhung der statorseitigen Nusseltzahl. Ein laminares und ein turbulentes Strömungsregime wurde in Bezug auf die Rotations-Reynoldszahl beobachtet, welche mit einem durchfluss- und einem rotationsdominierten Wärmetransportregime korrelieren. Aus den experimentellen Ergebnissen wurde eine Nusseltzahl-Korrelation in Abhängigkeit aller untersuchten Parameter aufgestellt, welche die Experimente mit einer Genauigkeit von 20 % beschreibt. Eine deutliche Intensivierung des statorseitigen Wärmeübergangskoeffizienten und als Folge daraus des volumetrischen Wärmedurchgangskoeffizienten wurde durch eine Erhöhung der

Drehzahl des RSSDRs beobachtet. Die bestimmten volumetrischen Wärmedurchgangskoeffizienten sind doppelt so groß im Vergleich zu Wärmedurchgangskoeffizienten, die unter vergleichbaren Bedingungen an einem ähnlichen RSSDR Setup gemessen wurden, welche wiederum bereits fünfmal größer sind als jene in konventionellen Rohrreaktoren.

Da die experimentelle Untersuchung des Wärmetransports am RSSDR keine einfache Betrachtung lokaler Temperaturfelder und daraus die Ableitung radial aufgelöster Wärmeübergangskoeffizienten erlaubt und die Experimente aufwändig sind, wurde ein numerischer Ansatz verfolgt. Eine numerische Strömungsmechanikstudie der Strömungsverhältnisse im RSSDR wurde zunächst mit OpenFOAM® durchgeführt. Eine Turbulenzmodellstudie verschiedener Reynolds-averaged Navier−Stokes (RANS) Turbulenzmodelle zeigte, dass das *Lien-Leschziner*-Modell die turbulente Strömung im Reaktorspalt, welcher als zweidimensionale, achsensymmetrische (2.5D) Geometrie vereinfacht wurde, im untersuchten Parameterbereich gut beschreibt. Die Strömungssimulationen wurden für die Simulation des Wärmetransports am betrachteten RSSDR-Modell mit Hilfe eines modifizierten Wärmetransportlösers für gekoppelten Wärmetransport, der die Berücksichtigung der Dissipation ermöglicht, verwendet. Die aus den Simulationen gewonnenen radialen und axialen Temperaturverteilungen stimmen qualitativ mit Literaturergebnissen überein. Aus den Temperaturfeldern wurden lokale statorseitige Wärmeübergangskoeffizienten bestimmt, welche mit einer Erhöhung der Drehzahl und des Durchflusses ansteigen, wobei der Einfluss des Durchflusses zu höheren Radien hin verschwindet. Flächengemittelte Wärmeübergangskoeffizienten wurden ermittelt und zur Validierung mit den experimentellen Ergebnissen der ersten Studie dieser Arbeit verglichen, was eine gute Übereinstimmung ergab. Diese Studie zeigt die Möglichkeit Hydrodynamik und Wärmetransport eines RSSDRs anhand einer 2.5D-Modellgeometrie unter Verwendung eines RANS-Ansatzes für die Turbulenzmodellierung in OpenFOAM® zu charakterisieren.

Abschließend wurde die Intensivierung der Epoxidierung von MO mit Wasserstoffperoxid und Ameisensäure im RSSDR in Abhängigkeit von Drehzahl, Durchfluss und Temperatur mit und ohne katalysatorbeschichteter Rotorscheibe untersucht. Optimalwerte in Bezug auf die untersuchten Parameter wurden für die Reaktion, welche in halbkontinuierlicher Betriebsweise mit Recycle im RSSDR durchgeführt wurde, festgestellt. Obwohl der Einsatz eines heterogenen Katalysators keine vorteilhaften Ergebnisse unter den experimentellen Bedingungen zeigte, konnte im Vergleich mit Batchexperimenten, die als Benchmark durchgeführt wurden, eine deutliche Erhöhung der Epoxidausbeute und des Umsatzes an MO durch den Einsatz des RSSDRs festgestellt werden. Epoxidbildungsgeschwindigkeiten, die aus den Experimenten am RSSDR und Batchreaktor bestimmt wurden, zeigen auf, dass die Bildungsgeschwindigkeiten im RSSDR viermal so groß sind wie jene im Batchreaktor. In einem Vergleich der Epoxidbildungsgeschwindigkeiten des RSSDRs mit Literaturergebnissen zeigte sich, dass der RSSDR ähnliche Werte erzielt wie Mikroreaktorsysteme aus der Literatur und diese teilweise übertrifft. Folglich konnte mit dieser Studie demonstriert werden, dass der RSSDR eine signifikante Intensivierung

der Epoxidierung bedingt durch die exzellenten Stofftransport- und bis zu einer gewissen Drehzahl auch die hervorragenden Wärmetransporteigenschaften ermöglicht.

Contents

1 Introduction

In a world where natural catastrophes and famines are slowly reaching a state that could be perceived as normal, politics and industry are under pressure to establish a climate agreement without any compromises obstructing a serious effort to stop the world's climate change and to enforce it. Just recently the Intergovernmental Panel on Climate Change (IPCC) published a special report entitled "Global warming of 1.5 °C" [1]; in this report, the IPCC requests politics and industry to quickly introduce more measures for climate protection; higher energy efficiency and low-carbon energy sources are urgently necessary in order to limit global warming to 1.5 °C and stem negative consequences such as the occurrence of heat waves, a further rise in sea level and the dying of coral reefs [2].

Several research projects with many partners have been initiated in the last years focusing on feasible solutions for energy and carbon footprint reduction in industrial processes and the transition towards renewable energy sources: for example the "IC4" project on optimization of carbon dioxide conversion to natural gas [3], the !nnovA^2 project, in which the project partners examined innovative plant concepts to enhance the efficiency of production processes [4], or the Kopernikus project with its four subprojects ENSURE, P2X, SynErgie and ENavi, which were initiated for research on how the power grid can be adjusted to irregular power supply, how power from renewable resources can be stored, which technologies are necessary to adapt an industrial process to the power supply and what the best roadmap for the energy transformation is [5–8].

Against this background, the field of process intensification (PI) evolved and caught the interest of many researchers and institutions [9], such as the Process Intensification Network [10, 11], the European Federation of Chemical Engineering [12] or the DECHEMA [13]. The term PI was first used in a Polish journal in 1973 [14] according to Keil [10]. Many definitions of PI were given over the years; Cross and Ramshaw [15], one of the pioneers in PI, e.g., defined PI as the "strategy of reducing the size of a chemical plant needed to achieve a given production objective" [16]. This was extended by Stankiewicz and Moulijn [17] to PI being the "development of innovative apparatuses and techniques that offer drastic improvements in chemical manufacturing and processing, substantially decreasing equipment volume, energy consumption, or waste formation, and ultimately leading to cheaper, safer, sustainable technologies" [16], as the former definition merely included one aspect of the desired effects of PI [17]. A newer definition by the European Roadmap of Process Intensification states, PI "provides radically innovative principles

("paradigm shift") in process and equipment design which can benefit (often with more than a factor two) process and chain efficiency, capital and operating expenses, quality, wastes, process safety and more" [16, 18]. The assumption by van Gerven et al. [16] and Keil [10] that there will never be a "single, commonly accepted definition" [16] of PI is probably right. It is "rather the societal relevance of the issues it addresses" [16], making PI an important tool in todays society.

The field of PI can be divided into two subcategories: process-intensifying equipment and process-intensifying methods [17]. The first category includes novel reactor types and devices for intensive mixing, mass and heat transfer, and the latter techniques for, e.g., phase transition and heat exchange or hybrid separations and the integration of separation and reaction, by means of applying inventive methods for process control and renewable energy sources [17]. One novel reactor technology classified under process-intensifying equipment is the rotor-stator spinning disc reactor (RSSDR). This reactor type was further developed from the simple spinning disc reactor (SDR) [9] as one of many rotating reactors dating back to 77 A.D. when the first stirred tank reactors were used [19, 20]. The RSSDR consists of a stator housing enclosing a concentrically aligned rotor; it is characterized by the small distance between the rotating and static parts and the high energy input induced in the fluid in the reactor gap by the rotor. Thus, this reactor type provides excellent mass and heat transfer properties [21, 22]. Several studies on the mixing properties as well as mass and heat transport characteristics in RSSDRs [21–30], which will be more thoroughly presented in Section 2.1.1, have already been performed. The aim of this work is to further characterize the RSSDR in terms of reaction engineering and hydrodynamics.

In Chapter 3 of this thesis, an experimental study on the single-phase stator-side heat transfer of two different RSSDR setups will be presented. Therefore, first a stator housing made of an aluminum alloy and integrated coolant channels was designed in two sizes for the already existing rotor-stator setup to allow good temperature control of the reactor gap. For evaluation of the experiments, the prevailing reactor model introduced by de Beer et al. [31] is used as the base for a simple reactor modeling making the experiments evaluable. One challenge in this study is the correct consideration of the dissipative power input due to rotation, which becomes relevant at disc speeds above $1000\,\mathrm{min}^{-1}$. Overall heat transfer coefficients are determined from which stator-side heat transfer coefficients and Nusselt numbers are derived. The results are summarized in form of a Nusselt number correlation in dependence of dimensionless flow parameters, material properties and geometric design parameters.

As the experimental investigation of heat transfer in RSSDRs, especially with small dimensions, is complex and it is difficult to consider local and not only overall quantities, Chapter 4 of this thesis deals with a computational fluid dynamics simulation of flow and heat transfer in an RSSDR. For a selection of rotational disc speeds and throughputs,

the RSSDR of the study presented in Chapter 3 is simulated as an axisymmetric two-dimensional setup using a Reynolds-averaged Navier−Stokes approach for turbulence modeling. First, an appropriate turbulence model is chosen by means of simulating model geometries of rotor-stator cavities found in literature for which experimental data on pressure and velocity exists and comparing the simulations of this work with the experiments to identify the turbulence model representing the experimental data best. This model is then used for flow simulations of the studied RSSDR, which are subsequently used for simulations of the heat transfer. Therefore, an existing solver for conjugate heat transfer of several regions is modified by a source term accounting for dissipative power inputs. Local temperature profiles and heat transfer coefficients are determined and based on the latter average heat transfer coefficients are derived and compared to the experiments presented in Chapter 3.

In Chapter 5, the excellent heat transfer properties studied in Chapters 3 and 4 as well as the eminent mixing and mass transfer properties [22, 23] are applied to intensify the epoxidation of the fatty acid methyl ester (FAME): methyl oleate. This reaction was chosen, since epoxidized FAMEs are important starting materials for a variety of industrial applications (lubricants, bio-fuel additives, stabilizers for polyvinyl chloride resins, plasticizers, cosmetics and pharmaceuticals [32–37]) and the epoxidation carried out with hydrogen peroxide and formic acid needs excellent mixing properties because two immiscible fluids need to be brought into contact. Furthermore, the reaction is very exothermic (reaction enthalpy of $\Delta H_\mathrm{R} = -230.2\,\mathrm{kJ\,mol^{-1}}$ per double bond [33]), which is why excellent temperature control must be provided. Moreover, due to the usage of hydrogen peroxide, the reaction holds a safety risk, which should be easily controllable with the small reactor volume V of a typical RSSDR (in this study $V \approx 32\,\mathrm{mL}$). A stator housing of robust stainless steel with integrated coolant channels is designed and the sealing of the reactor gap against the drive shaft improved in order to make it insensitive to the aggressive media used in this study. The epoxidation reaction is carried out in a semi-batch operational mode with recycle through the RSSDR for various operating conditions. The results are compared to two sets of batch experiments performed as benchmark in this study.

2 Theoretical background and literature review

In this work, the innovative reactor technology rotor-stator spinning disc reactor (RSSDR) is characterized in terms of reaction engineering and hydrodynamics. Heat transfer properties are examined experimentally and numerically, which also requires investigation of the flow profiles and regimes of said reactor type. Therefore, the first section (Section 2.1) of this chapter deals with the general principle of the RSSDR, the hydrodynamics and heat transfer properties of rotor-stator cavities. In a further part of this work, the beneficial heat and mass transfer properties of the RSSDR are applied to intensify a test reaction system, which needs good temperature control and very good mixing properties, i.e., Prilezhaev epoxidation of a fatty acid methyl ester (FAME) such as methyl oleate (MO) [32]. In Section 2.2 of this chapter, the Prilezhaev epoxidation reaction, the reaction mechanism and possible side and consecutive reactions are presented.

2.1 Rotor-stator spinning disc reactor

2.1.1 The rotor-stator spinning disc reactor

The studied RSSDR of this work is depicted schematically in Figure 2.1. It consists of a stator housing, enclosing a concentrically aligned rotor disc, with integrated coolant channels for temperature control. The distance between static and rotating parts is 1 mm each in the upper and lower reactor gap, which is typical for this reactor type, as it generally ranges between 1 mm and 5 mm [9]. Two setups with different rotor radii, but apart from that the same geometric configuration, are examined, with one being 65 mm and the larger one having a value of 135 mm. As indicated in Figure 2.1, the reactor gap medium enters the studied RSSDR at the top near the center, flows through the upper gap towards the outer rim of the gap, where it flows down to the lower gap, from where it is further led to the bottom center of the RSSDR, where it leaves the reactor. Due to the rotation of the rotor, which can reach rotational disc speeds of 4000 min^{-1} for the setup with a radius of 65 mm and 2000 min^{-1} for the other setup, and the small gap height, large shear forces are induced into the fluid in the reactor gap. In dependence of the

operating conditions, volumetric throughput and rotational disc speed, turbulences and the formation of different flow regimes are caused in the reactor gap [23, 27], which will be discussed in more detail in Section 2.1.2.

In case of a two-phase, more specific a liquid-liquid, flow in the reactor gap, it is reported that, assuming sufficient mixing due to high disc speeds is provided, a well dispersed mixture is present on upper and lower side of the rotor [38]. This is different from gas-liquid flow behavior, in which two-film flow is observed in the reactor gap, where the two phases are introduced, and gas bubbles dispersed in the liquid on the respective other rotor side [22, 39]. As gas-liquid flow does not play an important role in this work, the focus of multi-phase flow in Section 2.1.2 is laid on liquid-liquid flow.

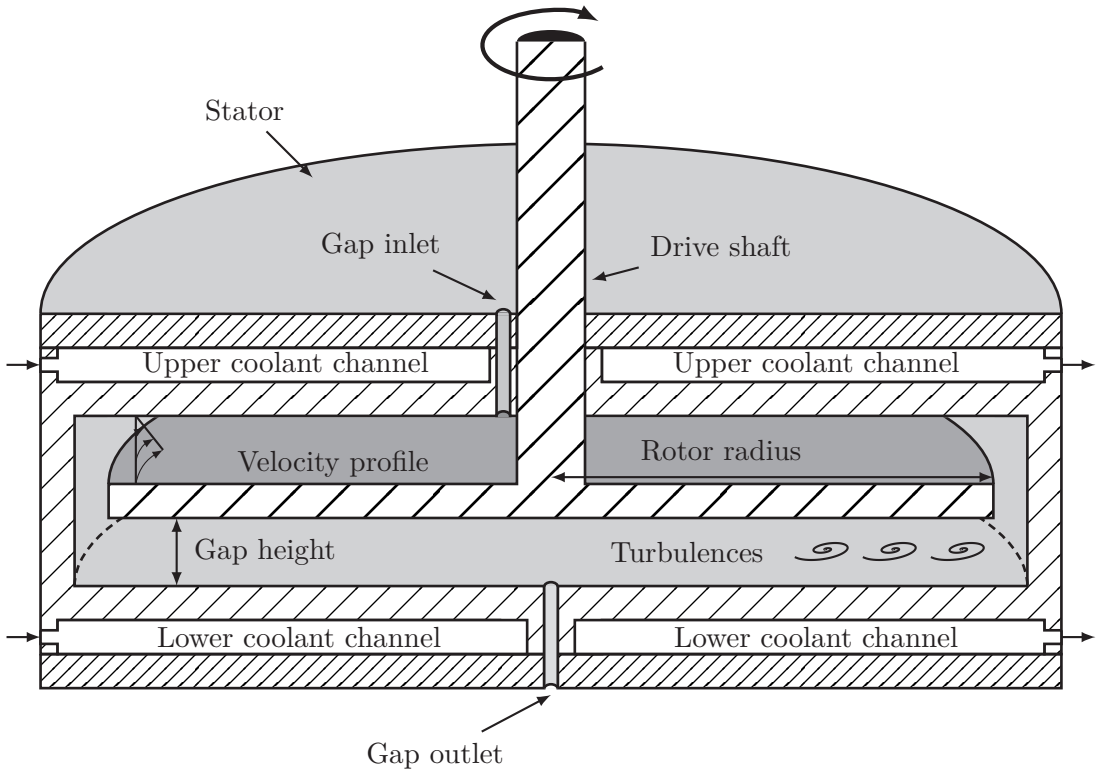

Figure 2.1: Schematic of a rotor-stator spinning disc reactor with integrated coolant channels in the stator as used in this thesis.

In the past decade, the RSSDR has been the interest of many studies. Visscher et al. [40] were the first to examine residence time behavior of a single-phase RSSDR and proposed a reactor model based on their experiments building on a plug flow reactor (PFR) and two to three ideally stirred tanks in series. This model was further developed by de Beer et al. [21, 41], who suggested a reactor model consisting of a PFR and one continuous stirred tank reactor (CSTR). This model was confirmed and the parameter range of its applicability extended by Haseidl et al. [42]. The latter model forms the base for evaluation of the heat transfer experiments in Chapter 3, in which it will be explained in more detail.

Haseidl et al. [9, 23] further examined the micromixing properties by means of the Villermaux-Dushman reaction and found a strong influence of the local energy input on the segregation index and mixing time. A similar study was performed by Martinez et al. [24], who observed fast mixing times in the range of $1.13 \cdot 10^{-4}$ s to $8.76 \cdot 10^{-3}$ s.

Plenty of studies on mass transfer properties of RSSDRs were performed. Meeuwse et al. [22, 26, 27, 39] focused on gas-liquid substance systems and investigated the gas-liquid mass transfer coefficient of single- and multi-stage RSSDRs in dependence of different operating parameters, reactor gap distances and the influence of co-feeding gas and liquid systems at one reactor inlet. They found volumetric mass transfer coefficients in the desorption process of oxygen from water being 40 times larger compared to conventional bubble columns, which is attributed to smaller gas bubbles with increasing disc speeds [19, 26]. Similar gas-liquid mass transfer studies were performed by Haseidl et al. [28]; they used a new reactor setup with a perforated rotor disc containing 119 channels in order to disperse the gas phase directly via the rotor disc. High volumetric mass transfer coefficients were achieved due to large energy inputs at high disc speeds; a correlation for a power law model describing the impact of the main operating parameters on the volumetric mass transfer coefficients was established [28]. The multi-stage RSSDR study on gas-liquid mass transfer by Meeuwse et al. [39] further revealed that each stage of the multi-stage RSSDR behaves as a single RSSDR. Thus, easy scale-up is possible, as several stages could be simply stacked above one another on the drive shaft, and the behavior of each one can be easily extrapolated.

A numerical approach on gas-liquid mass transfer in an RSSDR was pursued by van Eeten et al. [43]. They used direct numerical simulation in order to describe the flow field around a single bubble in the RSSDR and showed that the presence of turbulence inside the thin liquid film, which surrounds the bubble, is due to vortex stretching [43]; they also derived an expression from their simulations representing experimental data in literature. The flow of co-fed gas-liquid flow in RSSDRs was also studied by de Beer et al. [44], who examined pressure drop signals with high speed imaging and spectral analysis; they observed two bubble formation mechanisms, of which one is caused by gas overpressure and the other one due to turbulent vortices.

Liquid-solid mass transfer experiments investigating the heterogeneously catalyzed oxidation of glucose in an RSSDR were performed by Meeuwse et al. [25] and Haseidl et al. [23]; Meeuwse et al. [25] reported a liquid-solid mass transfer limited regime at lower angular velocities such as $26\,\mathrm{rad\,s^{-1}}$, whereas at higher velocities ($157\,\mathrm{rad\,s^{-1}}$), the reaction is limited by the intrinsic kinetic; a strong increase in volumetric mass transfer coefficient with increasing angular velocity was observed with the coefficient at the highest observed velocity being eleven times higher in contrast to the lowest one [25].

As mentioned before, Visscher et al. [45, 46] studied liquid-liquid systems; liquid-liquid mass transfer rates of the extraction of benzoic acid from *n*-heptane to water were

examined for a similar RSSDR as studied in this work for rotational disc speeds between $100\,\mathrm{min}^{-1}$ and $1600\,\mathrm{min}^{-1}$. Mass transfer rates were determined, which are at least 25 times larger in comparison to packed bed columns and 15 times higher than mass transfer rates in microchannels [19, 45]. An impeller reactor was developed from the RSSDR, which should intensify liquid-liquid contacting equipment by exploiting the high liquid-liquid mass transfer rates [19, 47, 48]. Liquid-liquid extraction in an RSSDR was also examined by Wang et al. [49]; they used a rotor-stator spinning disc extractor to extract phosphoric acid from an aqueous to an organic phase and investigated parameters such as disc speed, volumetric throughput and rotor-stator distance. They observed increased volumetric mass transfer coefficients with increasing disc speed and throughput and decreasing gap distance [49].

Single- and multi-phase heat transfer studies on RSSDRs or stator-rotor-stator spinning disc reactors (SRSSDR) were performed by de Beer et al. [21, 29, 30, 41, 50]. In their study on single-phase stator-side heat transfer of an RSSDR setup very similar to the one used in this work, they studied the parameters rotational disc speed and volumetric throughput for two different aspect ratios; they observed a throughput-governed heat transfer regime for low rotational Reynolds numbers (Equation (2.1)), in which Nusselt numbers (Equation (2.9)) increase with increasing dimensionless throughput (Equation (2.3)) and decreasing aspect ratio (Equation (2.2)), whereas they observed a rotation-governed heat transfer regime at higher rotational Reynolds numbers, where aspect ratio and throughput play no important role anymore [21]. By means of further developing the RSSDR to an SRSSDR, heat transfer in the RSSDR can be further enhanced, as rotation is used on reactor and coolant medium side to intensify the heat transfer coefficients; with this setup, de Beer et al. [29] investigated the rotor-side heat transfer coefficient and observed a similar trend for the rotor-side heat transfer coefficient as for the stator-side one with respect towards rotational disc speed, and no influence of throughput on the rotor-side heat transfer coefficient. Generally, high heat transfer coefficients are achieved with the described setups, which reach values up to $10^4\ \mathrm{W\,m^{-2}\,K^{-1}}$ at angular velocities of $120\,\mathrm{rad\,s^{-1}}$ [41]. Similar values were observed for forced convective condensation or boiling heat transfer in SRSSDRs; the heat transfer coefficients for boiling are slightly lower than the ones for turbulent single-phase flow and the ones for condensation are a bit higher [41].

In recent years, the basic RSSDR has also been applied as a rotor-stator spinning disc heat exchanger for drying liquids, providing an “elegant, energy-efficient water removal process” for the “removal of trace amounts of water from hydrate forming liquids” [51, 52]. Granados Mendoza et al. [53, 54] and Moshtarikhah [55] used the RSSDR as a spinning disc membrane electrolyzer for intensification of the chlor-alkali process; they showed that the alkali process at high current densities is possible and that the spinning disc membrane electrolyzer yields production rates being three times as large as the ones achieved in conventional parallel plate cells [54].

2.1.2 Hydrodynamics of single- and multi-phase flow in rotor-stator cavities

Many studies on hydrodynamics of single-phase flow in rotor-stator cavities were performed in the past decades originating from research on turbomachinery [9, 21, 56–60]. The characteristic dimensionless numbers determining the flow in between a rotor and a stator are the rotational Reynolds number Re_Ω (Equation (2.1)), the aspect or gap ratio G (Equation (2.2)) and the dimensionless throughput C_W (Equation (2.3)).

$$Re_\Omega = \frac{\Omega\, r_{\mathrm{r,o}}^2}{\nu} \tag{2.1}$$

$$G = \frac{s}{r_{\mathrm{r,o}}} \tag{2.2}$$

$$C_W = \frac{\dot{V}_{\mathrm{R}}}{r_{\mathrm{r,o}}\, \nu} \tag{2.3}$$

The parameters in Equations (2.1) to (2.3) are angular velocity Ω, the outer radius of the rotor $r_{\mathrm{r,o}}$, kinematic viscosity ν, gap height s and volumetric throughput through the gap $\dot{V}_{\mathrm{R}}$.

In the following, the basic flow profiles of single-phase flow in between a rotor and a stator will be discussed as well as the boundary layers, which are formed at the stator and rotor side of the cavity, first for closed cavities and second for cavities with superimposed throughputs in dependence of the introduced dimensionless numbers.

Flow profiles in rotor-stator cavities without superimposed throughput

Figure 2.2 shows radial (top row) and tangential (bottom row) velocity profiles of Stewartson (Figure 2.2a), Batchelor (Figure 2.2b) and torsional-Couette flow (Figure 2.2c) in a rotor-stator cavity, with the stator being the upper geometric restriction to the cavity and the rotor being the lower one. For Stewartson flow, the formation of a boundary layer exclusively at the rotor side with velocity components in radial and tangential direction is characteristic, as can be seen in Figure 2.2a. This boundary layer is called von Kármán layer [61]. Outside the rotor-side boundary layer, the core of the liquid is at rest in radial and tangential direction [62]. Stewartson type flow occurs when the fluid in the cavity does not encounter a geometric restriction in radial direction, but only in axial direction at the stator and rotor side [9, 62]. The flow in the rotor-stator cavity in this case is caused by the radial acceleration of the fluid due to centrifugal force [9, 62].

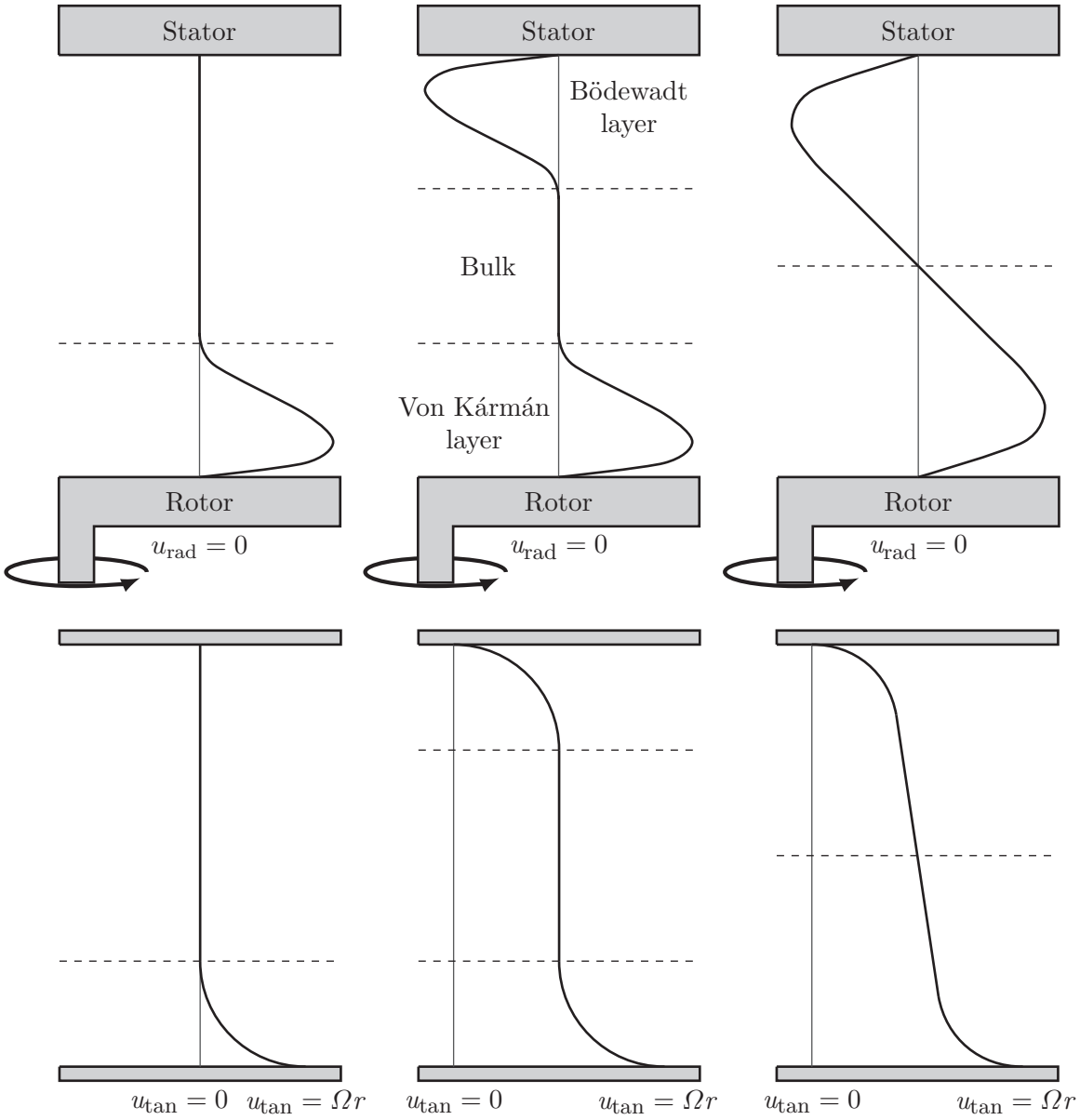

(a) Stewartson flow. **(b)** Batchelor flow. **(c)** Torsional-Couette flow.

Figure 2.2: Schematic of the radial (top row) and tangential (bottom row) flow profiles in rotor-stator cavities based on [9]: (a) Stewartson flow with velocity components exclusively in the von Kármán boundary layer at the rotor [62], (b) Batchelor flow with velocity components in both boundary layers and a rotating fluid core [63] and (c) torsional-Couette flow with merged von Kármán and Bödewadt layer [64, 65].

In case a closed rotor-stator cavity is regarded, the flow is redirected at the outer cylinder of the stator housing and circulates back, in the boundary layer at the stator side, towards the center of the cavity due to mass conservation [64]. The stator-side boundary layer is named after Bödewadt, who studied a turning fluid over a solid plate [66], on the contrary to von Kármán, who studied a rotating plate in a liquid [61]. The formation of the boundary layers depends on the geometric and operational parameters of a regarded rotor-stator cavity [9, 64, 67–69]. Two different flow types with boundary layers present

at rotor and stator side can occur: Batchelor flow (Figure 2.2b) and torsional-Couette flow (Figure 2.2c).

The flow is characterized as Batchelor flow, if the two boundary layers are separated by a rotating core, which has no velocity in radial direction, but a constant tangential velocity for the main body (cf. Figure 2.2b). In case the two boundary layers are merged, the flow is classified as torsional-Couette flow (cf. Figure 2.2c). The occurrence of Batchelor or torsional-Couette flow is dependent on aspect ratio and rotational Reynolds number, which can be seen in the flow map in Figure 2.3 introduced by Daily and Nece [65] based on their study on enclosed rotating discs.

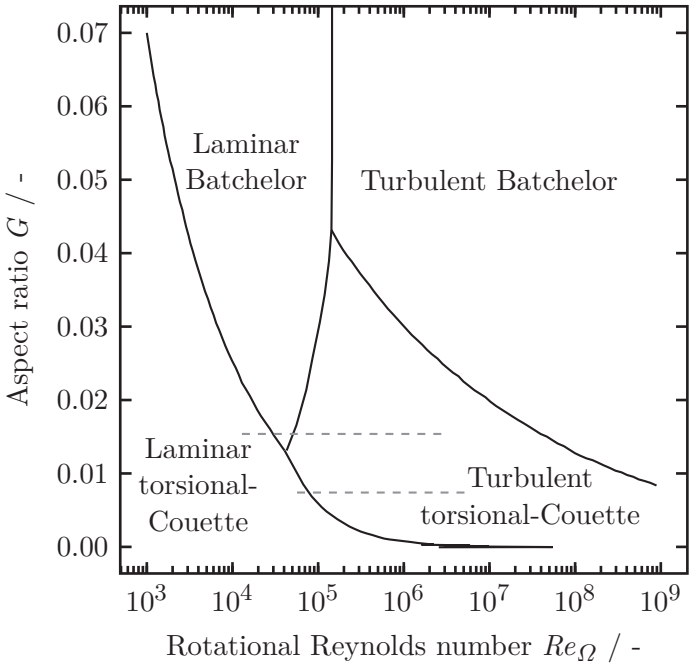

Figure 2.3: Flow map for rotor-stator cavities without superimposed throughput [65, 67]. The dashed lines indicate the regarded parameter range of this study.

In general, for large aspect ratios, Batchelor flow is found in closed rotor-stator cavities and torsional-Couette flow for small aspect ratios (cf. Figure 2.3). Each of the just described flow types occurs in laminar and turbulent form in dependence of the rotational Reynolds number. The transition from laminar to turbulent and Batchelor to torsional-Couette flow is not indicated by either a vertical or horizontal line in Figure 2.3, respectively, but the transition is an interplay of aspect ratio and rotational Reynolds number resulting in transition curves.

The flow map shown in Figure 2.3 is technically only for enclosed rotor-stator cavities without superimposed throughput. It will, however, be used for a general classification of the flow conditions of the studied parameter range in this work. How the just described flow profiles in cavities without an external flow change when an outer flow is superimposed, will be discussed in the next section.

Flow profiles in rotor-stator cavities with superimposed throughput

If an external flow is superimposed on a flow in a rotor-stator cavity (a centrifugal flow is assumed for the following remarks, i.e., $C_W > 0$), the tangential velocity profile resembles a Stewartson type flow at radial positions near the rotation axis (cf. Figure 2.4, bottom left corner) [9, 31, 58, 59]. As the shear forces acting on the fluid in the gap are low at radial positions close to the rotation axis, tangential velocity components are only present in the von Kármán layer [9]. Due to the centrifugally superimposed flow, the velocity component in radial direction is positive across the entire gap height at low radial positions (cf. Figure 2.4, top left corner). In this region of the gap, rotation plays a minor role, which is why the radial velocity profile resembles the axial velocity profile of a conventional pipe flow; this flow is throughput governed [9, 64]. With increasing radial position, the flow profiles change to torsional-Couette behavior, which can be seen in Figure 2.4 on the right side. Despite the superimposed centrifugal flow, the flow in the Bödewadt layer changes to a centripetal one due to the strong centrifugal acceleration in the von Kármán layer [9, 64, 70] and the radial velocity profile in the middle of the cavity becomes linear, which results from strong shear forces [64]. The absolute value of the radial velocity in the rotor-side boundary layer at intermediate radial positions is higher compared to the velocity in the stator-side layer due the combination of the superimposed centrifugal flow and the centrifugal force, which is caused by the rotation of the disc; in the torsional-Couette regime, rotation plays the predominant role determining the flow behavior [64].

A correlation describing the transition radius r_{trans} from Stewartson to torsional-Couette flow in dependence of rotational Reynolds number and dimensionless throughput is given in Equation (2.4) [58, 60].

$$r_{\mathrm{trans}} = r_{\mathrm{r,o}} \left(\frac{1}{c_{\mathrm{trans}}} \frac{|C_W|}{Re_\Omega^{4/5}} \right)^{5/13} \tag{2.4}$$

The theoretical value of the parameter c_{trans} is $c_{\mathrm{trans}} = 0.219$ [60], which was validated numerically by Haddadi et al. [64] and Poncet et al. [58]. This value is valid for large aspect ratios, i.e., Batchelor flow, where the parameter c_{trans} is independent from the aspect ratio; with decreasing aspect ratio a decrease in c_{trans} is visible [9, 31, 42]. De Beer et al. [21] established a correlation for the parameter in dependence of the aspect ratio for aspect ratios $G < 0.038$ (Equation (2.5)).

$$c_{\mathrm{trans}} = 8.4 \cdot 10^{-4} \exp(146.6\, G) \tag{2.5}$$

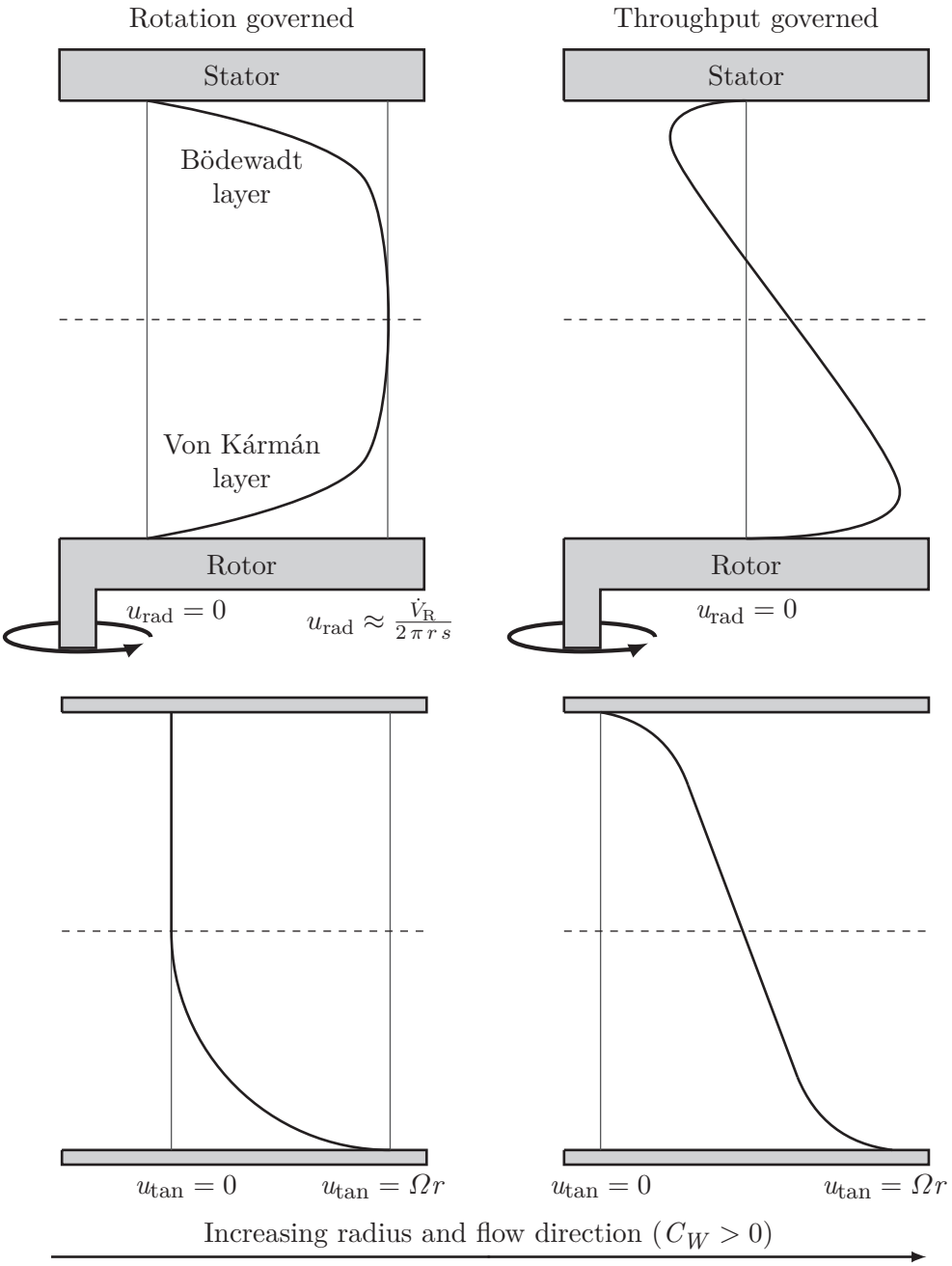

Figure 2.4: Schematic of radial (top row) and tangential (bottom row) velocity profiles of a centrifugally superimposed throughput in a rotor-stator cavity in dependence of radial position [31].

Interpreting Equation (2.4), it becomes clear that the transition radius between throughput- and rotation-governed regions in the reactor gap depends on the relation between the superimposed throughput and the radial velocities induced by the rotation of the rotor [9]. If $r < r_{\mathrm{trans}}$, the radial velocity across the entire gap height is unidirectional and the flow is throughput governed, since the radial velocity component is larger than the radial velocity of the recirculating flow in the Bödewadt layer [9]. If $r \geq r_{\mathrm{trans}}$, the radial velocity features centripetal (Bödewadt layer) and centrifugal (von Kármán layer)

velocity components across the gap height and a recirculating flow is present, which is governed by rotation [9, 60, 64].

In an RSSDR, two gaps are considered, one above and one below the rotor disc. For the studied setup of this work, with the reactant inlet at the top near the center and the outlet at the bottom center (cf. Figure 2.1), a centrifugal superimposed flow is present in the upper reactor gap and a centripetal flow in the lower gap, respectively. In case of a centripetal superimposed flow, the tangential velocity of the fluid in the gap increases towards lower radial positions at radial positions close to the center of rotation; this is due to conservation of angular momentum of the fluid [9, 64]. At these radial positions close to the center of rotation, a negative radial velocity is present across the entire gap height [9, 58, 64, 67, 70, 71]. At higher radial positions, the flow in the reactor gap is similar to flow conditions occurring in a gap with centrifugal superimposed flow: a Batchelor or torsional-Couette flow is present depending on the external parameters; however, the Bödewadt boundary layer is more distinctly present and features higher radial velocities towards the center due to the superimposed centripetal flow [9, 57, 64].

According to Haddadi et al. [64], the radial velocity profiles in the reactor gaps for centripetal and centrifugal flow show similar profiles, which is why symmetric flow behavior can be assumed for the reactor gap above and below the rotor disc of the RSSDR [9, 31]. The parameter range studied in this work is indicated by the gray lines in Figure 2.3, one for the large setup with an aspect ratio of $G = 1\,\mathrm{mm}/135\,\mathrm{mm} = 0.0074$, with the denotation large referring to the radius, and one for the small setup with the smaller radius, i.e., the larger aspect ratio of $G = 1\,\mathrm{mm}/65\,\mathrm{mm} = 0.0154$. Figure 2.3 indicates that the majority of the studied parameter range of this work lies in the turbulent torsional-Couette regime. Thus, centrifugal fluid flow occurs in the von Kármán layer and centripetal flow in the Bödewadt layer, as the radial velocity components are higher compared to the superimposed throughputs creating recirculation in large parts of the rotor-stator cavities [9].

Multi-phase flow in rotor-stator cavities

As described in Section 2.1.1, the focus of multi-phase flow in RSSDRs is laid on liquid-liquid flow behavior in RSSDRs, even though more research is available on gas-liquid flow and mass transfer properties. Figure 2.5 shows the two-phase flow and volume fractions of water and n-heptane in dependence of rotational disc speed from experiments performed by Visscher et al. [45] on liquid-liquid mass transfer in an RSSDR similar to the reactor setup studied in this work; the water phase is shown blue and n-heptane is transparent.

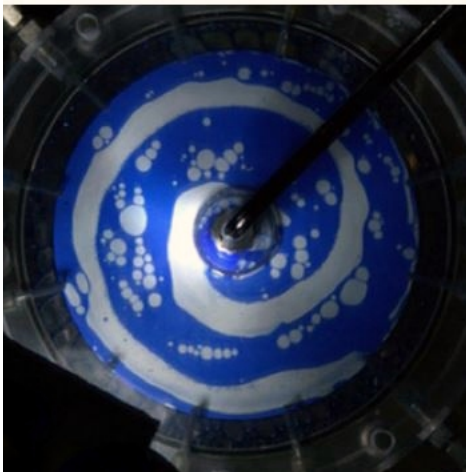

(a) $n = 50\,\mathrm{min}^{-1}$.

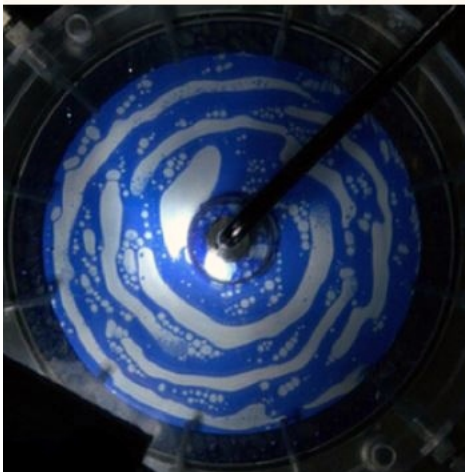

(b) $n = 100\,\mathrm{min}^{-1}$.

(c) $n = 200\,\mathrm{min}^{-1}$.

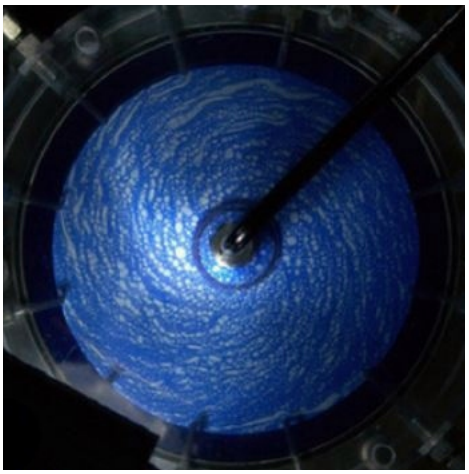

(d) $n = 300\,\mathrm{min}^{-1}$.

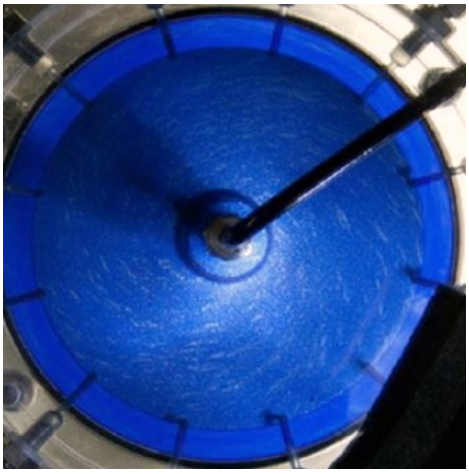

(e) $n = 500\,\mathrm{min}^{-1}$.

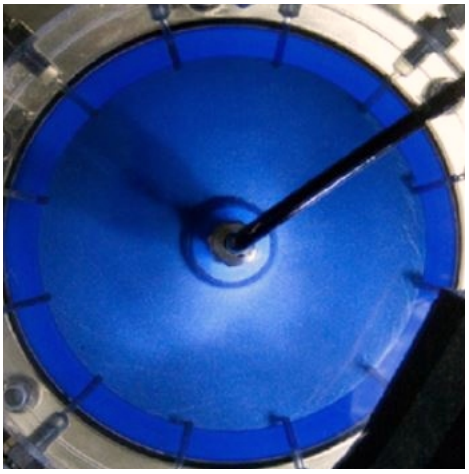

(f) $n = 700\,\mathrm{min}^{-1}$.

Figure 2.5: Two-phase flow and volume fractions in dependence of rotational disc speed from experiments by Visscher et al. [45]. Photographs are taken of the bottom stator of an RSSDR with a total flow rate of $4.7 \cdot 10^{-6}$ $\mathrm{m}^3\,\mathrm{s}^{-1}$. The water phase appears in blue, colored by an ink, and *n*-heptane appears transparent.

The results are from experiments, in which water is introduced to the upper gap of the reactor near the center of rotation; *n*-heptane with benzoic acid is introduced at the outer rim of the lower gap and the two media leave the reactor at the outlet at the bottom center of the lower gap [45]. Consequently, the pictures in Figure 2.5 are showing the lower gap of the RSSDR.

Visscher et al. [45] observed three different flow patterns in dependence of rotational disc speed for the studied system. For rotational disc speeds up to $100\,\mathrm{min}^{-1}$ (cf. Figures 2.5a and 2.5b) the radial flow of *n*-heptane towards the center behaves as a continuous spiral, which does not feature any backmixing [45]. With increasing rotational disc speed up to $300\,\mathrm{min}^{-1}$, the continuous *n*-heptane spiral breaks open and droplets are formed, moving in a spiral towards the outlet in the center; this is caused by the stronger shear forces induced in the lower reactor gap with increasing disc speed [45] (cf. Figures 2.5c and 2.5d). A further increase in rotational disc speed results in very small *n*-heptane droplets with diameters smaller than the gap height of 1 mm being dispersed in the water [45] (cf. Figures 2.5e and 2.5f). The rotational disc speeds in Figure 2.5 are only shown up to $700\,\mathrm{min}^{-1}$, since a further increase up to $1600\,\mathrm{min}^{-1}$ does not change the resulting flow behavior [45]. As at these rotational disc speeds boundary layers are formed on rotor and stator side, both phases are backmixed and ideally mixed flow behavior is assumed [45, 58, 72]. The latter was verified by Visscher et al. [45], as they observed *n*-heptane in the upper reactor gap during the experiments at higher disc speeds, which could only happen, if the flow was ideally mixed.

As stated before, the flow behavior of liquid-liquid flow in an RSSDR is the same for the upper and lower reactor gap in contrast to gas-liquid systems [38, 46]. Also, the flow types discussed for single-phase flow (cf. Section 2.1.2) are generally applicable to multi-phase flow [9].

2.1.3 Heat transfer in rotor-stator cavities

The interest in heat transfer properties of rotor-stator systems also arises from the research on turbomachinery [67]. A brief description of exemplary temperature profiles and Nusselt number behavior in rotor-stator cavities of model geometries found in literature will be presented in the following sections.

Axial temperature profiles across the reactor gap

Figure 2.6 shows the dimensionless temperature profile across the dimensionless gap height z/s, with the axial position z, for three dimensionless radii $r/r_{\mathrm{r,o}}$ from simulations performed by Poncet et al. [73] on the experimental setup examined by Djaoui et al. [67]. The regarded rotor-stator cavity consists of a rotating disc at the bottom ($z/s = 0$) and

a heated stationary disc as upper geometric restriction ($z/s = 1$); the superimposed flow is centripetal [73]. The dimensionless temperature T^* in Figure 2.6 is calculated from the local temperature T, the wall temperature of the heated stator T_s and the temperature at the boundaries rotor and inlet T_bc [73].

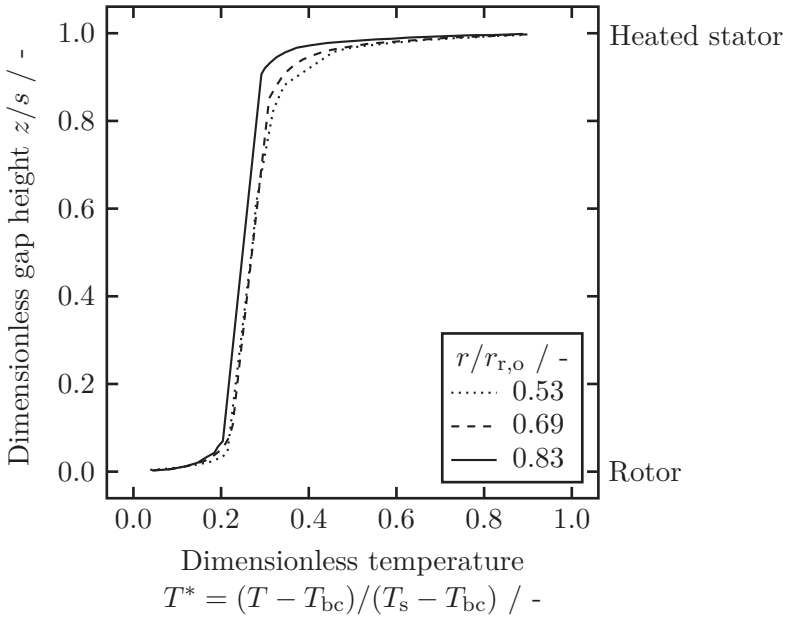

Figure 2.6: Axial temperature profiles at three radial locations for $C_W = -12082$, $Re_\Omega = 1.44 \cdot 10^6$, $G = 0.08$ and $Pr = 0.7$ (Equation (2.6)). Simulations were performed by Poncet et al. [73] with a Reynolds stress model (RSM) to predict the experiments of Djaoui et al. [67].

Steep temperature profiles with boundary layers present at the rotor and stator side can be seen in Figure 2.6, with a large change in temperature in the stator-side boundary layer. The temperature profiles resemble the tangential velocity profiles in the torsional-Couette regime and the boundary layers at the stator side thicken with decreasing radial position [73].

Local Nusselt numbers in dependence of radial position

Poncet et al. [73] also extended the results of the temperature profiles of Djaoui et al. [67], in order to investigate the effect of the Prandtl number (Equation (2.6)) on the local Nusselt number, which they defined in dependence of the local radius and wall heat flux.

$$Pr = \frac{\nu}{a} = \frac{\mu\, c_p}{\lambda} \tag{2.6}$$

The parameters in Equation (2.6) are thermal diffusivity a given in Equation (2.7), specific heat at constant pressure c_p, dynamic viscosity μ and thermal conductivity λ.

$$a = \frac{\lambda}{\varrho\, c_p}, \tag{2.7}$$

with density ϱ. The local and average Nusselt numbers as used in this work are defined in Equations (2.8) and (2.9), respectively:

$$Nu_{\mathrm{loc}} = \frac{\alpha_{\mathrm{loc}}\, r}{\lambda}, \tag{2.8}$$

$$Nu = \frac{\alpha\, r_{\mathrm{r,o}}}{\lambda}, \tag{2.9}$$

with the local and integral heat transfer coefficients α_{loc} and α, respectively, and the local radius r. Technically, thermal conductivity should also be a local quantity in the definition of the local Nusselt number. However, as the studied temperature differences of the media in the reactor gap are small to moderate, and no strong changes in material properties are expected, isothermal conditions are assumed for the regarded media.

The dependence of the local stator-side Nusselt number $Nu_{\mathrm{s,loc}}$ from the numerical study by Poncet et al. [73] on radial position and Prandtl number is shown in Figure 2.7.

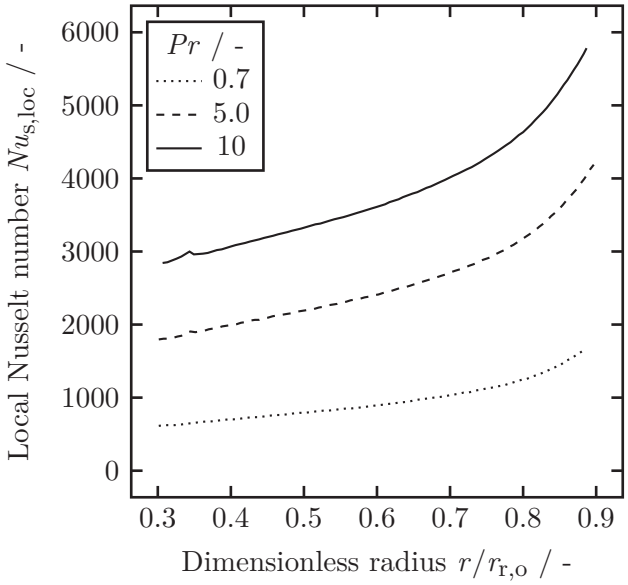

Figure 2.7: Local Nusselt number in dependence of radial position for $C_W = -12082$, $Re_\Omega = 1.44 \cdot 10^6$ and $G = 0.08$. Simulations were performed by Poncet et al. [73] with a Reynolds stress model (RSM).

An increase in local Nusselt number with a rise in radial position and Prandtl number is observed in Figure 2.7. The rise in Nusselt number with increasing radial position is

attributed to higher local velocities at higher radii caused by the rotation of the rotor; Djaoui et al. [67], however, reported that at small radial positions, first a small decrease of the local Nusselt number is observable due to the decrease in radial velocity, as radius increases for a constant superimposed throughput, which is presumably not the case in Figure 2.7, since the dimensionless throughput is very high.

Average Nusselt numbers in dependence of rotational Reynolds number, Prandtl number and dimensionless throughput

Based on the local Nusselt number, the integral Nusselt number of the stator or rotor side can be determined. Figure 2.8 displays the average stator-side Nusselt numbers from the results of Poncet et al. [73] of the single rotor-stator cavity described above, in dependence of Prandtl number, rotational Reynolds number and dimensionless throughput.

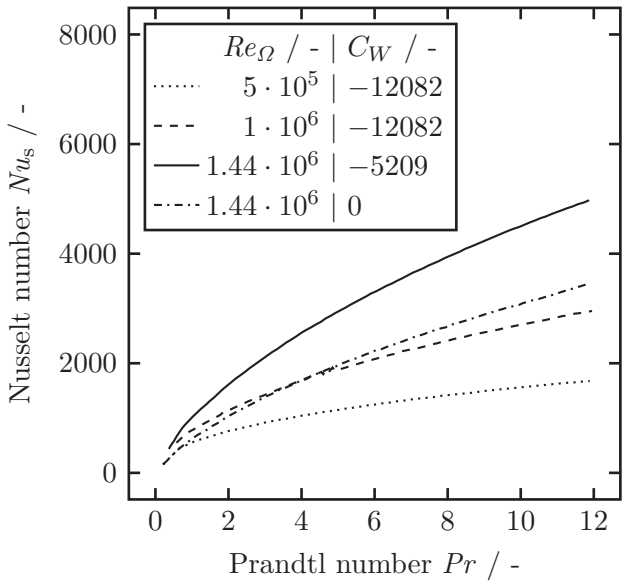

Figure 2.8: Average Nusselt number in dependence of Prandtl number for different rotational Reynolds numbers and dimensionless throughputs from simulations performed with a Reynolds stress model (RSM) by Poncet et al. [73].

The average stator-side Nusselt number increases with a rise in Prandtl number, rotational Reynolds number and dimensionless throughput. The dependence of the Nusselt number on Prandtl number is high in comparison to, e.g., conventional pipe flow; Poncet et al. [73] as well as many others observed powers for the Prandtl dependence of around 0.5 [74–78]. With respect to the rotational Reynolds number, dimensionless throughput and also aspect ratio dependence of the Nusselt number, several authors have observed different heat transfer regimes [41, 56, 79–82]. Pellé and Harmand [79], e.g., established four heat transfer regimes in analogy to the flow map of Daily and Nece [65] for the flow regimes in dependence of rotational Reynolds number and aspect ratio for rotor-side heat transport. However, since the knowledge on heat transfer in rotor-stator

cavities is not yet as comprehensive and coherent as on the flow regimes discussed in Section 2.1.2, further details on the different heat transfer studies are presented in the respective chapters of this thesis. The presented examples (Figures 2.6 to 2.8) display of course qualitative results found in the majority of studies on heat transfer in rotor-stator cavities, but should not be interpreted in the same way as the comprehensive theoretical background on the fluid flow in rotor-stator cavities, which has been researched more extensively.

2.1.4 Energy dissipation

As the studied RSSDR allows high rotational disc speeds, the energy dissipation induced in the fluid in the reactor gap needs to be considered. Daily and Nece [65] introduced a theoretical model describing the dissipative power input due to rotation for enclosed rotor discs; they express the tip-friction torque M as

$$M = C_m \frac{1}{2} \varrho \, \Omega^2 \, r_{\mathrm{r,o}}^5 \,, \tag{2.10}$$

with the momentum coefficient C_m. The latter depends on the flow regime indicated by the flow map (Figure 2.3 in Section 2.1.2). Since in the majority of this work operation conditions in the turbulent torsional-Couette regime are regarded, merely the momentum coefficient for this regime is presented (Equation (2.11)) [65].

$$C_m = \frac{0.08}{G^{1/6} \, Re_{\Omega}^{1/4}} \tag{2.11}$$

The dissipated power P_{rot} induced in the fluid in the reactor gap is calculated as [21]:

$$P_{\mathrm{rot}} = M \, \Omega \,. \tag{2.12}$$

The exemplary development of the dissipative power input due to rotation with water as reactor gap medium at 25 °C for an aspect ratio of $G = 0.0154$ for rotational disc speeds between $100\,\mathrm{min}^{-1}$ and $4000\,\mathrm{min}^{-1}$ is given in Figure 2.9. An exponential increase in power input with a rise in rotational Reynolds number is observed, meaning that an operational and a constructional limit of rotor-stator reactors is automatically given by the strong dependence of the dissipative power input on radius and rotation. This is because of the small volume of the reactor gap leading to high specific power inputs, which, in dependence of the material properties of the respective medium, would not allow good temperature control.

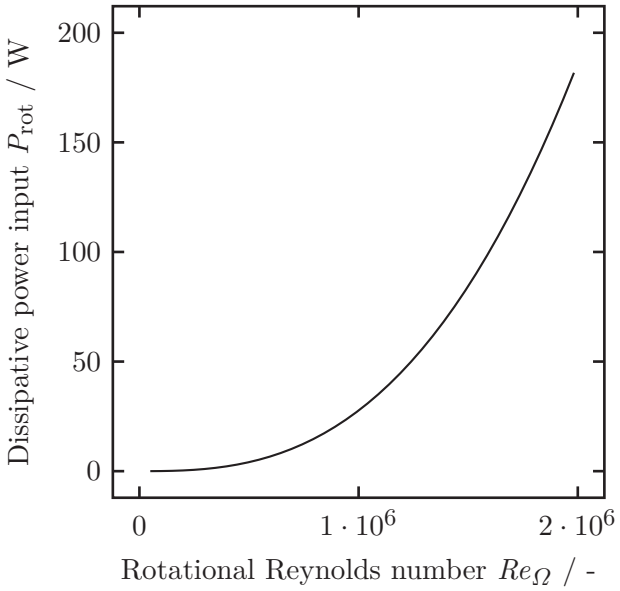

Figure 2.9: Dissipative power input due to rotation in dependence of rotational Reynolds number calculated according to Equations (2.10) to (2.12) for an aspect ratio of $G = 0.0154$ and water as reactor gap medium at $T = 25\,°C$. The material properties of water are calculated using the polynomials given in Appendix A.1.2.

2.2 Prilezhaev epoxidation

Parts of this section were published in a similar way as:

J. Kleiner, O. Hinrichsen, Epoxidation of methyl oleate in a rotor-stator spinning disc reactor. *Chem. Eng. Process.* 136 (2019) 152−162 [83].
Reprint with permission from *Elsevier*.

The epoxidation of olefins with peroxycarboxylic acids to form oxiranes is called Prilezhaev epoxidation [84]. In this reaction, acetic or formic acid (oxygen carrier) reacts in situ with hydrogen peroxide (oxygen donor) to form a peracid (cf. Figure 2.10) [85].

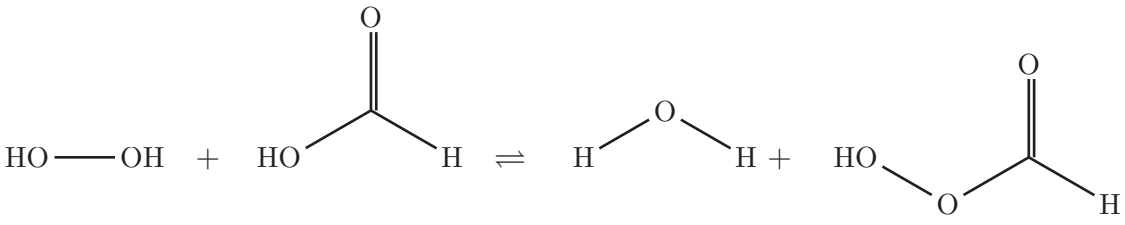

Figure 2.10: In situ generation of performic acid.

According to Chua et al. [85], the oxygen-oxygen bond of the peroxyacid is weak (ca. 35 kcal mol^{-1}), which is why it adopts a conformation with intramolecular hydrogen bonds when being in solution. Due to the high degree of polarization, an electrophilic

oxygen atom is present, which is able to add to an olefin [85]. In presence of an acid catalyst, the epoxidation takes place in a single step via the so called "butterfly" transition state (cf. Figure 2.11) [85]. In the transition state, oxygen addition and proton shifting happen simultaneously (cf. Figure 2.11); hence, this epoxidation always results in syn-stereospecifity, meaning that there is no structural rearrangement [85]. Thus, *cis* olefins yield *cis* epoxides and *trans* olefins yield *trans* epoxides, respectively [85–87]. In case the olefin has chiral centers, the double bond is attacked by the peroxyacid from the sterically less-hindered side [86, 87].

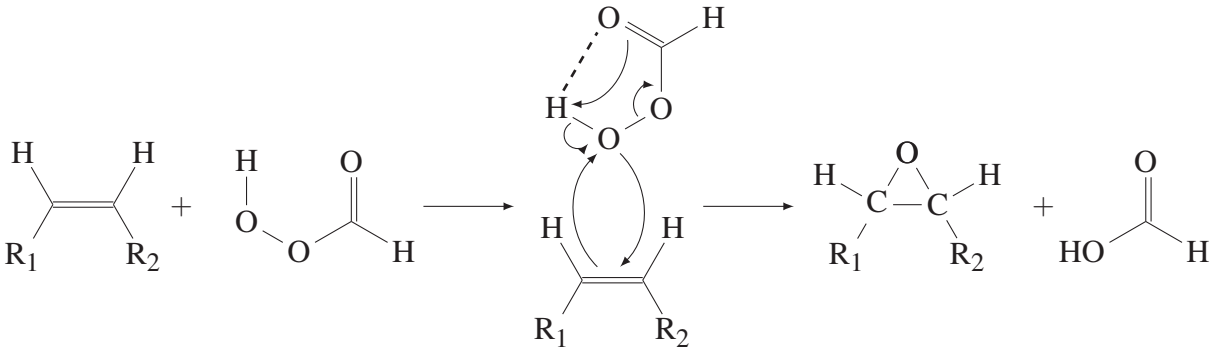

Figure 2.11: Prilezhaev epoxidation via "butterfly" transition state [85].

For an olefin with two different substituents, e.g., methyl oleate (Figure 2.12), four different epoxide isomers are possible; although the *cis* olefin yields high selectivities of one epoxide, the ratio of the diastereoisomers is more balanced for the *trans* epoxides [87]. The possible epoxide isomers resulting from epoxidation of either *cis* (Z) or *trans* (E) methyl oleate, respectively, are shown in Figure 2.13. The substituents R_1 and R_2 are the respective rests to the left- and right-hand side of the double bond in the methyl oleate molecule (Figure 2.12) and are depicted on the left side in Figure 2.13. In this work, the main educt is the *cis* isomer and the main product the (2*R*-*cis*) isomer or (2*R*,3*S*) isomer of methyl 8-(3-octyl-oxiran-2-yl)octanoate (Figure 2.13) also called *cis*-9,10-epoxystearic acid methyl ester (Figure 2.14). In the following, the terms methyl oleate (MO) referring to *cis*-9,10 methyl oleate will be used for the main educt and the term epoxidized methyl oleate (EMO) for the target product *cis*-9,10-epoxystearic acid methyl ester depicted in Figure 2.14.

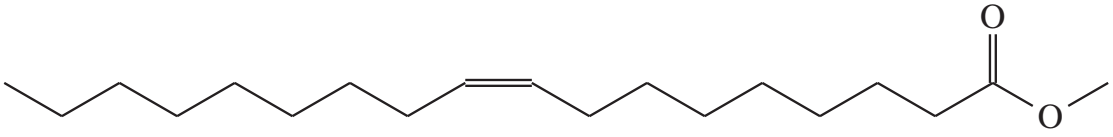

Figure 2.12: Methyl *cis* oleate also called oleic acid methyl ester.

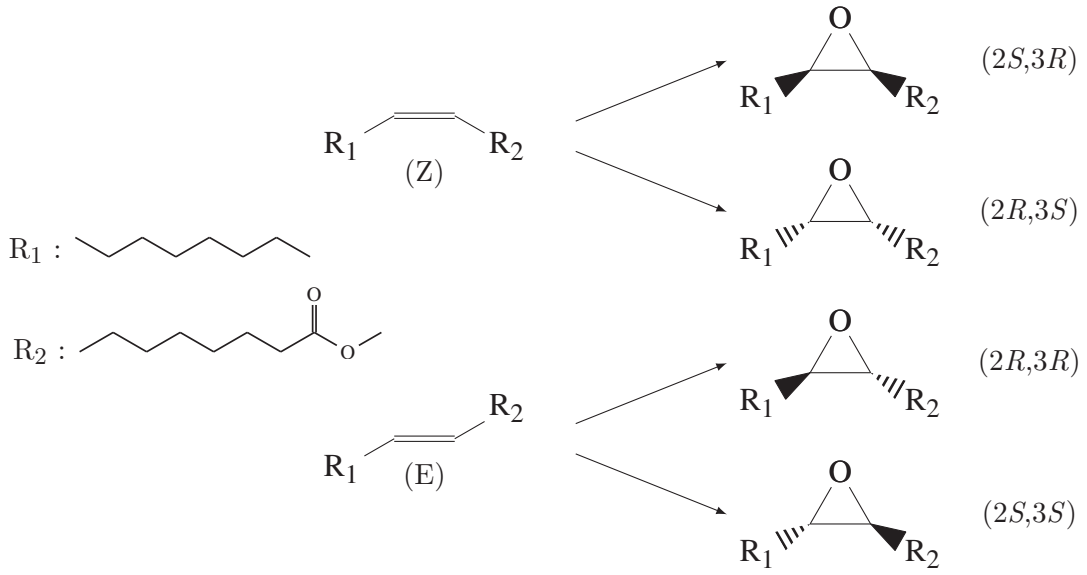

Figure 2.13: *Cis* and *trans* isomers of methyl oleate and methyl 8-((2 *,3 *)-3-octyl-oxiran-2-yl)octanoate also called methyl 9,10-epoxy-stearate (epoxidized methyl oleate). The superscript * is a placeholder for either R for "rectus" (right-handed) or S for "sinister" (left-handed).

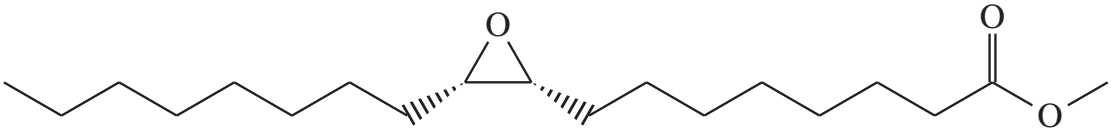

Figure 2.14: *cis*-9,10-epoxystearic acid methyl ester or methyl 8-((2R,3S)-3-octyl-oxiran-2-yl)octanoate.

In this work, the epoxidation of MO to EMO by the use of hydrogen peroxide and formic acid without any solvents is regarded. This means that it is a two-phase reaction and that sufficient mixing of two immiscible fluids is crucial. The reaction of a peracid with a carbon double bond is also very exothermic ($\Delta H_\mathrm{R} = -230.2\,\mathrm{kJ\,mol^{-1}}$ per double bond) [33], which means further that excellent temperature control is needed. As hydrogen peroxide is involved, it is also important to perform the reaction in a small and easily controllable reactor type, allowing high operational safety. These aspects make this reaction system an excellent example application to be carried out in the RSSDR studied in this work.

2.2.1 Possible side and consecutive reactions during the epoxidation of methyl oleate

During the epoxidation of MO, several side and ring opening reactions depending on the present reactants and reaction conditions may occur; especially the acidic character of, e.g., formic acid may lead to ring opening reactions, if present in very high amounts [35].

A variety of the most popular side and ring opening reactions is shown in the scheme in Figure 2.15.

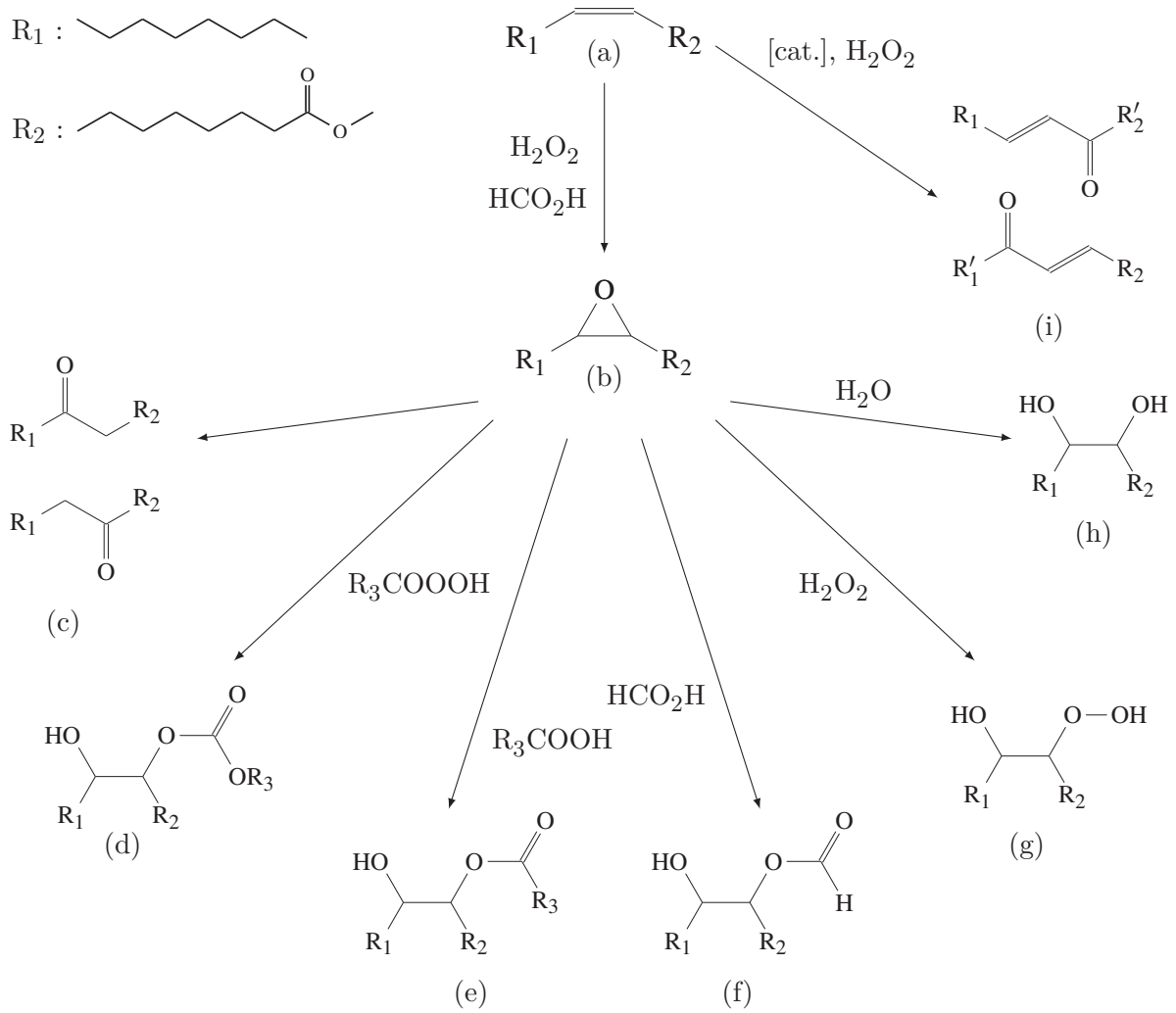

Figure 2.15: Possible epoxy ring opening reactions and side reactions, which may occur during the epoxidation of methyl oleate in presence of water, hydrogen peroxide, formic acid, performic acid and TiO_2 [35, 88–90]. The different molecules are: (a) methyl oleate, (b) epoxidized methyl oleate, (c) methyl oxo-ooctadecanoate, (d) oligomer, (e) oligomer, (f) methyl 9-(formyloxy)-10-hydroxy-octadecanoate, (g) methyl 9-hydro-peroxy-10-hydroxyoctadecanoate, (h) methyl 9,10-dihydroxy-octadecanoate and (i) methyl oxooctadecenoate. R_1 and R_2 are the respective hydrocarbon and ester rests of methyl oleate, R_1' and R_2' are R_1 and R_2 with one less carbon group each and R_3 is also a hydrocarbon/ester rest.

After the formation of the epoxide (compound (b) in Figure 2.15), methyl oxooctadecanoate (compound (c)) could be formed via oxirane ring rearrangement of the epoxide [89]. In the presence of hydroxyl groups, the oxirane ring may also react to oligomers (Figure 2.15 compounds (d) and (e)) as proposed by de Haro et al. [90]. Other epoxy ring opening reactions are the ones described by Omonov et al. [88], in which the epoxide reacts either with water or a carboxylic acid to form methyl 9,10-dihydroxy-octadecanoate

(Figure 2.15 compound (h)) or methyl 9-(formyloxy)-10-hydroxy-octadecanoate (compound (f)). In the presence of hydrogen peroxide, the epoxide may react to methyl 9-hydro-peroxy-10-hydroxyoctadecanoate (Figure 2.15 compound (g)). Hydrogen peroxide may also react with the olefin, often in presence of a heterogeneous catalyst [88], to form methyl oxooctadecenoate (Figure 2.15 compound (i)). Reaction parameters such as temperature, hydrogen peroxide and acid amount, reaction time as well as a catalyst influence whether the epoxide is selectively formed or side and ring opening reactions occur strongly. Many authors report that temperatures should be between 60 °C and 75 °C [32, 35, 88], to avoid a lot of ring opening, hydrogen peroxide and peroxyacid decay. Also, very acidic reaction mixtures are further beneficial for ring opening reactions [35]. Hydrogen peroxide may cause side and ring opening reactions, but it needs to be present abundantly, to compensate its loss due to decomposition caused by too high temperatures and moreover, to ensure the epoxidation reaction reaches completion [88]. Thus, a compromise for the respective parameters needs to be applied, to on the one hand guarantee fast epoxidation at high selectivities and on the other hand avoid excessive side and consecutive reactions.

3 Single-phase stator-side heat transfer in a rotor-stator spinning disc reactor

This chapter was published in a similar way as:

J. Kleiner, F. Haseidl, O. Hinrichsen. Rotor-Stator Spinning Disc Reactor: Characterization of the Single-Phase Stator-Side Heat Transfer. *Chem. Eng. Technol.* 40 (11) (2017) 2123−2133 [91].
Reprint with permission from *WILEY-VCH Verlag GmbH & Co. KGaA*.

3.1 Abstract

This chapter deals with the examination of the single-phase fluid-stator heat transfer in a rotor-stator spinning disc reactor (RSSDR) in dependence of rotational Reynolds number, dimensionless throughput, Prandtl number and aspect ratio. For the selected ranges of these parameters, an increase in the stator-side Nusselt number with increasing Reynolds number, Prandtl number and a higher throughput is found. Laminar and turbulent flow regions are observed, which coincide with a throughput- and a rotation-governed heat transfer regime, respectively. A Nusselt correlation to predict the experimental data in the turbulent flow regime within 20 % accuracy was established. A distinct increase in the overall volumetric heat transfer coefficient for a rise in rotational Reynolds number was observed, being considerably higher compared to conventional tube reactors and twice as large in contrast to a similar rotor-stator setup.

3.2 Introduction

Process intensification (PI) aims at the improvement of chemical processes in terms of reducing capital cost, increasing environmental aspects, energy efficiency and operational safety by means of integrating innovative technologies and drastically reducing equipment size [17, 92, 93]. To overcome heat transfer limitations is one key aspect in PI [93], as for example insufficient heat removal during a reaction can lead to thermal runaways or a

decrease in selectivity. The RSSDR is a novel reactor technology, which was engineered for the intensification of chemical processes and especially addresses intensification of heat and mass transfer limited reactions. The reactor consists of a rotor enclosed within a cylindrical housing. The distance between the rotating and static parts is a few millimeters, whereas the rotor radius ranges between 60 mm and 140 mm. Due to high rotational disc speeds of the rotor, which reach about $4000\,\mathrm{min}^{-1}$, and the small gap height, high shear forces are induced in the fluid within the gap. In dependence of the throughput through the gap, rotational disc speed and the aspect ratio, turbulences and the formation of different flow regimes are caused [23, 27]. This in turn influences the heat and mass transfer properties of the rotor-stator reactor.

Several studies of mass and heat transfer properties as well as hydrodynamics on rotor-stator reactors have already been performed. Meeuwse et al. [22, 26, 27] examined gas-liquid mass transfer properties of RSSDRs and found the volumetric mass transfer coefficient to be significantly higher compared to conventional reactors such as bubble columns, which was also observed by Haseidl et al. [9]. Visscher et al. [45] studied liquid-liquid flow behavior and liquid-liquid mass transfer coefficients, while Meeuwse et al. [39] investigated a multistage rotor-stator reactor and demonstrated that a rotor-stator spinning disc reactor could be easily scaled-up and each stage of the multi-stage rotor-stator reactor could be regarded as a single RSSDR.

Studies on liquid-solid mass transfer effects of the oxidation of glucose in a rotor-stator reactor reveal mass transfer coefficients which are about one magnitude higher compared to packed beds [9, 25]. Experiments on the residence time behavior were first conducted by Visscher et al. [40], who introduced a reactor model based on a plug flow region and two to three tanks in series. Later de Beer et al. [31] proposed a slightly different reactor model for the RSSDR consisting of a plug flow region and only one stirred tank reactor. The latter model was validated for different setups of rotor-stator reactors and a broader parameter range by Haseidl et al. [42]. The micromixing properties of the RSSDR were further examined by Haseidl et al. [23].

Regarding the studies performed on heat transfer on rotor-stator systems, research varies greatly, as very different setups were examined from free discs [74, 82], enclosed rotor-stator systems [81, 94], (partially) open cavities [74, 79, 95] without superimposed throughput [79, 95, 96] and with throughput [67, 74, 97]. Moreover, only little research has focused on closed rotor-stator cavities with superimposed throughput, yet [21, 29, 30, 50].

Owen et al. [74] for example studied heat transfer of a free disc as well as a disc rotating near a stator without any coolant flow for $2 \cdot 10^5 \leq Re_\Omega \leq 4 \cdot 10^6$ and $0.0067 \leq G \leq 0.18$ and with coolant flow for $0.0067 \leq G \leq 0.18$ and $1.4 \cdot 10^4 \leq C_W \leq 1 \cdot 10^5$; they found the Nusselt number to be independent from the aspect ratio for large aspect ratios and for $C_W/(2\,\pi\,G\,Re_\Omega) > 1.7$ correlating with $(C_W/G)^{0.8}$. Owen [98] further investigated,

whether the Reynolds analogy could be applied to a rotor near a stator with and without superimposed throughput.

Nikitenko [81] performed experiments on an air filled enclosed rotor-stator system for $0.018 \leq G \leq 0.085$ and rotational Reynolds numbers $Re_\Omega \leq 1 \cdot 10^6$ and found no effect of the aspect ratio on the Nusselt number. Similar experiments of Shchukin and Olimpiev [94] for an aspect ratio of $G = 0.0646$ confirmed this observation.

Djaoui et al. [67] regarded a setup with a small aspect ratio and an inward flow and presented temperature distributions as well as local Nusselt number correlations. Poncet et al. [73] regarded a rotor-stator cavity with superimposed throughput for $5 \cdot 10^5 \leq Re_\Omega \leq 1.44 \cdot 10^6$, $0 \leq C_W \leq 12082$, $0.036 \leq G \leq 4/9$ and Prandtl numbers between $1 \leq Pr \leq 12$. They compared their findings with the experimental results of Djaoui et al. [67] and established a stator-side Nusselt correlation for a broad parameter range based on their numerical results in dependence of Prandtl number, dimensionless throughput and rotational Reynolds number.

Kapinos [99] examined heat transfer of a disc rotating in a housing for aspect ratios $0.016 \leq G \leq 0.06$ and rotational Reynolds numbers between $5 \cdot 10^5 \leq Re_\Omega \leq 4 \cdot 10^6$ and found the Nusselt number to be dependent on Reynolds number, throughput and aspect ratio. A dependence of the Nusselt number on the aspect ratio was further seen by Boutarfa and Harmand [75] and Yuan et al. [96].

Pellé and Harmand [79] performed an experimental study on heat transfer in an opened rotor-stator air gap for rotational Reynolds numbers between $1.29 \cdot 10^5 \leq Re_\Omega \leq 6.45 \cdot 10^5$ and aspect ratios between 0.01 and 0.16 and identified four heat transfer regimes. They extended their research on a rotor-stator system with axial inflow for $2 \cdot 10^4 \leq Re_\Omega \leq 5.16 \cdot 10^5$ and a throughflow Reynolds number between 0 and 41666 [97].

For a rotor-stator disc system with electrical heating and radial outflow of air, Howey et al. [95] examined the stator-side heat transfer within the parameter range $3.7 \cdot 10^4 \leq Re_\Omega \leq 5.6 \cdot 10^5$ and $0.0106 \leq G \leq 0.0297$. They regarded local Nusselt numbers at three different radii and observed a transition in flow from laminar to turbulent [95]. Laminar and turbulent flow regimes were also seen by Yu et al. [100] who conducted experiments on a shrouded parallel disc system with coolant throughput for aspect ratios between 0.22 and 2 and rotational disc speeds ranging from $500\,\mathrm{min}^{-1}$ to $3700\,\mathrm{min}^{-1}$ [100]. By means of applying the analogy between mass and heat transfer, Kreith et al. [101] investigated heat and mass transfer of an enclosed rotating disc with and without a superimposed throughput; similar to Howey et al. [95] they observed laminar, transition and turbulent flow regimes.

De Beer et al. [21] examined the single-phase stator-side heat transfer coefficient in an RSSDR in the parameter range $0 \leq Re_\Omega \leq 12 \cdot 10^5$ and $211 \leq C_W \leq 421$ for the aspect ratios 0.017 and 0.03. They observed a rotation-governed heat transfer regime

for rotational Reynolds numbers $Re_\Omega > 0.2 \cdot 10^5$ and a throughput-governed regime for lower rotational Reynolds numbers and observed only an influence of the aspect ratio and the dimensionless throughput in the throughput-governed region. The fluid-rotor heat transfer coefficient was studied by de Beer et al. [29] in a stator-rotor-stator spinning disc reactor for rotational disc speeds between 0 and 157 rad s^{-1} and volumetric throughputs ranging from $15 \cdot 10^{-6}\,\mathrm{m^{-3}\,s^{-1}}$ to $20 \cdot 10^{-6}\,\mathrm{m^{-3}\,s^{-1}}$.

Despite all the different researches on heat transfer available in literature, however, no comprehensive study on single-phase stator-side heat transfer in RSSDRs covering influence factors such as rotational Reynolds number, dimensionless throughput, a variation in Prandtl number and aspect ratio has been conducted, yet. Especially, the influence of the Prandtl number on heat transfer in RSSDRs is not fully understood. Therefore, variation of the Prandtl number is one key aspect of this study, besides a variation in rotational disc speed, superimposed throughput and aspect ratio.

3.3 Theoretical background

3.3.1 Rotor-stator reactor model

The reactor model for the evaluation of the heat transfer experiments is the engineering model for single-phase flow in a multi-stage rotor-stator spinning disc reactor by de Beer et al. [31]. Figure 3.1 shows a schematic of the single-stage rotor-stator reactor used for this study illustrating the applied reactor model. The rotor-stator reactor is regarded as two plug flow regions at lower radial positions, one in the upper and one in the lower gap, and a continuous stirred region connecting the two plug flow regions at higher radial positions [31]. The plug flow region is governed by the superimposed throughput and features an either centripetal or centrifugal radial velocity profile depending on the superimposed flow direction [58, 64, 102]. On the contrary, rotation governs the ideally stirred region, which shows a radial velocity profile with both centripetal and centrifugal flow; at the rotor side, a centrifugal boundary layer develops, whereas a centripetal boundary layer is present at the stator side [64]. The transition radius r_{trans} (Equation (2.4) [31]) indicates the transition between plug flow and continuous stirred regions. As described in Section 2.1.2, the transition radius depends on rotational Reynolds number Re_Ω (Equation (2.1)) and dimensionless throughput C_W (Equation (2.3)). The parameter $c_{\mathrm{trans}} = 0.219$ for aspect ratios $G \geq 0.038$ (Equation (2.2)) and for $G < 0.038$ $c_{\mathrm{trans}} = 8.4 \cdot 10^{-4} \exp(146.6\,G)$ (Equation (2.5)) [31].

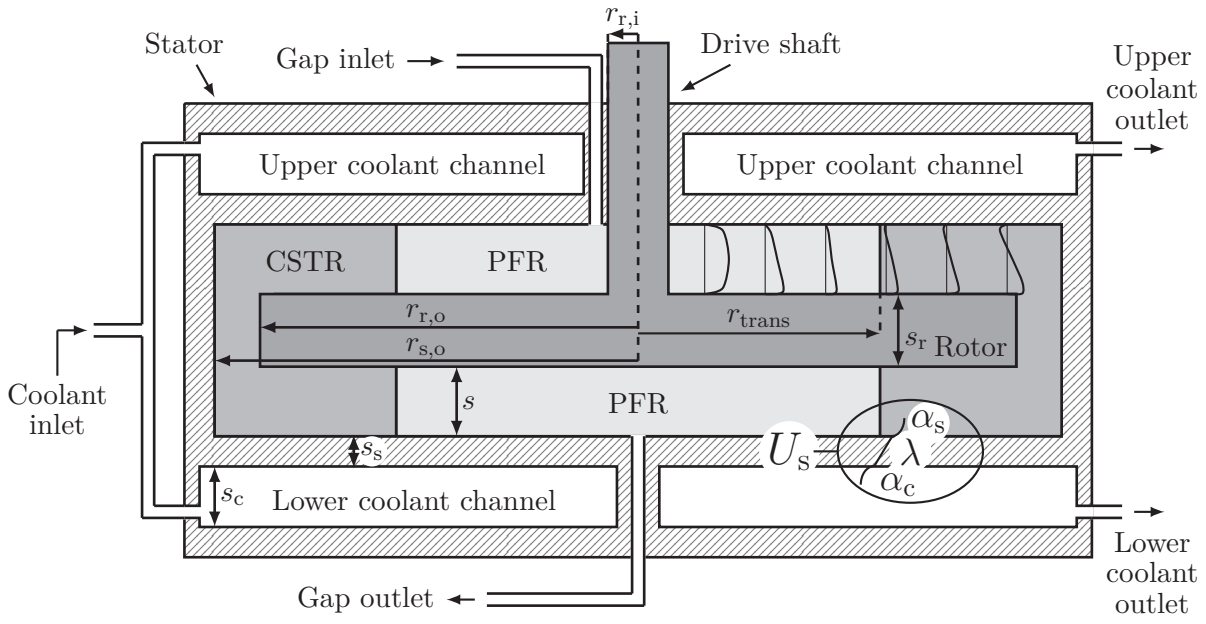

Figure 3.1: Schematic of the rotor-stator reactor. The reactor gap is considered, according to the proposed reactor model by de Beer et al. [31], as two plug flow regions and a continuous stirred region connecting the upper and lower plug flow region. The transition radius r_{trans} indicates the transition between the two regions. Radial velocity profiles in the upper reactor gap illustrate the centrifugal flow profile in the plug flow region as well as the centrifugal, respectively, the centripetal boundary layer at the rotor respectively stator side for the continuous stirred region [64]. The regarded overall heat transfer coefficient between reactor gap and coolant channels in the stator walls is shown in the lower right part of the reactor schematic.

In this work, rotor-stator reactors with aspect ratios of $G = 0.0154$ and $G = 0.0074$ were examined, meaning that according to the flow map introduced by Daily and Nece [65] almost all measurements are within the torsional-Couette regime and the parameter c_{trans} is calculated using Equation (2.5).

3.4 Applied heat transfer model

The applied heat transfer model to determine the overall heat transfer coefficient of the studied reactor setups is based on the reactor model by de Beer et al. [31], described in Section 3.3.1. Differential enthalpy balances are established for the upper and lower plug flow region of the reactor, whereas an algebraic enthalpy balance applies for the ideally stirred region connecting the upper and lower plug flow region. In the following, the deduced enthalpy balance for the upper plug flow region is exemplarily presented. Figure 3.2 shows the system boundaries of a differential element in the upper reactor gap with the considered enthalpy flows.

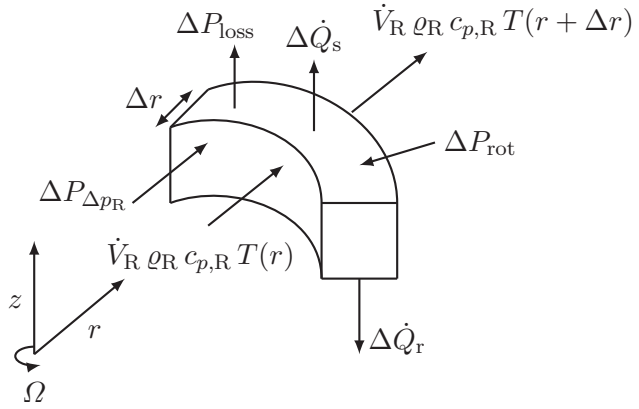

Figure 3.2: Differential element of the upper reactor gap with the considered enthalpy flows. Axial and tangential convective heat flows are neglected because of the plug flow region being axially and tangentially well mixed [21, 64].

Conduction through the rotor is neglected for the setup with an aspect ratio of $G = 0.0154$, since the rotor's heat transfer resistance is very high compared to the stator-side resistance. The small rotor consists of two 3 mm thick steel plates ($\lambda_{\text{steel}} = 16\,\text{W}\,\text{m}^{-1}\,\text{K}^{-1}$) that enclose a 2 mm air gap ($\lambda_{\text{air}} = 0.0262\,\text{W}\,\text{m}^{-1}\,\text{K}^{-1}$) (cf. Figure 3.3a). This results in a thermal resistance $R_{\text{th}} \approx 5.8\,\text{K}\,\text{W}^{-1}$ compared to a mean thermal resistance through the stator of $R_{\text{th}} \approx 0.05\,\text{K}\,\text{W}^{-1}$. For the setup with an aspect ratio of $G = 0.0074$, however, conduction through the rotor is not negligible. This is because the large rotor has almost the same core as the rotor for the small setup, but has an aluminum alloy ($\lambda_{\text{alu}} = 112\,\text{W}\,\text{m}^{-2}\,\text{K}^{-1}$) disc surrounding the small rotor adapter (cf. Figure 3.3b).

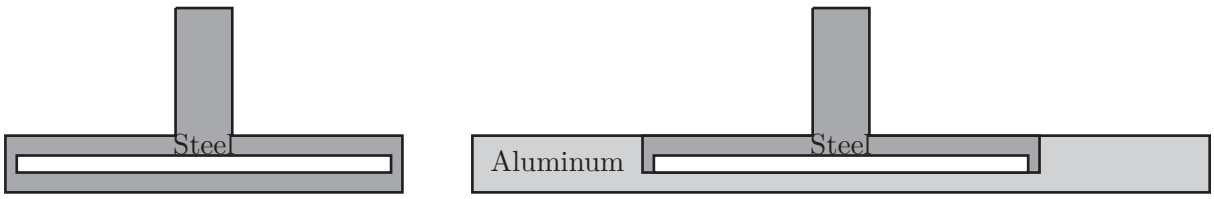

(a) $G = 0.0154$. **(b)** $G = 0.0074$.

Figure 3.3: Schematics of the rotor discs. The rotor of the setup shown in (a) consists of two 3 mm steel plates, which enclose a 2 mm air gap. The rotor in (b) on the other hand consists of a 3 mm steel plate, a 2 mm air gap and a 3 mm aluminum alloy layer at $r \leq 65$ mm and for $r > 65$ mm the rotor consists entirely of an aluminum alloy.

The overall heat transfer coefficient through the rotor for the setup with $G = 0.0074$ is therefore divided into two parts (first part: $r \leq 65$ mm and second part: $r > 65$ mm) with two different overall conductivities.

The limit of the overall heat transfer coefficient U_{limit} in the two considered rotor-stator systems given by the external heat transfer coefficient through the coolant channels is

determined via the measurements at the setup where $G = 0.0154$ with the relation for the overall heat transfer coefficient

$$U_\mathrm{s} = \frac{1}{\frac{1}{\alpha_\mathrm{s}} + \frac{s_\mathrm{s}}{\lambda_\mathrm{alu}} + \frac{1}{\alpha_\mathrm{c}}} = \frac{1}{\frac{1}{\alpha_\mathrm{s}} + \frac{1}{U_\mathrm{limit}}} \tag{3.1}$$

The unknown variables in Equation (3.1) are the stator- and coolant-side heat transfer coefficient α_s and α_c, respectively, and the thickness of the layer in the stator between reactor gap and coolant channels s_s.

U_limit is then used in the enthalpy balances for the setup with $G = 0.0074$, thus allowing to directly determine the heat transfer coefficient in the reactor gap. For the heat transfer term through the rotor for the setup with $G = 0.0074$, the rotor-side heat transfer coefficient is assumed to be the same as the stator-side heat transfer coefficient. This assumption was first made by de Beer et al. [21] who showed that this simplification does not introduce large errors. An estimation of the introduced error with the rotor-side heat transfer coefficient being 18 % larger compared to the stator-side heat transfer coefficient as shown by Nikitenko [81] revealed an average deviation of 4 % of the heat transfer coefficient.

As the plug flow region is axially and tangentially well mixed [21, 64], convective heat flows in axial and tangential direction are neglected. Adding up all heat flows of Figure 3.2 the following enthalpy balance for the steady-state results:

$$V_\mathrm{R}\varrho_\mathrm{R}\, c_{p,\mathrm{R}} \frac{\mathrm{d}T}{\mathrm{d}t} = 0 = -\dot{V}_\mathrm{R}\, \varrho_\mathrm{R}\, c_{p,\mathrm{R}} \frac{\mathrm{d}T}{\mathrm{d}r}\Delta r + \Delta P_\mathrm{rot} + \Delta P_{\Delta p_\mathrm{R}} - \Delta P_\mathrm{loss} - \Delta\dot{Q}_\mathrm{s} - \Delta\dot{Q}_\mathrm{r}. \tag{3.2}$$

The dissipative power input due to rotation is given by Equation (3.3)

$$\Delta P_\mathrm{rot} = \frac{1}{2}\frac{\mathrm{d}P_\mathrm{rot}}{\mathrm{d}r}\Delta r + \ldots = \frac{14}{6}\frac{P_\mathrm{rot}}{r_\mathrm{s,o}^{14/3}} r^{11/3}\,\Delta r \tag{3.3}$$

with P_rot being the experimentally measured overall power input. Radial dependence results from the momentum coefficient C_m for the turbulent torsional-Couette regime according to Daily and Nece [65], which is given in Equation (2.11) in Section 2.1.4. With the definition of the torque (Equation (2.10)) and the overall dissipative power input, given in Equation (2.12) in Section 2.1.4, the radial dependence of the dissipative power input can be expressed as:

$$P_\mathrm{rot} = C\, r^{14/3}, \tag{3.4}$$

with the proportionality constant C.

Dissipation by means of pressure drop Δp is calculated via the Bernoulli equation [103] and contributes by volume of the discretization element to the enthalpy balance:

$$\Delta P_{\Delta p_\mathrm{R}} = \frac{\dot{V}_\mathrm{R}\,\Delta p_\mathrm{R}\,r\Delta r}{r_\mathrm{s,o}^2}. \tag{3.5}$$

The same applies for heat loss to the environment:

$$\Delta P_\mathrm{loss} = \frac{P_\mathrm{loss}\,r\,\Delta r}{r_\mathrm{s,o}^2}. \tag{3.6}$$

The variable $r_\mathrm{s,o}$ stands for the outer radius of the stator.

Heat removal through the stator walls is calculated with a constant overall heat transfer coefficient U_s and the arithmetic mean of the coolant inlet and outlet temperatures $\bar{T}_\mathrm{C,u}$ with the index "u" denominating the upper gap part:

$$\Delta\dot{Q}_\mathrm{s} = U_\mathrm{s}\,2\,\pi\,r\,\Delta r\,(T_\mathrm{u}(r) - \bar{T}_\mathrm{C,u})\,. \tag{3.7}$$

As stated before, for the large setup, heat transfer through the rotor is not negligible. Thus, another term is to be considered in the enthalpy balance with the index "l" for the lower gap part.

$$\Delta\dot{Q}_\mathrm{r} = U_\mathrm{r}(r)\,2\,\pi\,r\Delta r\,(T_\mathrm{u}(r) - T_\mathrm{l}(r)) \tag{3.8}$$

with U_r being

$$U_\mathrm{r} = \frac{1}{\dfrac{2}{\alpha_\mathrm{s}} + \sum_i \dfrac{s_i}{\lambda_i}}. \tag{3.9}$$

The term $\sum_i s_i/\lambda_i$ considers contributions from the materials steel, aluminum alloy and air for $r \leq 65\,\mathrm{mm}$ and only aluminum alloy for $r > 65\,\mathrm{mm}$.

Taking into account the above made considerations, the differential equation for the temperature in the plug flow region of the upper reactor gap results in

$$\begin{aligned}\frac{\mathrm{d}T}{\mathrm{d}r} =& \frac{\dfrac{14}{6}\dfrac{P_\mathrm{rot}}{r_\mathrm{s,o}^{14/3}}r^{\frac{11}{3}} - \dfrac{P_\mathrm{loss}\,r}{r_\mathrm{s,o}^2} + \dfrac{\dot{V}_\mathrm{R}\,\Delta p_\mathrm{R}\,r}{r_\mathrm{s,o}^2} - U_\mathrm{s}\,2\,\pi\,r\,(T_\mathrm{u}(r) - \bar{T}_\mathrm{C,u})}{\dot{V}_\mathrm{R}\,\varrho_\mathrm{R}\,c_{p,\mathrm{R}}} \\ &- \frac{U_\mathrm{r}(r)\,2\,\pi\,r\,(T_\mathrm{u}(r) - T_\mathrm{l}(r))}{\dot{V}_\mathrm{R}\,\varrho_\mathrm{R}\,c_{p,\mathrm{R}}}\end{aligned} \tag{3.10}$$

with $U_\mathrm{r} = 0$ for $G = 0.0154$. The differential equations for the upper and lower gap are solved using the *bvp4c* boundary condition solver from MATLAB®. The reactor

gap inlet and outlet temperatures as well as the enthalpy balance for the ideally stirred region serve as boundary conditions. The stator-side overall heat transfer coefficient is the fitting parameter for the experiments at the setup with $G = 0.0154$, whereas the stator-side heat transfer coefficient is directly fitted for the setup with $G = 0.0074$. In case the transition radius is larger than the outer rotor radius, the upper and lower gaps are entirely considered as plug flow regions [21].

3.5 Experimental section

3.5.1 Experimental setup

The rotor-stator setup used for the current work is schematically depicted in Figure 3.1 with the most important geometric parameters. The rotor radius is either $r_{\mathrm{r,o}} = 65\,\mathrm{mm}$ (for $G = 0.0154$) or $135\,\mathrm{mm}$ (for $G = 0.0074$), while the gap height remains always $s = 1\,\mathrm{mm}$. The radius of the drive shaft in the upper coolant channel is $r_{\mathrm{r,i}} = 11\,\mathrm{mm}$, radial clearance between stator housing and outer rotor radius values $r_{\mathrm{s,o}} - r_{\mathrm{r,o}} = 1.5\,\mathrm{mm}$ and the rotor height is $s_{\mathrm{r}} = 8\,\mathrm{mm}$. The stator wall between reactor gap and coolant channels is $s_{\mathrm{s}} = 3\,\mathrm{mm}$ thick. The coolant channels have a cross section of 5 mm times 5 mm and traverse the stator parts in meanderings (similar to the setup used by de Beer et al. [21]) separated by 2 mm thick and 5 mm high fins. The reactor volumes correspond to $V(G = 0.0154) = 3.25 \cdot 10^{-5}\,\mathrm{m}^3$ and $V(G = 0.0074) = 1.2693 \cdot 10^{-4}\,\mathrm{m}^3$ and the heat exchange areas $A(G = 0.0154) = 0.0274\,\mathrm{m}^2$ and $A(G = 0.0074) = 0.1167\,\mathrm{m}^2$.

A schematic flow diagram of the setup for the experiments is shown in Figure 3.4. Coolant (deionized (DI) water) and reactor gap media (DI water/glycerol mixtures) are supplied and tempered by two thermostats (*Haake* DC50 and *Julabo* MP). The medium flowing through the reactor gap is pumped by an *ISMATEC* tooth wheel pump (type BVP-Z) and controlled by a mini CORI-FLOW mass flow controller by *Bronkhorst* (type M15-ABD-33-O-S). A reciprocal diaphragm VERDERBAR pump (type *Wanner* HydraCell G03-E), controlled by an in-house control implemented in LabVIEW®, pumps the coolant medium. Inlet and outlet temperatures of the respective media are measured with type J thermocouples (NI USBTC01, *Texas Instruments*), which are calibrated with a high accuracy thermometer *ISOTECH* (TTI-10) with an accuracy of $\pm 0.012\,\mathrm{K}$. The maximum deviation of the thermocouple calibration is 0.16 K, resulting in a maximum deviation of $\pm 0.172\,\mathrm{K}$ for the thermocouples. For pressure measurements, a precision manometer (*ASHCROFT* 160 T5510) with an accuracy of $\pm 0.6\,\%$ in a measurement range of $0 - 1\,\mathrm{bar}$ was used. A *LENZE* SE RS100 motor powers the rotor and the output motor power is measured. A 10 mm *Armaflex* layer insulates the stator parts and a 14 mm hose insulation from *Julabo* insulates all pipes.

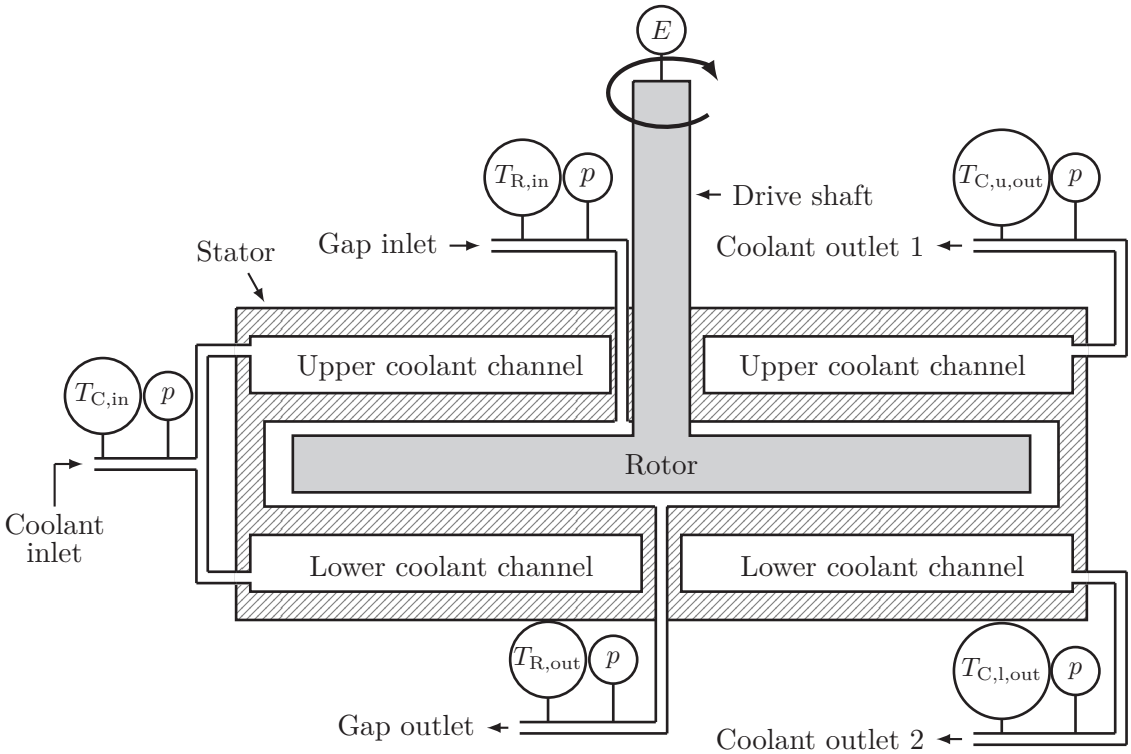

Figure 3.4: Schematic flow diagram of the rotor-stator spinning disc reactor. Reactor gap and coolant media are supplied and tempered by two thermostats and pumped with a tooth wheel pump and a diaphragm pump, respectively. Inlet and outlet temperatures of coolant and reactor circuit are measured using type J thermocouples and for pressure measurements, a precision manometer is used. A *LENZE* motor powers the rotor and its output power is monitored.

3.5.2 Measurement procedure

For determination of the heat transfer rates in this study, enthalpy balances for the coolant channels and the reactor gap were established. The throughput in the coolant channels was kept constant at $\dot{V}_{C,i} = 1.73 \cdot 10^{-5}\,m^3\,s^{-1}$ for the upper and lower channel, respectively. The coolant inlet temperature was set to $T_{C,in} = 25\,°C$ for all experiments, which was close to the ambient temperature in order to reduce heat loss. The reactor-side throughput varied between $\dot{V}_R = 3.88 \cdot 10^{-6}\,m^3\,s^{-1}$ and $\dot{V}_R = 2.40 \cdot 10^{-5}\,m^3 s^{-1}$ corresponding to dimensionless throughputs of $C_W = 100$ and 450 for the setup with $G = 0.0154$. For $G = 0.0074$, the gap throughput ranged between $\dot{V}_R = 4.90 \cdot 10^{-6}\,m^3\,s^{-1}$ and $\dot{V}_R = 2.26 \cdot 10^{-5}\,m^3\,s^{-1}$ ($C_W = 60$ and $C_W = 232$). Rotational disc speeds varied from $n = 40\,min^{-1}$ to $n = 3900\,min^{-1}$ for $G = 0.0154$ and from $n = 40\,min^{-1}$ to $n = 1500\,min^{-1}$ for $G = 0.0074$, resulting in rotational Reynolds numbers ranging from $Re_\Omega = 1.1 \cdot 10^4$ to $Re_\Omega = 2.7 \cdot 10^6$. The reactor inlet temperature was constantly set at $T_{R,in} = 54\,°C$.

Material properties, in order to vary the Prandtl number (Equation (2.6) in Section 2.1.3) of the gap medium, were varied using DI water/glycerol mixtures with the following mass fractions of glycerol: $w_{gly} = 0.00$, $w_{gly} = 0.18$, $w_{gly} = 0.32$, $w_{gly} = 0.41$.

The mass fractions of each solution were measured with an *Anton Paar GmbH* DMA 100 M fluid density meter with an accuracy of $0.001\,\mathrm{g\,cm^{-3}}$. For calculation of the material properties of coolant and reactor gap medium, the arithmetic mean of the respective inlet and outlet temperatures was used. The correlations for the material properties itself were retrieved from the NIST databank and are given in Appendix A.1.2.

If the enthalpy balance (Equation (3.11)) of a measurement could not be closed within $\pm 10\,\%$ of the heat transfer rate, the measurement was discarded. The same applied, if the temperature difference between reactor outlet and lower coolant channel outlet of an experiment was lower than $\Delta T = T_{\mathrm{R,out}} - T_{\mathrm{C,l,out}} < 0.3\,\mathrm{K}$.

$$\begin{aligned} V_{\mathrm{R}}\,\varrho_{\mathrm{R}}\,c_{p,\mathrm{R}}\frac{\mathrm{d}T}{\mathrm{d}t} = 0 =& \dot{V}_{\mathrm{R}}\,\varrho_{\mathrm{R}}\,c_{p,\mathrm{R}}(T_{\mathrm{R,in}} - T_{\mathrm{R,out}}) + \dot{V}_{\mathrm{C}}\,\varrho_{\mathrm{C}}\,c_{p,\mathrm{C}}(T_{\mathrm{C,in}} - \bar{T}_{\mathrm{C,out}}) \\ &+ P_{\mathrm{rot}} + P_{\Delta p_{\mathrm{R}}} + P_{\Delta p_{\mathrm{C}}} - P_{\mathrm{loss}} \end{aligned} \tag{3.11}$$

Repeatability of the measurements was ensured by performing many experiments in duplicate and some even in triplicate. The uncertainty of the determined overall heat transfer coefficient was estimated via error propagation considering the temperatures, the volumetric throughput, pressure drop, heat loss to the environment as well as the dissipative power input as error inducing quantities. This revealed a maximum uncertainty of about 8 % for the small setup while the average is about 7 % and for the large setup a maximum uncertainty of 13 % with the average being 8 %.

The enthalpy balance in Equation (3.11) includes influences of convective heat transfer flows, dissipation due to pressure drop on coolant- and reactor gap-side and rotation as well as heat loss to the environment. The evaluation of the four latter contributions to the enthalpy balance is discussed within the first part of the results and discussion section (Section 3.6.1).

Heat loss to the environment

Heat loss to the environment was measured by introducing liquid at different temperatures into the reactor gap, while keeping the coolant flow at zero and measuring the outlet temperature of the medium flowing through the gap as well as the ambient temperature [21].

Dissipative power input

Pressure drop

Pressure drop across reactor gap and coolant channels was measured with the precision manometer described in Section 3.5.1, which was located at the respective inlets, while keeping the outlets open to atmosphere. For the reactor gap-side pressure drop, measurements at different dimensionless throughputs ($C_W = 130 - 300$), temperatures ($T_{\mathrm{R,in}} = 20 - 54\,^{\circ}\mathrm{C}$) and rotational Reynolds numbers ($Re_{\Omega} = 0 - 2.5 \cdot 10^6$) were performed with the two different setups.

Rotational energy dissipation

The rotational power input induced by the rotor is determined by measuring the effective output power of the motor first with air inside the reactor gap and second with liquid. The difference between the measured output power P with liquid and air gives the dissipative power input induced in the fluid P_{rot}.

$$P_{\mathrm{rot}} = P_{\mathrm{liq}} - P_{\mathrm{air}} \tag{3.12}$$

Alternatively, the dissipative power input was determined via a direct method, similar to de Beer et al. [21]. Liquid at a temperature of 23 °C entered the reactor gap as well as the coolant channels and the outlet temperatures were measured. Thus, the dissipative power input was calculated via convective terms of the reactor gap and coolant channels and heat loss to the environment.

$$P_{\mathrm{rot}} = \left| \dot{V}_{\mathrm{R}}\, \varrho_{\mathrm{R}}\, c_{p,\mathrm{R}}\, (T_{\mathrm{R,in}} - T_{\mathrm{R,out}}) + \dot{V}_{\mathrm{C}}\, \varrho_{\mathrm{C}}\, c_{p,\mathrm{C}}\, (T_{\mathrm{C,in}} - \overline{T}_{\mathrm{C,out}}) \right| + P_{\mathrm{loss}} \tag{3.13}$$

3.6 Results and discussion

3.6.1 Preliminary results for determination of the heat transfer in a rotor-stator spinning disc reactor

Heat loss to the environment

Based on the measurements for the determination of heat loss to the environment, heat loss to the environment was determined via the enthalpy difference between in- and outlet of the reactor gap. Empirical correlations for the heat loss in dependence of the difference between reactor gap inlet and ambient temperature T_{amb} were established, which are given in Appendix A.1.1.

Dissipative power input

Pressure drop

Pressure drop for each of the coolant channels for $G = 0.0074$ values $\Delta p_{\mathrm{C},i} = 0.142\,\mathrm{bar}$ and for $G = 0.0154$ $\Delta p_{\mathrm{C},i} = 0.085\,\mathrm{bar}$. The resulting dissipative power inputs are $P_{\Delta p_{\mathrm{C},i}}(G = 0.0074) = 0.142\,\mathrm{bar} \cdot 1.73 \cdot 10^{-5}\,\mathrm{m^3\,s^{-1}} = 0.25\,\mathrm{W}$ and $P_{\Delta p_{\mathrm{C},i}}(G = 0.0154) = 0.085\,\mathrm{bar} \cdot 1.73 \cdot 10^{-5}\,\mathrm{m^3\,s^{-1}} = 0.15\,\mathrm{W}$. Exemplary results of the reactor gap-side pressure drop for the setup with $G = 0.0074$ in dependence of rotational Reynolds number, dimensionless throughput and material properties are displayed in Figure 3.5.

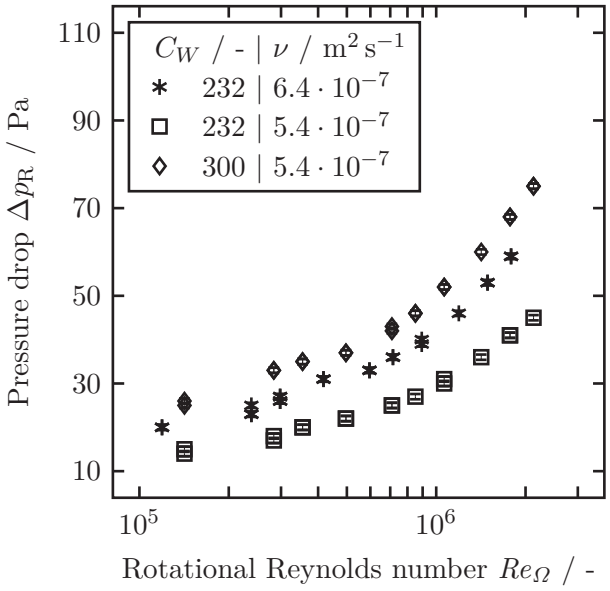

Figure 3.5: Pressure drop across the reactor gap in dependence of rotational Reynolds number, dimensionless throughput and viscosity ($G = 0.0074$).

As can be seen in Figure 3.5, pressure drop increases with increasing rotational Reynolds number. Two regimes are observed with regard to the rotational Reynolds number and are attributed to a laminar ($Re_\Omega \leq 6 \cdot 10^5$) and a turbulent ($Re_\Omega > 6 \cdot 10^5$) regime. Figure 3.5 further demonstrates an increase in pressure drop with a rise in dimensionless throughput as well as with a higher viscosity. Similar observations were made concerning experiments performed at the setup with $G = 0.0154$. However, the transition from laminar to turbulent flow occurs at smaller rotational Reynolds numbers ($Re_\Omega \approx 1{\cdot}10^5$), which is to be expected for setups with a higher aspect ratio considering the flow map of Daily and Nece [65]. In dependence of dimensionless throughput, rotational Reynolds number, aspect ratio and a viscosity term, adapted quantity equations for the laminar (Equation (3.14)) and turbulent (Equation (3.15)) regime were established in order to determine the pressure drop for the single heat transfer experiments. The parameters a_1 to a_5 in Equations (3.14) and (3.15) with the corresponding 95 % confidence intervals are given in Table 3.1. The corresponding parity plot is given in Figure 3.6.

$$\frac{\Delta p_R}{\text{bar}} = C_W^2 \, G^{a_1} \left(\frac{\nu}{\text{m}^2\,\text{s}^{-1}} \right)^{a_2} + C_W^2 \, Re_\Omega \left(\frac{\nu}{\text{m}^2\,\text{s}^{-1}} \right)^{a_3} \tag{3.14}$$

$$\frac{\Delta p_R}{\text{bar}} = a_4 \, C_W^2 \, G^{a_1} \left(\frac{\nu}{\text{m}^2\,\text{s}^{-1}} \right)^{a_2} + a_5 \, C_W^2 \, Re_\Omega \left(\frac{\nu}{\text{m}^2\,\text{s}^{-1}} \right)^{a_3} \tag{3.15}$$

Table 3.1: Parameter values and 95 % confidence intervals of the pressure drop correlations given in Equations (3.14) and (3.15).

Parameter	Value ± 95 % confidence interval
a_1	-2.411 ± 0.027
a_2	2.068 ± 0.037
a_3	2.332 ± 0.036
a_4	177.286 ± 91.448
a_5	$1.144 \cdot 10^3 \pm 583.132$

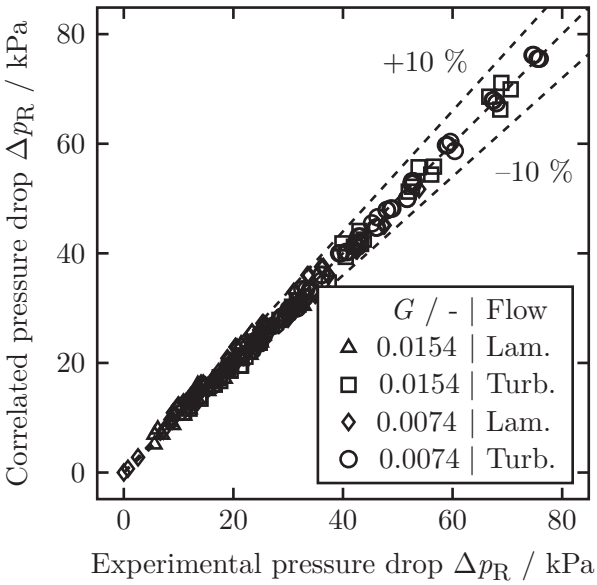

Figure 3.6: Parity plot of the pressure drop correlations for the two regarded setups.

The majority of the pressure measurements is described within 10 % accuracy with the above given adapted quantity equations. All parameters in Equations (3.14) and (3.15) are significant, as indicated by the confidence intervals. With regard to the dimensionless throughput, a quadratic dependence of the pressure drop was observed for both setups, whereas the dependence on rotational Reynolds number is linear. The results are qualitatively in accordance with literature [21, 57, 58]. The high value for the dependence on the aspect ratio observed within this work (compare $\Delta p \propto G^{-0.2}$ [21]) can be explained by taking into account that the change in aspect ratio is brought about by a variation of radius. Therefore, varying the aspect ratio by varying gap height and by varying radius is not comparable when regarding rotor-stator setups with an upper and a lower gap.

Rotational energy dissipation

Rotational energy dissipation was determined via the two methods presented in Equations (3.12) and (3.13). The latter method to determine dissipative power input gave

results, which differ about 15 % from the results gained via the first method and the overall measurement uncertainty of the second method is considered significantly higher. Moreover, the theoretically estimated power input for the setups via the correlation by Daily and Nece [65] predicts values, which are close to the measured power inputs of the first method. Therefore, the power input is determined via Equation (3.12) and a correlation in accordance to Daily and Nece [65] is established (Equation (3.16)) to predict the power input for the single heat transfer measurements. The respective parameters and 95 % confidence intervals of Equation (3.16) are given in Table 3.2. The corresponding parity plot of the dissipative power input due to rotation is given in Figure 3.7.

$$\frac{P_{\mathrm{rot}}}{\mathrm{W}} = b_1\, G^{b_2}\, Re_{\Omega}^{b_3}\, \frac{\varrho}{\mathrm{kg\,m^{-3}}}\, 0.5 \left(\frac{\Omega}{\mathrm{rad\,s^{-1}}}\right)^3 \left(\frac{r_{\mathrm{r,o}}}{\mathrm{m}}\right)^5 \tag{3.16}$$

Table 3.2: Parameter values and 95 % confidence intervals for the dissipative power input correlation in Equation (3.16).

Parameter	Value ± 95 % confidence interval
b_1	0.165 ± 0.040
b_2	0.119 ± 0.035
b_3	-0.203 ± 0.020

As shown in Figure 3.7, the dissipative power input measurements are described within 15 % accuracy by the correlation in Equation (3.16) at higher power inputs. Only at small dissipation rates deviation is higher, which is attributed to the higher measurement uncertainty at very small dissipative power inputs.

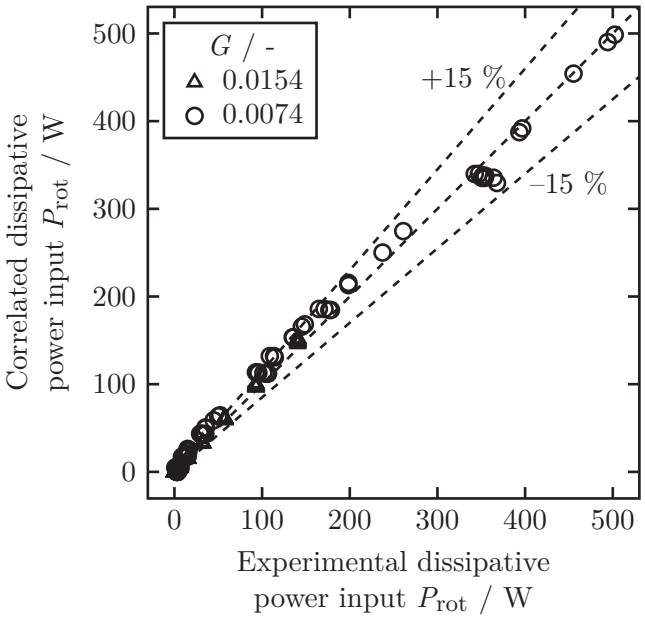

Figure 3.7: Parity plot of the correlation for the dissipative power input due to rotation for the two regarded setups.

3.6.2 Overall heat transfer coefficient

The overall heat transfer coefficients for the setup with $G = 0.0154$ deduced from the enthalpy balances for the reactor gap are shown in Figure 3.8. The influence of rotational Reynolds number, dimensionless throughput and glycerol mass fraction is visualized in Figure 3.8. An increase in overall stator-side heat transfer coefficient with increasing Reynolds number is observed, which is linear at small rotational Reynolds numbers and levels off to higher rotational Reynolds numbers until a limit of $U_s \approx 4100\,\mathrm{W\,m^{-2}\,K^{-1}}$ is reached. For rotational Reynolds numbers below 10^6, a dependence of the heat transfer coefficient on dimensionless throughput is observed, which reduces with increasing rotational speeds. With regard to the material properties varied via the glycerol mass fraction, the overall heat transfer coefficient increases with higher glycerol content, which is equal to a higher Prandtl number. At very high rotational Reynolds numbers, no influence of any parameter is observable anymore. This is due to the thermal resistance through conduction in the stator walls and convective heat transfer in the coolant channels limiting the overall heat transfer coefficient. The outer resistance is mainly ascribed to the convective heat transfer in the coolant channels. The reason for this is that the stator consists of an aluminum alloy with a heat transfer coefficient through the 3 mm stator wall between reactor gap and coolant channels of about $\lambda_{alu}\, s_s^{-1} = 37 \cdot 10^3\,\mathrm{W\,m^{-2}\,K^{-1}}$, which is one order of magnitude larger than the observed limit.

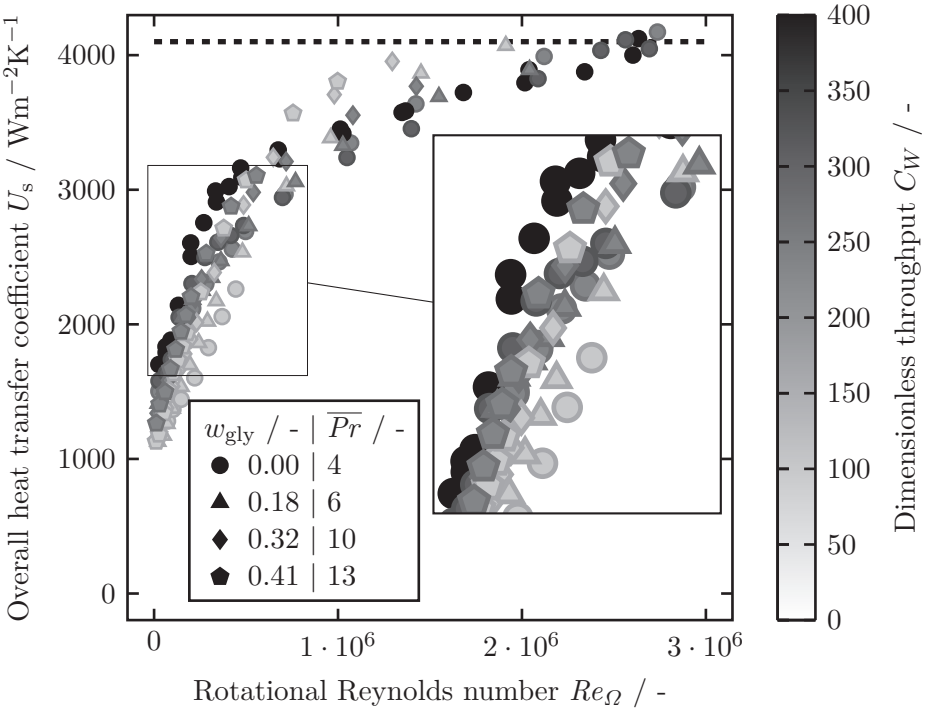

Figure 3.8: Overall heat transfer coefficient in dependence of rotational Reynolds number, dimensionless throughput and glycerol mass fraction ($G = 0.0154$).

3.6.3 Stator-side heat transfer coefficient

The outer limit of 4100 $\mathrm{W\,m^{-2}\,K^{-1}}$ is used for evaluation of the experiments at the setup with $G = 0.0074$, as the geometric properties of the two setups are almost the same. Furthermore, with the current peripheral heating and coolant circuits, the limit cannot be reached in the setup with $G = 0.0074$, which heat transfer area is four times higher than the one of the setup with $G = 0.0154$. Therefore, for the former setup, the heat transfer coefficient is directly fitted in the evaluation with MATLAB®. The results are given in Figure 3.9, showing stator-side heat transfer coefficients in dependence of rotational Reynolds number and dimensionless throughput for a glycerol mass fraction of $w_{\mathrm{gly}} = 0$. With regard to the rotational Reynolds number, the heat transfer coefficient increases slightly at lower rotational Reynolds numbers and decreases a little before rising more steeply at $Re_\Omega > 10^6$. The occurrence of this slight local extremum is attributed to flow irregularities at the flow transition from laminar to turbulent torsional-Couette regime, which was already observed within the pressure drop measurements (cf. Figure 3.5 in Section 3.6.1). Figure 3.9 further reveals an increase in heat transfer coefficient with increasing throughput, while the influence appears to be higher at smaller rotational Reynolds numbers in comparison to higher ones. This can be explained by the heat transfer in the regarded setup ($G = 0.0074$) being rotation governed at higher rotational Reynolds numbers, as already reported in literature for similar rotor-stator cavities [21].

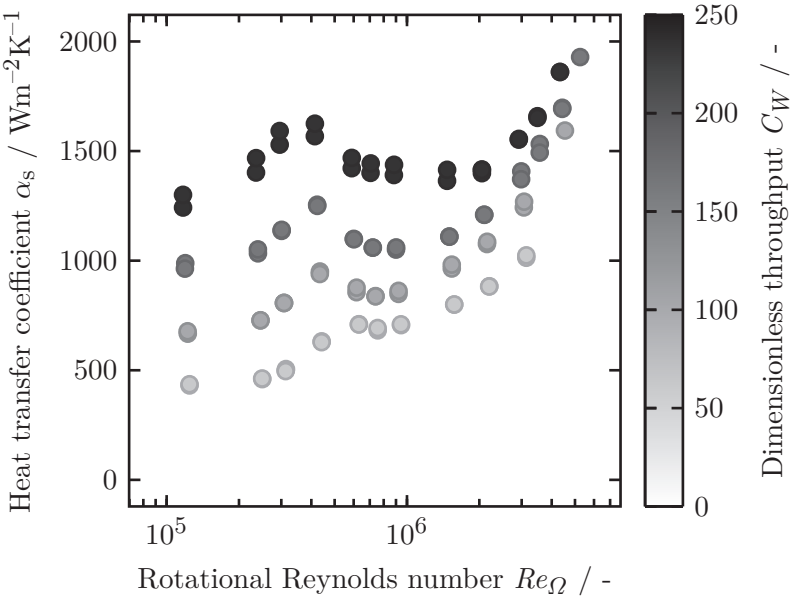

Figure 3.9: Stator-side heat transfer coefficient in dependence of rotational Reynolds number and dimensionless throughput for a glycerol mass fraction of $w_{\mathrm{gly}} = 0$, corresponding to $Pr \approx 4$ ($G = 0.0074$).

3.6.4 Stator-side Nusselt number

Based on the results of the overall heat transfer coefficient for $G = 0.0154$, values for the stator-side heat transfer coefficient were determined using Equation (3.1) with $U_{\mathrm{limit}} = 4100\,\mathrm{W\,m^{-2}\,K^{-1}}$. Only measurements with $Re_\Omega \leq 4.25 \cdot 10^5$ were used for evaluation of the heat transfer coefficients for the larger aspect ratio, in order to minimize errors due to effects of the outer limit by heat transfer through the stator and coolant channels. The stator-side Nusselt numbers were determined for both setups using Equation (2.9) in Section 2.1.3 and the stator-side heat transfer coefficient. The results for $G = 0.0154$ are given in Figure 3.10, which shows the dependence of the stator-side Nusselt number on rotational Reynolds number and Prandtl number (a) and dimensionless throughput (b). An increase in Nusselt number with increasing rotational Reynolds number is observed, while at rotational Reynolds numbers below 10^5 only a small dependence of the Nusselt number on the rotational Reynolds number is visible, which increases at higher rotational Reynolds numbers. The transition between the two regimes is in accordance with the regimes already observed during the pressure drop measurements (cf. Section 3.6.1) for $G = 0.0154$ and are attributed to the laminar and turbulent torsional-Couette regime proposed by Daily and Nece [65]. Figure 3.10a further reveals an increase in Nusselt number with increasing Prandtl number and Figure 3.10b shows a rising Nusselt number with increasing throughput for the laminar and the turbulent regime. This means that, although the influence of the rotational Reynolds number on the Nusselt number in the turbulent regime is expressed more strongly, a dependence on dimensionless throughput is still observable for $G = 0.0154$.

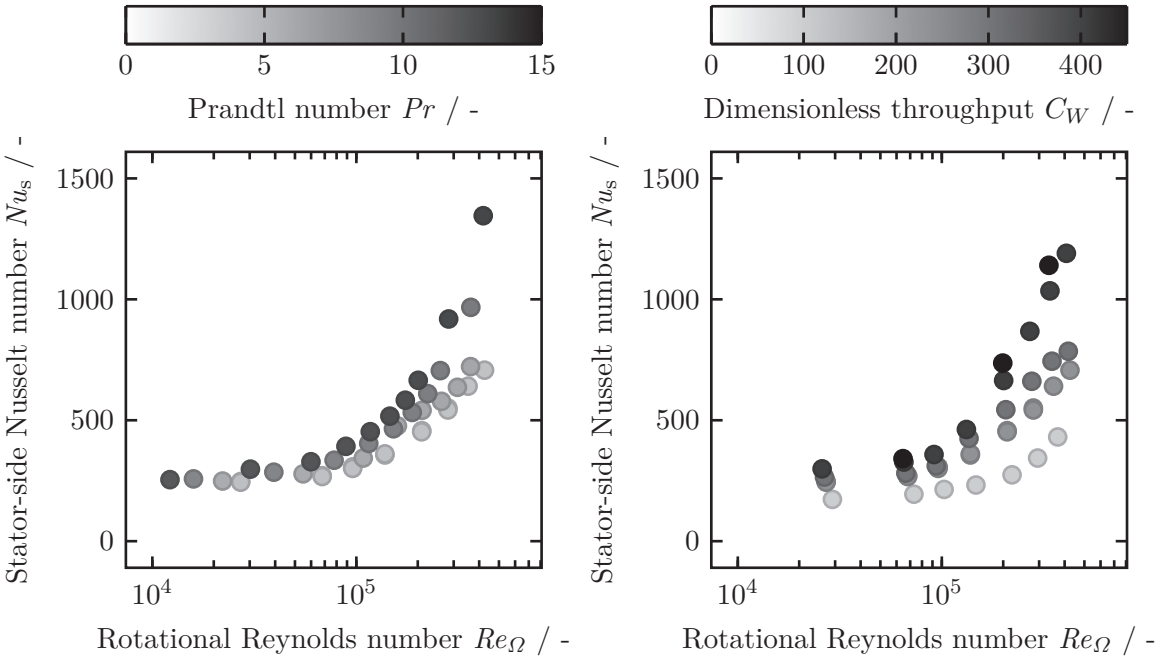

(a) $C_W = 232$.

(b) $w_{\mathrm{gly}} = 0$.

Figure 3.10: Stator-side Nusselt number in dependence of rotational Reynolds number and Prandtl number (a) and dimensionless throughput (b) ($G = 0.0154$).

In comparison to the results in Figure 3.10 for $G = 0.0154$, Figure 3.11 analogously presents the stator-side Nusselt number in dependence of rotational Reynolds and Prandtl number (a) and dimensionless throughput (b) for $G = 0.0074$. According to Figure 3.11, two different flow regimes are also present for the larger setup ($G = 0.0074$), but the transition is at higher rotational Reynolds numbers (cf. Section 3.6.1). The stator-side Nusselt number for this setup increases with increasing Prandtl number and the dependence of the Nusselt number on the Prandtl number is stronger for the setup with larger radius ($G = 0.0074$) (cf. Figure 3.11a). Within the regarded parameter range, the Nusselt number increases considerably with a higher throughput for rotational Reynolds numbers below $1 \cdot 10^6$. However, this dependence decreases with a further increase in rotational Reynolds number and almost ceases at $Re_\Omega = 5 \cdot 10^6$ (cf. Figure 3.11b). Comparing Figures 3.10 and 3.11, it can be seen that the Nusselt numbers for $G = 0.0154$ are higher in comparison to the ones measured with the setup with the smaller aspect ratio. It further stands out that for $G = 0.0154$, the dependence on the Prandtl number is smaller compared to $G = 0.0074$ and that for the latter setup a decreased dependence of the Nusselt number on dimensionless throughput is observed. Regarding this, it is, however, noteworthy that with the smaller setup ($G = 0.0154$) remarkably higher dimensionless throughputs (almost a factor two) could be reached using the current setups.

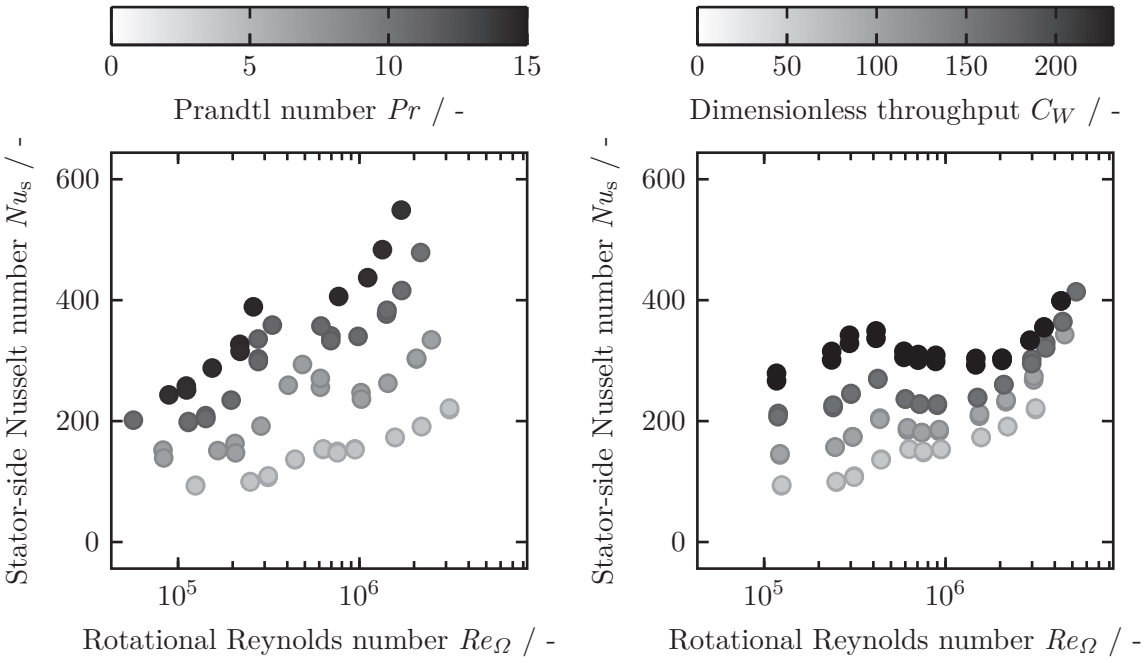

(a) $C_W = 60$. **(b)** $w_{\text{gly}} = 0$.

Figure 3.11: Stator-side Nusselt number in dependence of rotational Reynolds number and Prandtl number (a) and dimensionless throughput (b) ($G = 0.0074$).

A dimensionless Nusselt correlation to predict the experimental data within the turbulent regime for both setups was established. Therefore, only data points, which clearly are in the turbulent regime were used meaning for $G = 0.0154 : 10^5 \leq Re_\Omega$ and for

$G = 0.0074 : 1.7 \cdot 10^6 \leq Re_\Omega$. The resulting correlation is given in Equation (3.17) and the respective parameters with the corresponding 95 % confidence intervals are given in Table 3.3.

$$Nu_\mathrm{s} = (Re_\Omega^{0.8}\, C_W^{c_1 G}\, G^{c_2} + G\, C_W^{c_1 G})\, Pr^{c_3/G} \tag{3.17}$$

Table 3.3: Parameter values and 95 % confidence intervals for the Nusselt correlation in Equation (3.17).

Parameter	Value ± 95 % confidence interval
c_1	40.993 ± 2.483
c_2	1.878 ± 0.090
c_3	0.008 ± 0.001

A similar approach to the pressure drop correlations in Equations (3.14) and (3.15) was used, but as already seen in Figures 3.10 and 3.11, the dependences on dimensionless throughput and Prandtl number for the two different aspect ratios differ. The dependence of the Nusselt number on rotational Reynolds number was set to 0.8, as is reported in literature for the turbulent regime of rotor-stator reactors [41, 73, 77, 80, 81, 94, 98, 99, 104]. The parity plot of the Nusselt number correlation for both setups is given in Figure 3.12. A good agreement within ±20 % accuracy is found between experimental and correlated data, which is about the maximum measurement uncertainty for the regarded experiments. The data points in Figure 3.12 are regularly distributed around the bisecting line and no distinct systematic deviation is observed.

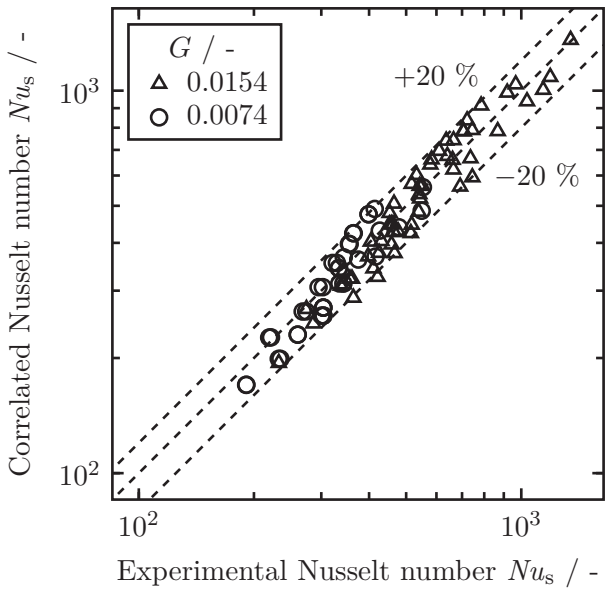

Figure 3.12: Parity plot of the Nusselt correlation for the two regarded setups; only data points within the turbulent torsional-Couette regime were used for the fit of the Nusselt correlation, i.e., for $G = 0.0154 : 10^5 \leq Re_\Omega$ and for $G = 0.0074 : 1.7 \cdot 10^6 \leq Re_\Omega$.

For both regarded setups, an increase in Nusselt number with increasing dimensionless throughput was observed for the laminar and turbulent regime. A higher throughput reduces the thickness of the thermal boundary layers at the stator and rotor side and thereby decreases the thermal resistance in the boundary layers leading to a higher heat transfer coefficient. As in the turbulent regime the influence of the rotational Reynolds number is larger compared to the influence of dimensionless throughput, the turbulent regime is considered to be governed by rotation of the rotor. The observation of the dimensionless throughput having an influence on the Nusselt number in the rotation-governed regime is in accordance with literature results [58, 67, 99]. The smaller dependence on dimensionless throughput for the setup with $G = 0.0074$ compared to the setup with the smaller radius ($G = 0.0154$) might be explained considering that the turbulent regime is shifted towards higher rotational Reynolds numbers for $G = 0.0074$. Therefore, it might be that for the latter setup the influence of the dimensionless throughput is smaller because the effect of rotational Reynolds number overweighs the throughput influence more strongly at rotational Reynolds numbers $10^6 \leq Re_\Omega$. Also, at higher rotational Reynolds numbers, a larger part of the gap behaves as a continuous stirred tank reactor (CSTR), which could further explain the lower dependence of the Nusselt number on dimensionless throughput for the setup with $G = 0.0074$.

The experiments show different dependences of the Nusselt number on the Prandtl number for the two regarded setups. For the smaller setup ($G = 0.0154$), the power of the Prandtl number is 0.52. This is in accordance with literature results for similar rotor-stator setups. Poncet et al. [73] for example found a dependence of $Nu \propto Pr^{0.5}$ for $0.036 \leq G \leq 4/9$, $5 \cdot 10^5 \leq Re_\Omega \leq 1.44 \cdot 10^6$, $0 \leq C_W \leq 12082$ and $1 \leq Pr \leq 12$. Owen [98] found a dependence of the Nusselt number on the Prandtl number with a power of 0.6 for $0.03 \leq G \leq 0.12$, $5 \cdot 10^5 \leq Re_\Omega \leq 4 \cdot 10^6$, $25000 \leq C_W \leq 100000$ and $0.6 \leq Pr \leq 1$. The observation of the Nusselt number for the setup with the larger radius ($G = 0.0074$) having a higher dependence on the Prandtl number might be explained considering that rotating systems show higher dependences on the Prandtl number compared to tubes or plates, etc., which often have Nusselt numbers correlating with $Pr^{0.33}$. As several researchers report dependences of the Nusselt number on the Prandtl number such as $Pr^{0.5}$ or $Pr^{0.6}$ [73–75, 77, 78, 98] for rotating systems, it is not astonishing to observe that the higher the radius of the regarded rotating system, the higher the power for the Prandtl dependence. The strongest influence on the Prandtl number is assumed to be due to the viscosity, which could support the afore chain of thought, as the positive effect of the rotor-stator reactor on media with high viscosities is supposed to be higher with larger radii, as the local energy is higher.

An increase in Nusselt number with a higher aspect ratio, as observed in this study, does agree with literature results to some extent. De Beer et al. [21] regarded two different setups ($G = 0.03$ and $G = 0.017$) and found that for $Re_\Omega \leq 0.2 \cdot 10^5$ $Nu_\mathrm{s} \propto G^{-1}$. However, they varied the aspect ratio by changing the gap height instead of the radius.

Kapinos [99] found $Nu_s \propto G^{-0.09}$ for a regarded parameter range of $0.016 \leq G \leq 0.06$, $5 \cdot 10^5 \leq Re_\Omega \leq 4 \cdot 10^6$, but did not state, how he varied the gap ratio. Owen et al. [74] found a decreasing trend of the average Nusselt number with increasing aspect ratio up to $G = 0.01$, after which the Nusselt number increases with further rising aspect ratio until an asymptote of the Nusselt number is reached at $G > 0.06$ for $4.8 \cdot 10^5 \leq Re_\Omega \leq 3.9 \cdot 10^6$. Boutarfa and Harmand [75] found different dependences of the average Nusselt number on the aspect ratio. For turbulent flow and a range of $0.02 \leq G \leq 0.06$ they found $Nu \propto \exp(-9.27\,G)\, Re_\Omega^{3/5+25\,G^{12/7}}$; for lower aspect ratios of $G = 0.01$, they did not correlate the Nusselt number with the aspect ratio and for $G > 0.06$, they established $Nu \propto \exp(-9.27\,G)\, Re_\Omega^{0.8}$. Pellé and Harmand [79] proposed correlations for three different regimes and found the average Nusselt number to decrease with increasing aspect ratio for small aspect ratios. The research of Owen, Boutarfa and Harmand and Pellé and Harmand was conducted varying the aspect ratio by changing the gap distance and not the radius. Therefore, it is considered difficult to compare the findings of this study with literature results in terms of the aspect ratio influence, as a variation of the gap ratio by changing the radius is very different from varying the actual gap height. Most importantly the heat transfer areas for the two setups in this study are different, which makes it already difficult to quantitatively compare the Nusselt numbers for the two setups regardless of the transfer area studied in this work. Since the Nusselt number is proportional to radius and the heat transfer area correlates with the radius to a power of two, any comparison of rotor-stator systems, which do not have the same heat transfer area, should be done very carefully and only qualitatively.

A qualitative comparison is given in Figure 3.13, showing stator- and rotor-side Nusselt numbers based on correlations and data points found in literature for the turbulent regime. The literature data is compared to the correlation established in this study for the setup with $G = 0.0154$ for a dimensionless throughput of $C_W = 300$ and a Prandtl number of $Pr \approx 4$. The data of the current setup lies within most of the correlations found in literature.

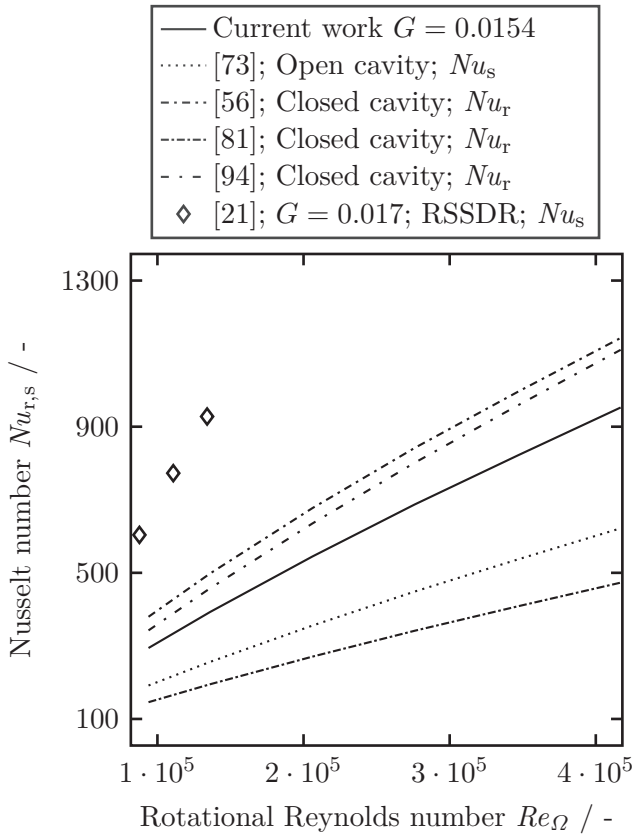

Figure 3.13: Comparison of the current work with literature results. For an open cavity, a Nusselt correlation for the stator is given for the turbulent regime [73]. Rotor-side Nusselt number correlations for a closed cavity within the turbulent regime by Nikitenko [81], Shchukin [94], and Owen [56] are indicated, as well as data for the stator-side Nusselt number in an RSSDR by de Beer et al. [21]. The Nusselt numbers are given for a dimensionless throughput of $C_W = 300$ and a Prandtl number of $Pr \approx 4$. The literature data is corrected by $(Pr_{\text{water}}/Pr_{\text{air}})^{0.52}$, if applicable [21].

Regarding the overall volumetric heat transfer coefficient $U_s A V^{-1}$ of the studied reactor, an increase from $1.27\,\text{MW}\,\text{m}^{-3}\,\text{K}^{-1}$ to $2.16\,\text{MW}\,\text{m}^{-3}\,\text{K}^{-1}$ for an increase in rotational Reynolds number from $2.71 \cdot 10^4$ to $4.25 \cdot 10^5$, a throughput of $C_W = 232$, a Prandtl number of 4 and an aspect ratio of $G = 0.0154$ was observed. The dissipative power input at $Re_\Omega = 4.25 \cdot 10^5$, $C_W = 232$ and $G = 0.0154$ is quite low (1.03 W), while pressure drop values 0.052 bar. This value of the overall volumetric heat transfer coefficient is more than a factor two higher compared to overall volumetric heat transfer coefficients by de Beer et al. [21], who measured $U_s A V^{-1} = 0.93\,\text{MW}\,\text{m}^{-3}\,\text{K}^{-1}$ ($Re_\Omega = 4.5 \cdot 10^5$, power input of 10 W), which is already more than a factor five larger in comparison to conventional tube reactors [105]. It should, however, be noted that this higher value is attributed to the higher limit through the stator walls and coolant channels, showing that further alterations of the setup could lead to even higher overall volumetric heat transfer coefficients. At a similar rotational Reynolds number of $Re_\Omega = 4.13 \cdot 10^5$ and the same dimensionless throughput, with the setup having an aspect ratio of $G = 0.0074$, $U_s A V^{-1} = 1.04\,\text{MW}\,\text{m}^{-3}\,\text{K}^{-1}$ at a pressure drop of 0.069 bar and a dissipative power

input of 0.47 W was reached, which is still high, but only half the value of the setup with $G = 0.0154$ of this study. The maximum stator-side Nusselt number observed for the small setup ($G = 0.0154$) was 1346 at $Re_\Omega = 4.2 \cdot 10^5$, a dimensionless throughput of 232 and a Prandtl number of 13 (pressure drop $\Delta p_\mathrm{R} = 0.052\,\mathrm{bar}$ and rotational power input $P_\mathrm{rot} = 15.5\,\mathrm{W}$). The results of this work show an intensification of the heat transfer in an RSSDR by variation of several parameters, thus, making this type of reactor attractive for strongly exo- or endothermic reactions, as already reported by de Beer et al. [21].

3.7 Conclusion

The single-phase stator-side heat transfer in an RSSDR was studied in dependence of rotational Reynolds number, dimensionless throughput, Prandtl number and aspect ratio. An increase in stator-side Nusselt number with higher Prandtl and rotational Reynolds numbers and higher dimensionless throughputs was observed for both regarded setups, while the Nusselt numbers for the setup with the aspect ratio of $G = 0.0154$ are higher compared to the setup with $G = 0.0074$, which can be explained by the respective heat transfer area. Laminar and turbulent flow regimes with regard to the rotational Reynolds number were found for both setups, with the critical rotational Reynolds numbers being $Re_{\Omega,\mathrm{crit}}(G = 0.0154) \approx 10^5$ and $Re_{\Omega,\mathrm{crit}}(G = 0.0074) \approx 10^6$. In the laminar regime, heat transfer is governed by the superimposed throughput, whereas in the turbulent flow region, rotation prevails the heat transfer. A Nusselt number correlation for the turbulent flow region was established, with the power of the rotational Reynolds number being 0.8 as reported in literature [41, 73, 77, 80, 81, 94, 98, 99, 104], to predict the experimental data within 20 % accuracy. Different dependences of the stator-side Nusselt numbers on Prandtl number and dimensionless throughput were observed for the two aspect ratios in the respective turbulent regime. The variation of the aspect ratio was ensured by a variation in the radius and not the gap height, as it is often found in literature. Since a difference in the Nusselt number's dependence on dimensionless throughput and especially on Prandtl number for the different aspect ratios, as is observed in this study, is not seen in literature, it can, thus, be concluded that it is crucial, how the variation of the aspect ratio is achieved.

A maximum stator-side Nusselt number of 1346 for the setup with $G = 0.0154$ was measured for $Pr = 13, C_W = 232$ and $Re_\Omega = 4.2 \cdot 10^5$ at a dissipative power input of $P_\mathrm{rot} = 15.5\,\mathrm{W}$. An intensification of the overall volumetric heat transfer coefficient from $1.27\,\mathrm{MW\,m^{-3}\,K^{-1}}$ to $2.16\,\mathrm{MW\,m^{-3}\,K^{-1}}$ for an increase in rotational Reynolds number from $Re_\Omega = 2.71 \cdot 10^4$ to $Re_\Omega = 4.25 \cdot 10^5$ at low energetic costs was reached, which is considerably higher in comparison to conventional tube reactors [105] and more than twice as high compared to a similar rotor-stator setup [21].

4 CFD simulation of single-phase heat transfer in a rotor-stator spinning disc reactor

This chapter was published in a similar way as:

J. Kleiner, B. Münch, F. Rößler, J. Fernengel, F. Habla, O. Hinrichsen, CFD simulation of single-phase heat transfer in a rotor-stator spinning disc reactor. *Chem. Eng. Process.* 131 (2018) 150−160 [106].
Reprint with permission from *Elsevier*.

4.1 Abstract

A computational fluid dynamics (CFD) study on hydrodynamics and heat transfer in a rotor-stator spinning disc reactor (RSSDR), an inventive reactor technology engineered within the frame of process intensification (PI), was performed with OpenFOAM®. This allows the investigation of locally resolved temperature profiles and heat transfer coefficients in the reactor gap, which is experimentally difficult for RSSDRs with small dimensions, while keeping computational costs low. The retrieved radial and tangential velocity and temperature profiles are in agreement with literature. Local stator-side heat transfer coefficients were determined, which increase with higher disc speeds and with increasing throughputs. Area-averaged heat transfer coefficients across the reactor gap were calculated and validated against experimental results performed on the setup simulated in this study; the numerical and experimental data are in qualitative agreement. This study presents the possibility to characterize an RSSDR in terms of hydrodynamics and heat transfer properties by means of a two-dimensional axisymmetric (2.5D) geometry and Reynolds-averaged Navier−Stokes (RANS) turbulence modeling in OpenFOAM®. Expensive measurements, which are difficult to perform particularly for RSSDRs with small dimensions, could thus be avoided, simulating industrial applications at the conditions of interest and designing the RSSDR setup accordingly.

4.2 Introduction

The investigation of hydrodynamics and heat transfer in rotor-stator cavities has been the focus of many studies for the past decades, as this topic is important in several engineering disciplines; especially in the field of turbomachinery, many researches have been conducted [80]. However, there are few studies on fluid flow in rotor-stator reactor setups with smaller dimensions and even fewer regarding heat transfer problems. As experimental work, especially investigations on heat transfer, on rotor-stator reactor systems with small dimensions are difficult to perform, a theoretical approach to simulate hydrodynamics and conjugate heat transfer in an RSSDR is presented in this chapter. The RSSDR is an inventive reactor technology, which was engineered within the scope of PI as an advancement of the spinning disc reactor (SDR) [28]. The term PI is understood as "any chemical engineering development that leads to a substantially smaller, cleaner, and more energy-efficient technology" [17]. The RSSDR, among other, addresses intensification of heat and mass transfer limited reactions and has been the object of several studies in the past years, as it is crucial to fully characterize a reactor type for the quantification of a reactor setup's performance and to plan the setup accordingly [21, 31, 91].

Most of the studies on rotor-stator systems found in literature concentrate on enclosed rotating discs or open cavities with either centripetal or centrifugal throughput. Daily and Nece [65] were among the first to experimentally and theoretically investigate fluid dynamics of enclosed rotating discs for a wide range of parameters. Research on a closed rotor-stator system was also performed by Schouveiler et al. [107] who examined flow instabilities in between a rotating and a stationary disc. With the same setup of Schouveiler et al.'s work, Cros et al. [108] studied the laminar-turbulent transition of torsional-Couette flow. Experiments on turbulent Batchelor type flow in an enclosed rotating disc were performed by Itoh et al. [109] who measured mean velocity distributions and the Reynolds stress tensor components in the two boundary layers formed at the rotor and stator side. Lopez et al. [68] performed a numerical study on instability of the cross flow in the Bödewadt layer of an enclosed rotating cylinder system. The applicability of different turbulence models in the modeling of rotating confined flows was investigated by Elena and Schiestel [110], who regarded a closed rotor-stator system with an aspect ratio $G = 0.08$. Debuchy et al. [111] performed experiments on an enclosed rotor-stator system for different aspect ratios ($0.05 \leq G \leq 0.10$) and rotational Reynolds numbers ($1.14 \leq 10^{-6} Re_{\Omega} \leq 1.96$) and developed an analytical model of the central core flow. Van Eeten et al. [112] used a numerical model as well as an analytical series approximation to describe the boundary layer development of the flow in between two infinite discs, of which one is stationary and one is rotating.

Phadke et al. [60] studied shrouded rotor-stator systems for different shroud geometries and investigated the effect of superimposed airflow rates and rotational disc speeds on the

sealing of gas-turbines. Iacovides et al. [71] investigated problems in turbulence modeling of numerical studies on fluid flow in co-rotating disc systems with radial throughflow and enclosed disc flow with aspect ratios of $G = 0.1333, 0.0685$ and 0.0255 with a $k{-}\varepsilon$ turbulence model in combination with an algebraic stress model. An experimental and a theoretical study on turbulent flow in a rotor-stator cavity with and without superimposed throughput was performed by Poncet et al. [59] who concentrated on the transition from Batchelor to Stewartson flow types. Poncet et al. [57] further did an experimental study on the entrainment coefficient in dependence of different aspect ratios, centripetal throughputs and rotational disc speeds of fluid rotating in a rotor-stator system and observed flow profiles in the Batchelor regime. A numerical study on turbulent torsional-Couette flow for a wide parameter range with rotational Reynolds numbers of $1.8 \cdot 10^5 \leq Re_\Omega \leq 1 \cdot 10^7$, aspect ratios of $0.02 \leq G \leq 0.05$ and dimensionless throughputs $-1 \cdot 10^4 \leq C_W \leq 1 \cdot 10^4$ was done by Haddadi et al. [64].

Studies on heat transfer and temperature distribution in dependence of rotation and coolant flow in a heated shrouded parallel disc system were conducted by Sparrow and Goldstein [113] for aspect ratios of $G = 4/9, 8/9$ and 2, different coolant flow rates and rotational Reynolds numbers between 0 and 10^6. A theoretical study on fluid flow and heat transfer in both an enclosed and an open rotor-stator system was conducted by Beretta and Malfa [114], who used CFD simulations in order to investigate momentum coefficients, mechanical power dissipation as well as velocity and temperature fields; they validated their CFD simulation results against a semi-empirical model, which they developed based on mass and momentum balances as well as the Reynolds analogy. The heat transfer with radial inward airflow in a rotor-stator system was experimentally and theoretically examined by Djaoui et al. [67] who extended the work of Debuchy et al. [111] on fluid flow in rotor-stator systems to heat transfer effects for aspect ratios $G < 1$. Poncet et al. [73] studied the setups of the work of Djaoui et al. [67] and Sparrow et al. [113] in their numerical work on heat transfer and flow properties in rotor-stator cavities with superimposed throughput; they used a Reynolds stress model (RSM) to predict the experimental data of the aforementioned studies and thereby validate the proposed model. Iacovides and Chew [104] did a computational study of convective heat transfer in rotating cavities with a RANS approach; they tested different turbulence models and regarded three different cavity configurations. A numerical study on turbulent flow and convective heat transfer in a rotating cavity with an aspect ratio of $G = 0.1333$ with a standard $k{-}\varepsilon$ and an algebraic stress model approach was further performed by Schiestel et al. [115].

Investigations on hydrodynamics and heat transfer in single- or multi-stage RSSDRs, as studied in this work, have mostly been experimental so far. Residence time distributions were determined by Visscher et al. [40], de Beer et al. [31] and Haseidl et al. [42]. The single-phase stator-side heat transfer in an RSSDR was investigated by de Beer et al. [21] and Kleiner et al. [91] (cf. Chapter 3) and the fluid-rotor heat transfer by de Beer et

al. [29]. These studies on RSSDRs, however, did not allow to locally resolve velocity and temperature profiles and the experiments were complex and expensive. Hence, numerical investigations of actual rotor-stator reactors need yet to be performed [116]. This study, therefore, aims at the description of fluid flow, local temperature profiles and heat transfer coefficients in an RSSDR with the aid of CFD simulations using the open-source software OpenFOAM®. A simple 2.5D approach is pursued with RANS turbulence modeling in order to reduce computational costs. A two-equation model is used instead of an RSM to further keep computation times low, as the applicability of different two-equation turbulence models implemented in OpenFOAM® was investigated in a preparatory work, which showed positive results (cf. Appendix A.2.1).

4.3 Modeling

4.3.1 Setup

The reactor setup considered in this study is illustrated in Figure 4.1. The geometry is a 2.5D simplification of a three-dimensional reactor setup used to perform experiments on heat transfer in rotor-stator reactors [91]. The setup in Figure 4.1 consists of a rotor enclosed in a cylindrical housing, the stator, including coolant media channels in the upper and lower part. The respective geometric lengths are given in Figure 4.1. The tubular inlet of the reactor gap is eccentrically aligned at one position in the three-dimensional setup [91]. For the simplified 2.5D model it is assumed as a ring inlet at the same radial position as in the three-dimensional setup. A further simplification is to regard the coolant channels as radial gaps, although in the experimental setup they meander in 5 mm times 5 mm channels through the upper and lower stator part [91]. The volumetric throughput through the coolant channels was therefore adjusted to have the same average Reynolds number as in the channels with the quadratic cross section of the experimental setup in order to obtain similar heat transfer coefficients in the coolant channels [91]. The medium through the reactor gap is introduced via the ring inlet of the setup and leaves the reactor at the bottom center. Hence, the throughput is centrifugal in the upper gap and centripetal in the lower one. The upper and lower coolant media flow in a radially counter-current mode to the reactor gap medium, respectively (cf. Figure 4.1).

With the current configuration, the aspect ratio (Equation (2.2) in Section 2.1.2) values $G = 0.0154$. The varied parameters are the rotational disc speed n and, thus, the rotational Reynolds number Re_Ω (Equation (2.1)) and the volumetric dimensionless throughput C_W (Equation (2.3)), respectively.

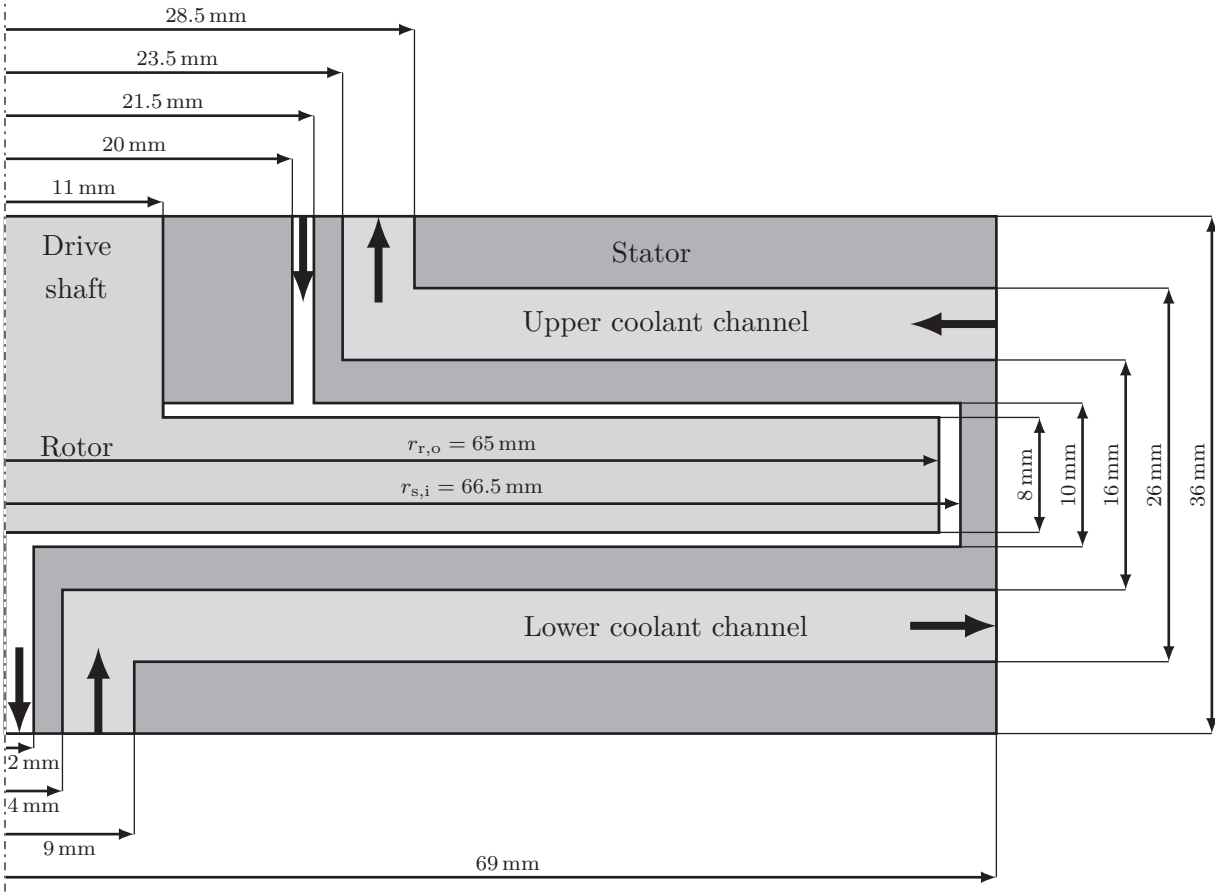

Figure 4.1: Geometric configuration of the studied reactor setup.

4.3.2 Mathematical formulation

In order to simulate fluid flow and heat transfer with the finite-volume approach, the governing mass, momentum and energy balances for the fluid regions need to be solved. The material properties of the fluids in this study are assumed constant in a first approach to facilitate simulations, hence, the equations are formulated in their incompressible version. Equation (4.1) gives the incompressible continuity equation and Equation (4.2) the incompressible momentum balance for steady-state. As a RANS approach is used, the temporal average of the quantities velocity $\mathbf{u}$ and pressure p is used in Equations (4.1) to (4.3). The temporal fluctuation of the velocity due to turbulence is considered in the Reynolds stress tensor $\boldsymbol{\tau}_{i,j}$.

$$\nabla \cdot \mathbf{u} = 0 \tag{4.1}$$

$$\nabla \cdot (\mathbf{u}\mathbf{u}) = -\frac{1}{\varrho}\nabla p + \nu \nabla^2 \mathbf{u} - \nabla \cdot \boldsymbol{\tau}_{i,j} \tag{4.2}$$

For simulation of the heat transfer, the enthalpy equation of the fluid domains is adjusted by a source term considering dissipative power inputs [117]. Enthalpy inputs due to radiation and buoyancy, however, have been omitted from the enthalpy equation as they are considered negligible in this study due to low temperatures and small temperature differences.

$$\nabla \cdot (\mathbf{u}\, h) + \nabla \cdot \left(\mathbf{u}\, \frac{|\mathbf{u}|^2}{2} \right) - \nabla \cdot (a_{\mathrm{eff,liq}}\, \nabla h) = \left[-\boldsymbol{\tau}_{i,j} + \nu \left(\nabla \mathbf{u} + \nabla \mathbf{u}^{\mathrm{T}} \right) \right] : \nabla \mathbf{u} \tag{4.3}$$

The parameters in Equation (4.3) are the specific enthalpy h, which also represents a temporal average, and effective thermal diffusivity a_{eff}, where the subscript "liq" stands for liquid.

The velocity fields of the reactor gap and coolant media were solved via the semi-implicit method for pressure-linked equations (SIMPLE) algorithm using the *simpleFoam* solver from OpenFOAM®. The *simpleFoam* solver is a standard solver from OpenFoam® and is used for steady-state simulations of incompressible flow with turbulence modeling [118]. Preparatory work on rotor-stator cavities, in which the applicability of different RANS turbulence models was investigated, revealed the *Lien-Leschziner* model [119, 120] to be well suited for 2.5D flow simulations of rotor-stator cavities with superimposed throughput (for further information cf. Appendix A.2.1). Therefore, the *Lien-Leschziner* turbulence model was used in this study for flow simulations of the reactor gap.

The *Lien-Leschziner* model as a two-equation or eddy-viscosity model is based on the Boussinesq eddy-viscosity approximation, which states an analogy between the mean viscous stress, which is proportional to the mean strain rate tensor, and the Reynolds stress [121], which is why according to the Boussinesq approach the Reynolds stress tensor is approximated as [122]:

$$-\boldsymbol{\tau}_{i,j} = \nu_{\mathrm{t}} \left(\nabla \mathbf{u} + \nabla \mathbf{u}^{\mathrm{T}} \right) - \frac{2}{3} \delta_{i,j}\, k\,, \tag{4.4}$$

with the eddy viscosity ν_{t}, the Kronecker delta $\delta_{i,j}$ and the turbulent kinetic energy k. The second term on the right-hand side in Equation (4.4) is needed to guarantee that the equation stays correct, when both sides of Equation (4.4) are contracted [122]. With this approach, the complexity of the turbulence closure problem is significantly decreased, as instead of the six components of the Reynolds stress tensor, only two unknown variables k and ν_{t} remain to be determined [121]. To finally solve the closure problem, these variables must be determined via models based on the known mean flow quantities [121], for which one approach is the usage of two-equation models as the *Lien-Leschziner* model, the model equations of which will be given in the following.

The eddy viscosity is usually given as [120]

$$\nu_\mathrm{t} = \tilde{C}_\mu \frac{k^2}{\varepsilon} \tag{4.5}$$

and the two steady-state transport equations for the turbulent kinetic energy k and the turbulent dissipation ε are given in Equations (4.6) and (4.7) [120].

$$\nabla \cdot (\mathbf{u}\, k) = \nabla \cdot [(\nu + \nu_\mathrm{t})\, \nabla\, k] + P_k - \varepsilon \tag{4.6}$$

$$\nabla \cdot (\mathbf{u}\, \varepsilon) = \nabla \cdot \left[\left(\nu + \frac{\nu_\mathrm{t}}{1.3}\right) \nabla\, \varepsilon\right] + \frac{\varepsilon}{k} \left(\tilde{C}_{\varepsilon 1}\, P_k - \tilde{C}_{\varepsilon 2}\, \varepsilon\right) \tag{4.7}$$

In the above given equations, P_k is the turbulence energy production. The tilded coefficients in Equations (4.5) to (4.7) are the numerical constants of the *Jones-Launder* model, if the flow is fully developed and high Reynolds turbulence applies [120]; however, under low Reynolds conditions, the coefficients depend on the Reynolds number Re_t (Equation (4.8)) and the dimensionless normal distance from the wall l_n^* (Equation (4.9)) and are given in Equations (4.10), (4.11) and (4.12) [120].

$$Re_\mathrm{t} = \frac{k^2}{\nu\, \varepsilon} \tag{4.8}$$

$$l_\mathrm{n}^* = \frac{l_\mathrm{n}\, k^{0.5}}{\nu} \tag{4.9}$$

$$\tilde{C}_\mu = 0.09 \left[\frac{1 - \exp\left(-0.016\, l_\mathrm{n}^*\right)}{1 - \exp(-0.263\, l_\mathrm{n}^*)}\right] \tag{4.10}$$

$$\tilde{C}_{\varepsilon 1} = 1.44 \left(1 + \frac{P_k'}{P_k}\right) \tag{4.11}$$

$$\tilde{C}_{\varepsilon 2} = 1.92 \left[1 - 0.3 \exp\left(-Re_\mathrm{t}^2\right)\right] \tag{4.12}$$

The parameter P_k' in Equation (4.11) is defined as follows [120]:

$$P_k' = \frac{\tilde{C}_{\varepsilon 2}\, k^{3/2}}{3.53\, l_\mathrm{n}\, \left[1 - \exp\left(-0.263\, l_\mathrm{n}^*\right)\right]} \exp\left[-0.00222\, l_\mathrm{n}^{*2}\right] \tag{4.13}$$

with the normal distance from the wall l_n [122].

The flow in the coolant channels was simulated using the k–ω-*SST* turbulence model. The concept for this eddy-viscosity model is analogous to the just described *Lien-Leschziner* model, only that the second model transport equation is for the specific rate of dissipation ω. As the simulation of the flow in the coolant channels was secondary, the k–ω-*SST* model is not presented at this point and the reader is referred to Menter et al. [123] for further information.

The cold-flow simulations of the reactor gap and coolant channels were then used to simulate heat transfer of the studied setup with the aid of the modified *chtMultiRegionSimpleFoam* solver. For the solid regions, the enthalpy balance given by Equation (4.14) was solved in the conjugate heat transfer simulations. The subscript "sol" in Equation (4.14) stands for solid.

$$\nabla \cdot (a_{\mathrm{eff,sol}} \nabla h) = 0 \tag{4.14}$$

4.3.3 Numerical approach and mesh

A finite volume approach was used for computations on the 2.5D meshes. The used meshes consist of fully structured blocks with hexahedral cells created using the *blockMesh* utility from OpenFOAM®. A grading is employed on each block in order to refine the mesh towards walls and critical mesh areas. The number of cells, resulting from a mesh convergence study (cf. Appendix A.2.3), for the meshes of the different domains are given in Table 4.1. Wedge segments of 5° of the axisymmetric domains were meshed. A detailed view of the reactor gap domain is shown in Figure 4.2.

Table 4.1: Mesh sizes of different setup domains. Every domain is a 5° segment of an axisymmetric element.

Domain	Number of cells
Reactor gap	$3.082 \cdot 10^5$
Upper coolant channel	$1.513 \cdot 10^5$
Lower coolant channel	$1.600 \cdot 10^5$
Rotor	$1.095 \cdot 10^5$
Stator	$1.092 \cdot 10^5$

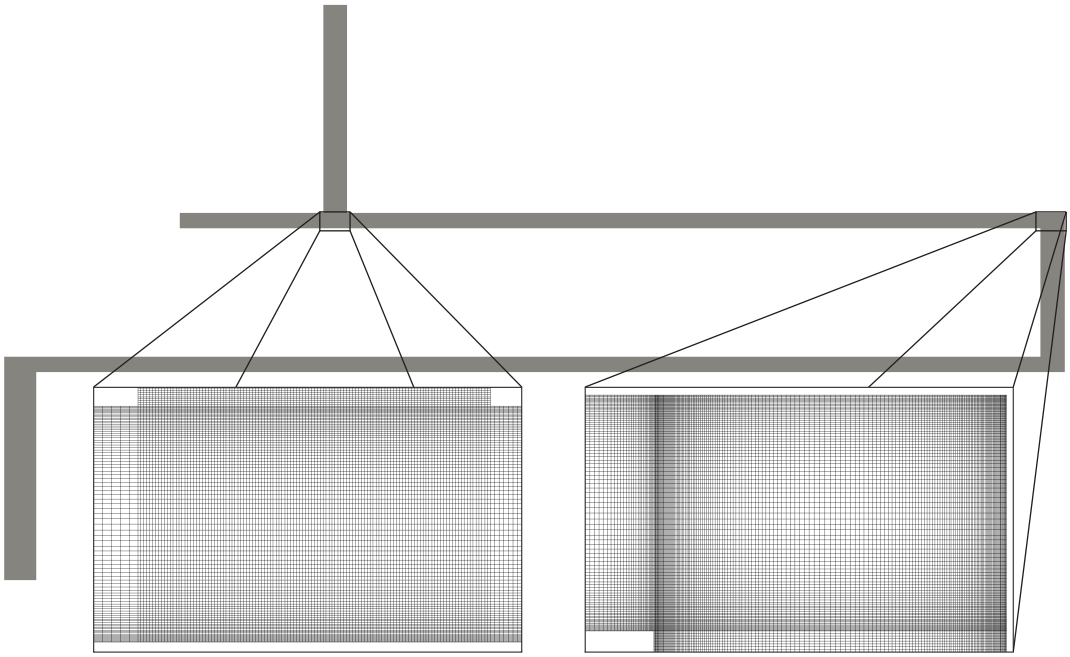

Figure 4.2: Detailed view of the reactor gap mesh: entire geometric domain, inlet and outer corner in the upper gap.

The flow and heat transfer simulations were initialized using solutions of preliminary simulations to reduce computation time. The calculations were performed on the CoolMUC2 linux cluster (Leibniz Rechenzentrum, Garching b. München, Germany). To obtain numerical convergence, about $9 \cdot 10^3$ and $2.1 \cdot 10^4$ iteration steps were necessary for the upper and lower coolant channels, respectively. For the flow simulations inside the reactor gap, iteration steps between $1.5 \cdot 10^4$ and $7.5 \cdot 10^4$ were necessary for the solution to converge. The heat transfer simulations reached convergence after $2 \cdot 10^5$ iteration steps.

4.3.4 Boundary conditions

For the fluid domains in the flow simulations, fixed inlet velocities were set, while a *pressureNormalInletOutletVelocity* applies at the respective outlets. The inlet velocities of the coolant channels were adjusted compared to the experimentally set values so that the Reynolds numbers inside the coolant channels aside the different geometries (real vs. simplified (Figure 4.1)) had about the same value and also resulted in similar values of the simulated heat fluxes in comparison to the experimental results [91]. At static walls, a no-slip condition was set for the velocity, while at rotating walls, the *rotatingWallVelocity* boundary condition was used to imprint a defined angular velocity. Since the reactant and coolant channel meshes were built to obtain low y^+ values (Equation (4.15) [121]) at stator and rotor walls, the low Reynolds approach for the wall treatment was applied.

$$y^+ = \frac{y\, u_\tau}{\nu}, \tag{4.15}$$

with the wall-normal coordinate y and the friction velocity at the nearest wall u_τ.

The maximum y^+ value obtained for the reactor gap in this study was 2 for the simulation case with a disc speed of $n = 500\,\mathrm{min}^{-1}$ and a dimensionless throughput of $C_W = 400$, though the average y^+ value at the walls of this simulation case was 0.35. Hence, for the turbulence quantities, fixed values of $1 \cdot 10^{-15}\,\mathrm{m^2\,s^{-2}}$ (≈ 0) were set at the walls for the turbulent kinetic energy and *zeroGradient* at the outlets, while a fixed value calculated via Equation (4.16) was set for the inlets. For the turbulent dissipation, the *zeroGradient* boundary condition was set at walls and outlets and a fixed value calculated via Equation (4.17) for the inlets. The boundary conditions of the specific rate of dissipation ω were set as *zeroGradient* at the walls and outlets and a fixed value, calculated via Equation (4.18), set for the inlet patches.

$$k_\mathrm{in} = \frac{3}{2}\,(u_\mathrm{in}\,I)^2 \tag{4.16}$$

$$\varepsilon_\mathrm{in} = 0.09\,\frac{k_\mathrm{in}^{3/2}}{L_\mathrm{t}} \tag{4.17}$$

$$\omega_\mathrm{in} = \frac{\sqrt{k_\mathrm{in}}}{L_\mathrm{t}} \tag{4.18}$$

In the above equations, u_in stands for the inlet velocity of the respective inlet patch, which is either the axial or radial velocity component, I for the turbulence intensity and L_t for the turbulent length scale. For the pressure, the outlet patches of the fluid domains were set to ambient pressure, whereas the *zeroGradient* condition was set for the inlet patches as well as the wall patches.

In the conjugate heat transfer simulations, fixed temperature values were set at the inlet patches of the fluid domains and *zeroGradient* at the outlet patches. The reactor medium inlet temperature was set to 54 °C and the coolant inlet temperatures to 25 °C. The solid patches to the surrounding were assumed adiabatic and the thermal coupling between solid-solid domains or solid-fluid was realized via the *compressible::turbulentTemperatureCoupledBaffleMixed* boundary condition supplied by OpenFOAM®.

For the respective front and back patches of the different domains, a *cyclic* condition was used for all quantities, since 5° wedge segments were considered for every domain.

4.3.5 Material properties

As stated before, material properties of the different domains were assumed constant as a first approach. For the fluid domains the properties of water at the respective mean

temperature, considered here as arithmetic mean of inlet and outlet temperature, of the corresponding experiment performed by Kleiner et al. [91] of the different operation points were set in the simulations. The material properties were determined via polynomials retrieved from the NIST data bank (cf. Appendix A.1.2). The material properties of the solid domains were constant for the different simulations and the values taken from material data sheets of the manufacturers for the material of the stator and rotor part of the real reactor setup. The stator material is an aluminum alloy with a density of $\varrho_{\mathrm{alu}} = 2665\,\mathrm{kg\,m^{-3}}$, a specific heat of $c_{p,\mathrm{alu}} = 900\,\mathrm{J\,kg^{-1}\,K^{-1}}$ and a thermal conductivity of $\lambda_{\mathrm{alu}} = 110\,\mathrm{W\,m^{-1}\,K^{-1}}$. The rotor material is steel with the following properties: $\varrho_{\mathrm{steel}} = 7900\,\mathrm{kg\,m^{-3}}$, $c_{p,\mathrm{steel}} = 500\,\mathrm{J\,kg^{-1}\,K^{-1}}$ and $\lambda_{\mathrm{steel}} = 15\,\mathrm{W\,m^{-1}\,K^{-1}}$.

4.4 Results and discussion

4.4.1 Velocity profiles

Exemplary results of radial and tangential velocity profiles across the dimensionless height z/s, with z being the axial position, are given in Figures 4.3 and 4.4 for different radial positions, rotational disc speeds and dimensionless throughputs, respectively. Figures 4.3a, 4.3c, 4.4a and 4.4c show velocity profiles at a dimensionless radius of $r/r_{\mathrm{r,o}} = 0.44$ and Figures 4.3b, 4.3d, 4.4b and 4.4d at a dimensionless radius of $r/r_{\mathrm{r,o}} = 0.92$, while Figures 4.3a, 4.3b, 4.4a and 4.4b show data for a constant disc speed of $n = 100\,\mathrm{min^{-1}}$ and Figures 4.3c, 4.3d, 4.4c and 4.4d for $n = 500\,\mathrm{min^{-1}}$. In order to ease understanding the figures in the results section, the dimensionless axial positions in the upper and lower reactor gap are referred to as follows: $z/s = 1$ corresponds to the upper boundary of the upper reactor gap at the stator, $z/s = 0$ is either the lower boundary of the upper reactor gap at the rotor or the upper boundary of the lower reactor gap at the rotor and $z/s = -1$ corresponds to the lower boundary of the lower reactor gap at the stator side.

At smaller radial positions and low disc speeds, the radial velocity profile appears parabolic and becomes more symmetric with increasing dimensionless throughput (cf. Figure 4.3a), whereas it gets distorted at larger radial positions so that a centrifugal boundary layer is present at the rotor and a centripetal one at the stator side (cf. Figure 4.3b). The same effect occurs with increasing disc speed for smaller radial positions (cf. Figure 4.3c) and is maximized at large radial positions and high disc speeds, in which case the influence of the throughput reduces to a minimum (cf. Figure 4.3d). Figure 4.3 further reveals merged boundary layers between the stator and rotor side (torsional-Couette flow), as is expected from the flow map introduced by Daily and Nece [65] for rotor-stator cavities with a small aspect ratio of $G = 0.0154$ and rotational Reynolds numbers between $Re_\Omega = 5 \cdot 10^4$ and $4.5 \cdot 10^5$. The radial velocity profiles in Figure 4.3 are in qualitative agreement with literature results [58, 59, 73] and demonstrate the validity of

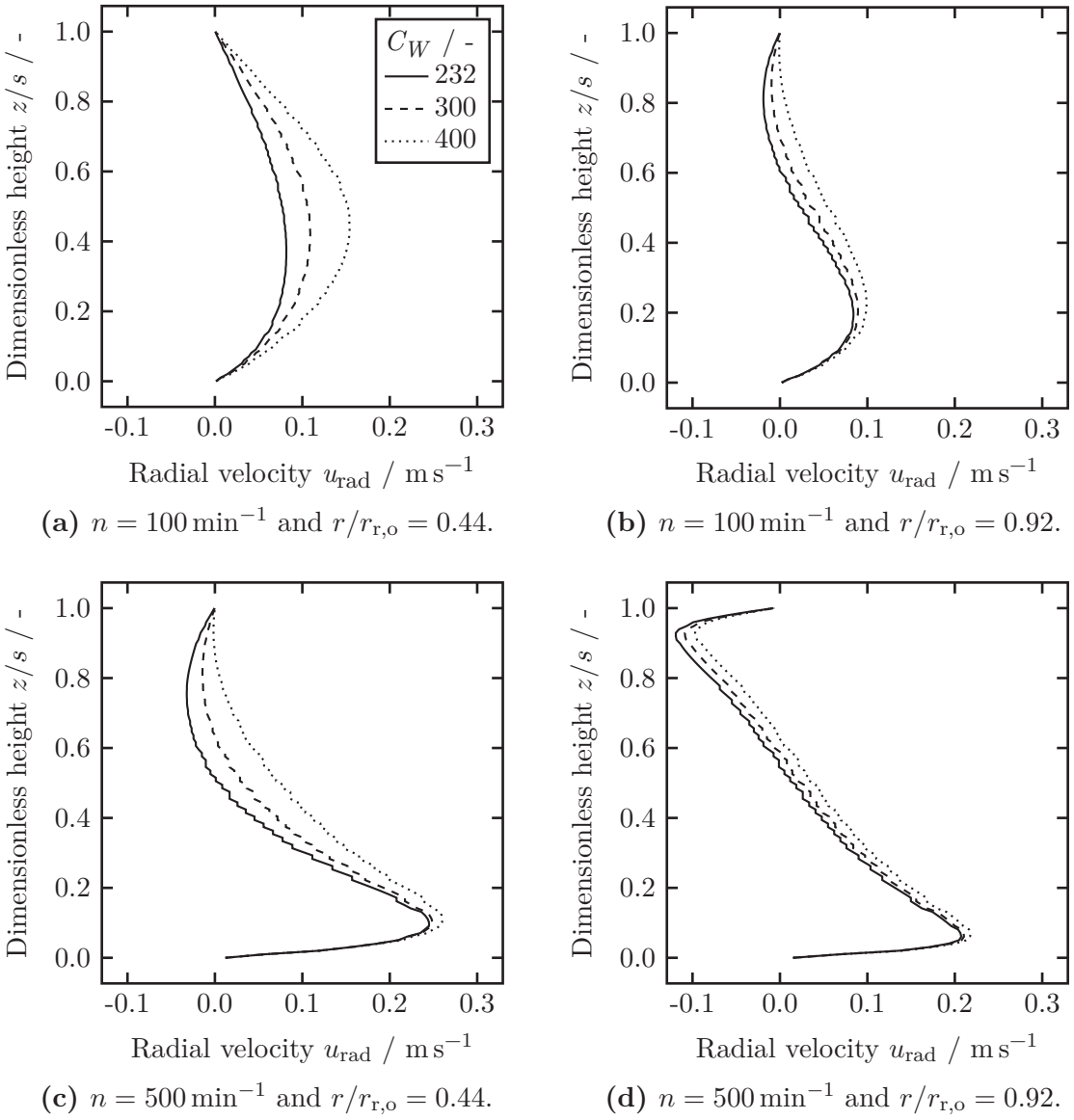

(a) $n = 100\,\mathrm{min}^{-1}$ and $r/r_{r,o} = 0.44$.

(b) $n = 100\,\mathrm{min}^{-1}$ and $r/r_{r,o} = 0.92$.

(c) $n = 500\,\mathrm{min}^{-1}$ and $r/r_{r,o} = 0.44$.

(d) $n = 500\,\mathrm{min}^{-1}$ and $r/r_{r,o} = 0.92$.

Figure 4.3: Radial velocity profiles across the upper reactor gap height at different rotational disc speeds and dimensionless radii for three dimensionless throughputs.

the flow simulations, aside the results shown in Appendix A.2.1. The same applies for the tangential velocity profiles in Figure 4.4, which reveal a Stewartson like profile with no boundary layer present at the stator side at smaller radial positions (cf. Figures 4.4a and 4.4c) [66]. This changes towards a torsional-Couette profile with boundary layers present at both rotor and stator side with higher rotational disc speeds and at larger radial positions (cf. Figure 4.4d).

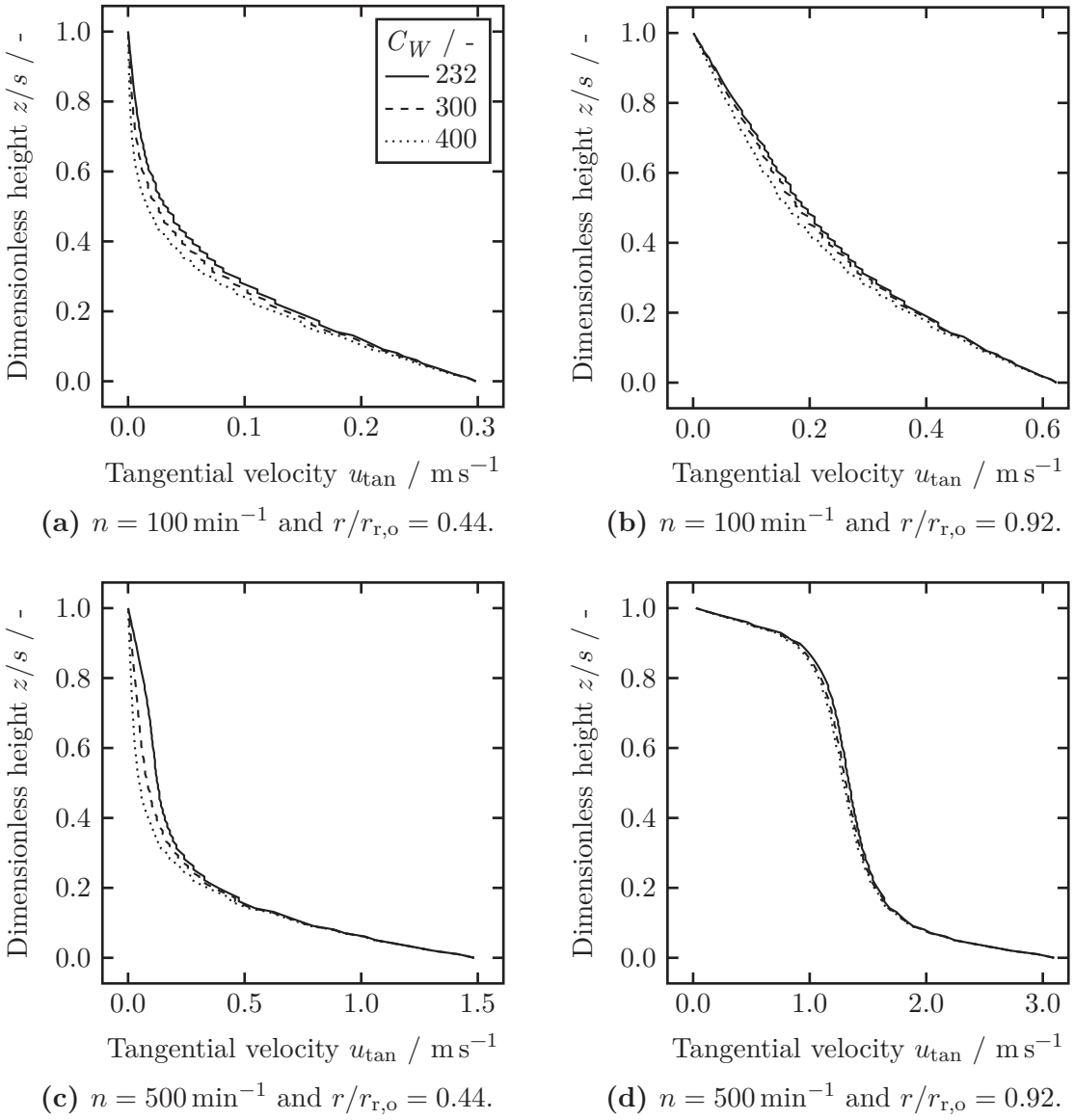

(a) $n = 100\,\mathrm{min}^{-1}$ and $r/r_{\mathrm{r,o}} = 0.44$.

(b) $n = 100\,\mathrm{min}^{-1}$ and $r/r_{\mathrm{r,o}} = 0.92$.

(c) $n = 500\,\mathrm{min}^{-1}$ and $r/r_{\mathrm{r,o}} = 0.44$.

(d) $n = 500\,\mathrm{min}^{-1}$ and $r/r_{\mathrm{r,o}} = 0.92$.

Figure 4.4: Tangential velocity profiles across the upper reactor gap height at different rotational disc speeds and dimensionless radii for three dimensionless throughputs.

4.4.2 Temperature profiles

Exemplary results of the axial temperature profiles across the upper and lower reactor gap at different radial positions in dependence of rotational disc speed and dimensionless throughput are illustrated in Figures 4.5 to 4.7. For the upper reactor gap, an almost parabolic axial temperature profile is observed right after the inlet ($r/r_{\mathrm{r,o}} = 0.32$), which changes into a steeper profile with increasing radial position with a small thermal boundary layer at the rotor and a considerably larger one at the stator side for moderate to high disc speeds for a constant dimensionless throughput of $C_W = 232$ (cf. Figure 4.5). The transition from the slightly parabolically shaped axial temperature profile to a steeper one with boundary layers at rotor and stator side right after the inlet occurs at a smaller radial position the smaller the dimensionless throughput. This would be expected, since

the parabolic profile is characteristic for radial temperature profiles in pipe flows [124], which is stronger present the higher the throughput (cf. Figure A.3 in Appendix A.2.2). Since the profiles in the upper reactor gap are distorted by the influence of the inlet, the focus of discussion is further laid on the results in the lower reactor gap. The axial temperature profiles in the lower gap for a constant throughput of $C_W = 232$ are shown in Figure 4.6 and reveal a decrease in boundary layer thickness on both rotor and stator side with increasing radial position as well as a rise in rotational disc speed. This observation is attributed to a higher degree of turbulence in the gap due to an increased local energy input. Figure 4.7 illustrates the development of the axial temperature profile in the lower reactor gap for a constant disc speed of $n = 300\,\mathrm{min}^{-1}$ with a change in radial position and dimensionless throughput; a decrease of the thermal boundary layer at the stator and rotor side is visible with a rise in throughput, which also results in slightly less steep axial temperature profiles at smaller radial positions.

In a qualitative comparison to similar rotor-stator cavities studied in literature, the axial temperature profiles in the lower reactor gap agree with results from Poncet et al. [73] as well as Djaoui et al. [67] and Beretta et al. [114], who also observed axial temperature profiles having a similar shape as the tangential velocity profile in the torsional-Couette regime [73].

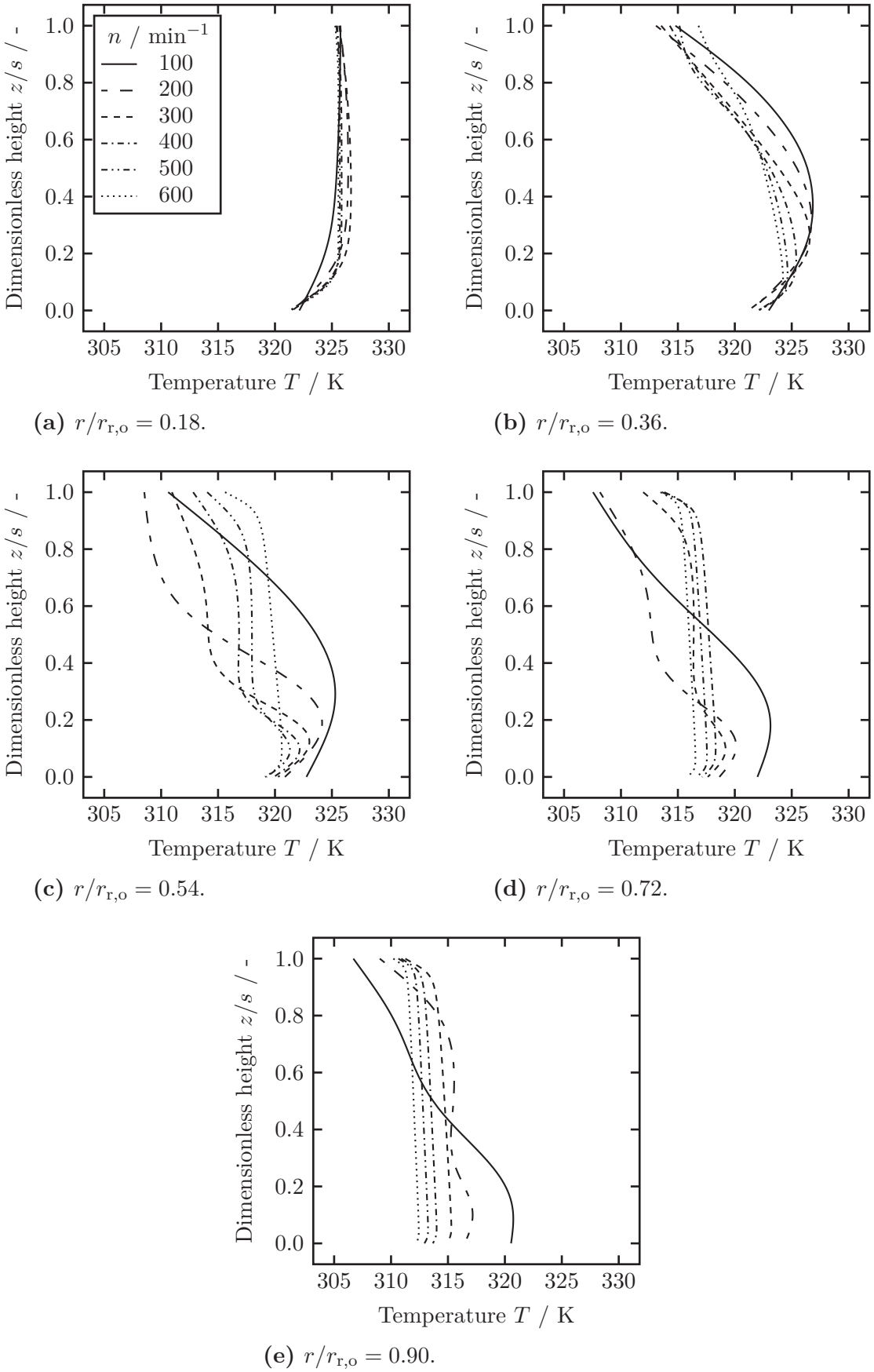

(a) $r/r_{\mathrm{r,o}} = 0.18$.

(b) $r/r_{\mathrm{r,o}} = 0.36$.

(c) $r/r_{\mathrm{r,o}} = 0.54$.

(d) $r/r_{\mathrm{r,o}} = 0.72$.

(e) $r/r_{\mathrm{r,o}} = 0.90$.

Figure 4.5: Temperature profiles across the upper reactor gap height at different dimensionless radii for a dimensionless throughput of $C_W = 232$ and six rotational disc speeds.

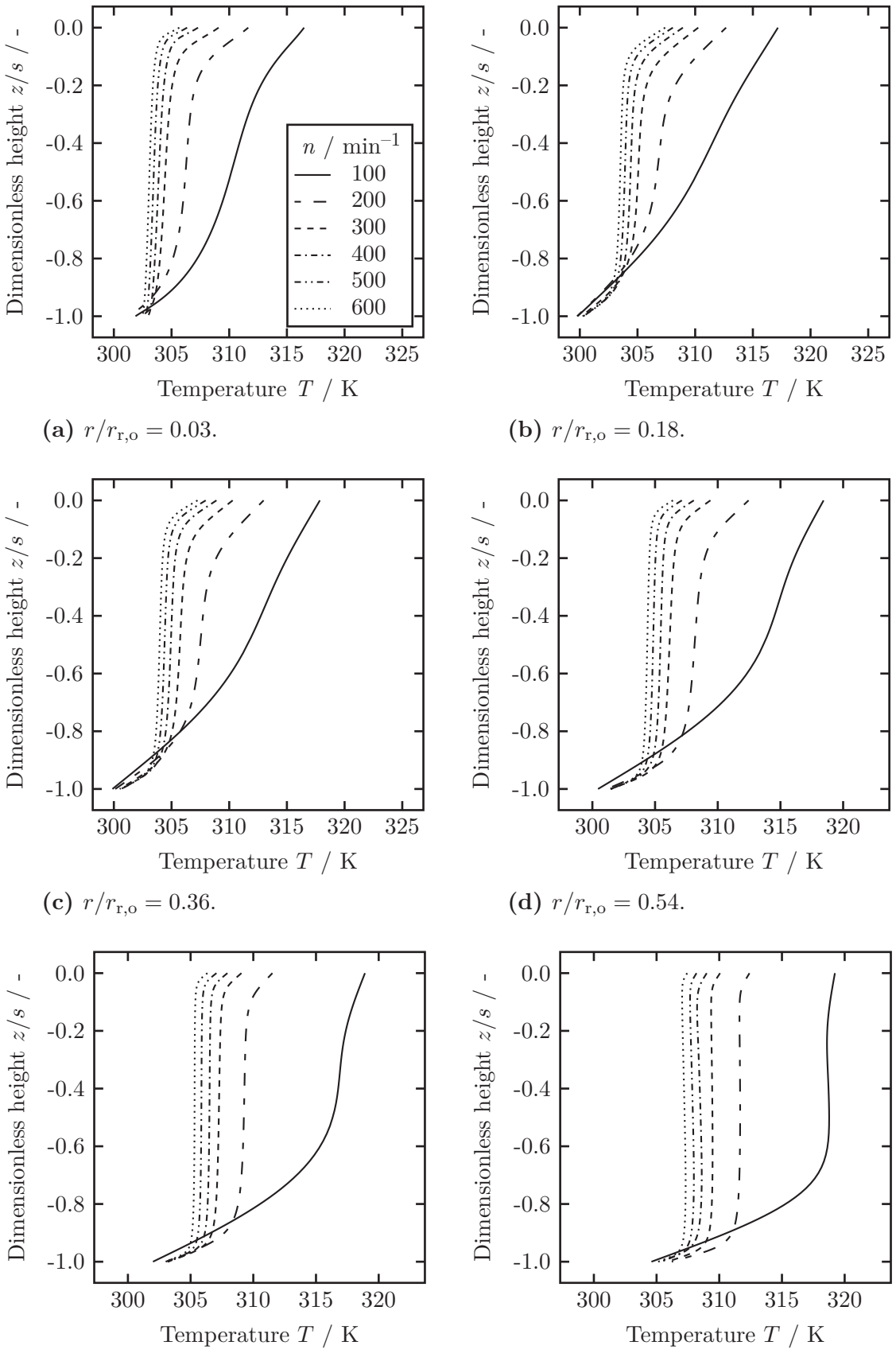

(a) $r/r_{\mathrm{r,o}} = 0.03$.

(b) $r/r_{\mathrm{r,o}} = 0.18$.

(c) $r/r_{\mathrm{r,o}} = 0.36$.

(d) $r/r_{\mathrm{r,o}} = 0.54$.

(e) $r/r_{\mathrm{r,o}} = 0.72$.

(f) $r/r_{\mathrm{r,o}} = 0.90$.

Figure 4.6: Temperature profiles across the lower reactor gap height at different dimensionless radii for a dimensionless throughput of $C_W = 232$ and six rotational disc speeds.

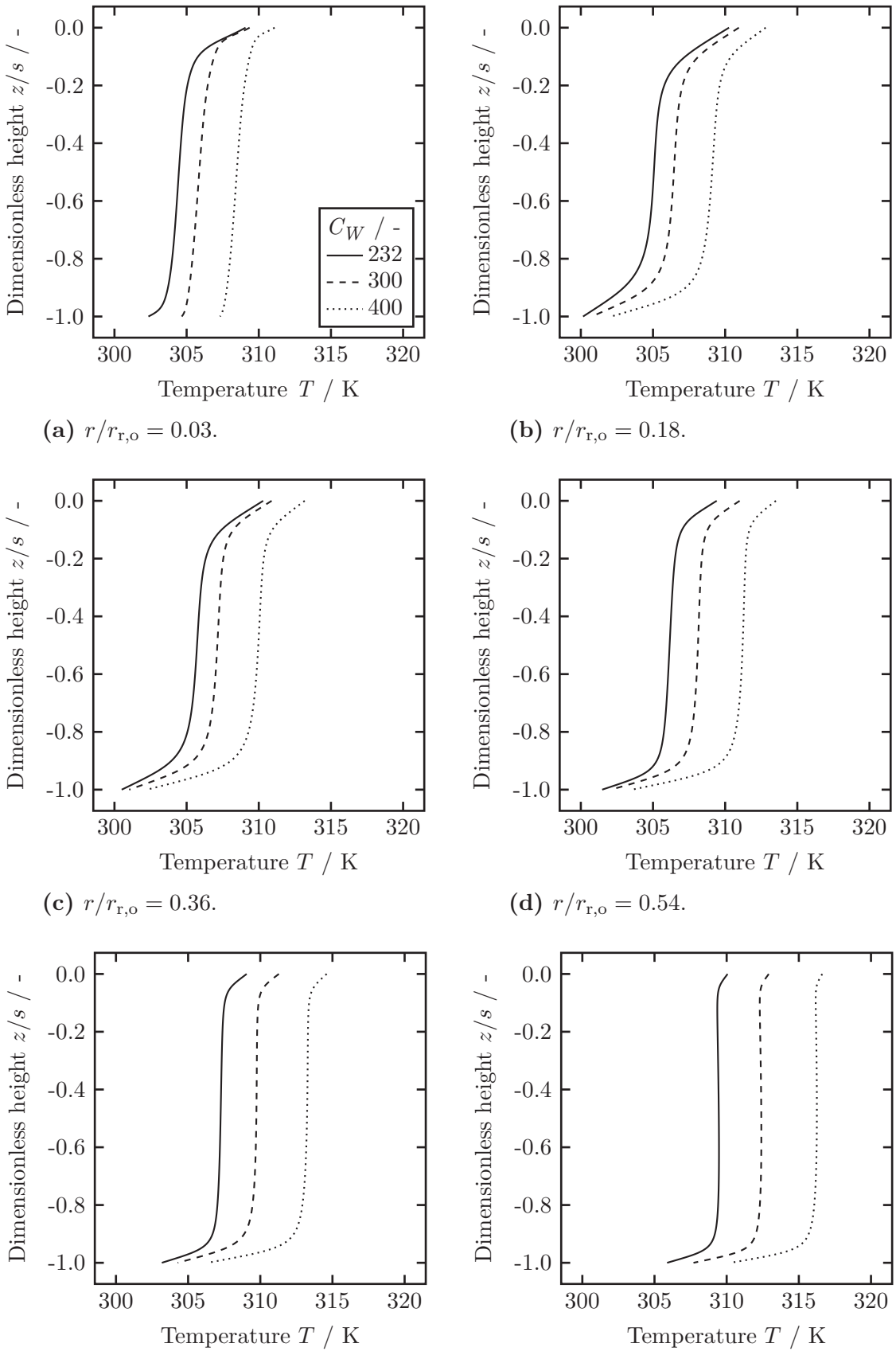

(a) $r/r_{\mathrm{r,o}} = 0.03$.

(b) $r/r_{\mathrm{r,o}} = 0.18$.

(c) $r/r_{\mathrm{r,o}} = 0.36$.

(d) $r/r_{\mathrm{r,o}} = 0.54$.

(e) $r/r_{\mathrm{r,o}} = 0.72$.

(f) $r/r_{\mathrm{r,o}} = 0.90$.

Figure 4.7: Temperature profiles across the lower reactor gap height at different dimensionless radii for a disc speed of $n = 300\,\mathrm{min}^{-1}$ and three dimensionless throughputs.

4.4.3 Heat transfer coefficients

In order to compare the numerical results of this study with stator-side heat transfer coefficient results from an experimental study on the three-dimensional version of the regarded setup, heat transfer coefficients were determined via Equation (4.19).

$$\dot{q} = \alpha_{\mathrm{s,loc}} \left(T_{\mathrm{s}} - T_{\mathrm{b}} \right) \tag{4.19}$$

$\dot{q}$ stands for the local wall heat flux, T_{s} for the respective local temperature at the stator wall and T_{b} for the local bulk temperature of the fluid in the reactor gap. For the fluid in the lower gap, the bulk temperature was always the temperature value at half the height of the lower gap, as the temperature profiles indicate almost constant temperature values across the majority of the axial gap, aside from the boundary layers at rotor and stator side for most of the evaluated operating conditions and radial positions, except for very low radii and low disc speeds (cf. Figures 4.6 and 4.7). The results for the lower gap of the just described determination of local stator-side heat transfer coefficients are given in Figure 4.8.

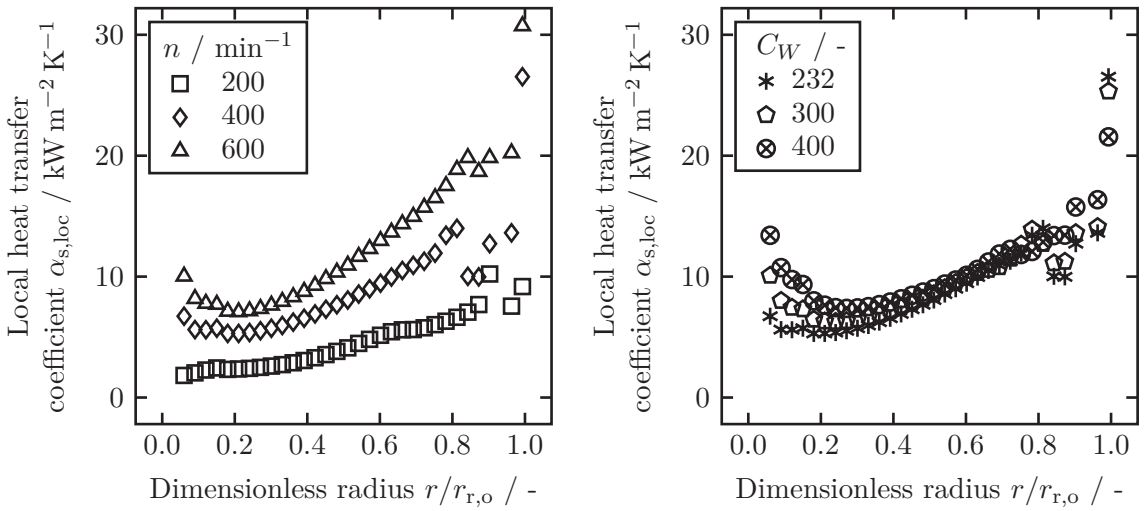

(a) $C_W = 232$. **(b)** $n = 400\,\mathrm{min}^{-1}$.

Figure 4.8: Local stator-side heat transfer coefficients in dependence of radial position in the lower reactor gap, rotational disc speed and dimensionless throughput.

For the determination of the stator-side heat transfer coefficients in the upper reactor gap, either the temperature at half the height of the upper gap was taken or the local temperature maximum of the axial temperature profile was used, if applicable, as the temperature profiles at lower radial positions in the upper gap are not constant across the central core part of the gap height due to the influence of the reactor inlet.

Figure 4.8a shows local stator-side heat transfer coefficients for the lower reactor gap in dependence of radial position and rotational disc speed for a constant dimensionless

throughput of $C_W = 232$. An increase in local heat transfer coefficient with a rise in rotational disc speed is observed in Figure 4.8a, which is stronger at higher radial positions, due to higher tangential velocities ($\Omega\, r$). With an increase in radius, the local heat transfer coefficients first decline before they rise with increasing radial positions (cf. Figure 4.8) [67]. This behavior is due to the interplay of the influence of the superimposed throughput and rotation, as the velocity of the superimposed flow decreases reciprocally with radius, whereas the influence caused by rotation rises with radius. Figure 4.8b illustrates local stator-side heat transfer coefficients for a constant rotational disc speed of $n = 400\,\mathrm{min}^{-1}$ in dependence of dimensionless throughput; a rise in heat transfer coefficient is visible with increasing throughput at lower radial positions, up to about $r/r_{\mathrm{r,o}} = 0.46$. However, this effect decreases at larger radii, where rotation overrules the throughput effects (cf. Figure 4.8b). At very high radial positions, single data points show deviations from the trend (cf. Figure 4.8). This could be attributed to vortex structures in the flow field in the axial gap connecting the upper and lower radial gap, which reach into the outer parts of the upper and lower radial gap.

The results of the local heat transfer coefficients are in qualitative agreement with literature results for rotor-stator setups [67, 73]. For further validation of the numerical results of this study with experiments performed at the setup, which was simulated in this work, area-averaged stator-side heat transfer coefficients α_{s} were determined across the entire reactor gap. Therefore, each local stator-side heat transfer coefficient was weighted with the area of the respective annulus in order to determine averaged heat transfer coefficients for the upper and lower gap, respectively. The averaged stator-side heat transfer coefficients of the upper and lower gap were then weighted with their corresponding heat exchange area, thus, resulting in an area-averaged stator-side heat transfer coefficient for the entire gap. Figure 4.9 presents the average stator-side heat transfer coefficients of the results from this study in comparison to results based on experimental work [91] in dependence of rotational disc speed for three dimensionless throughputs.

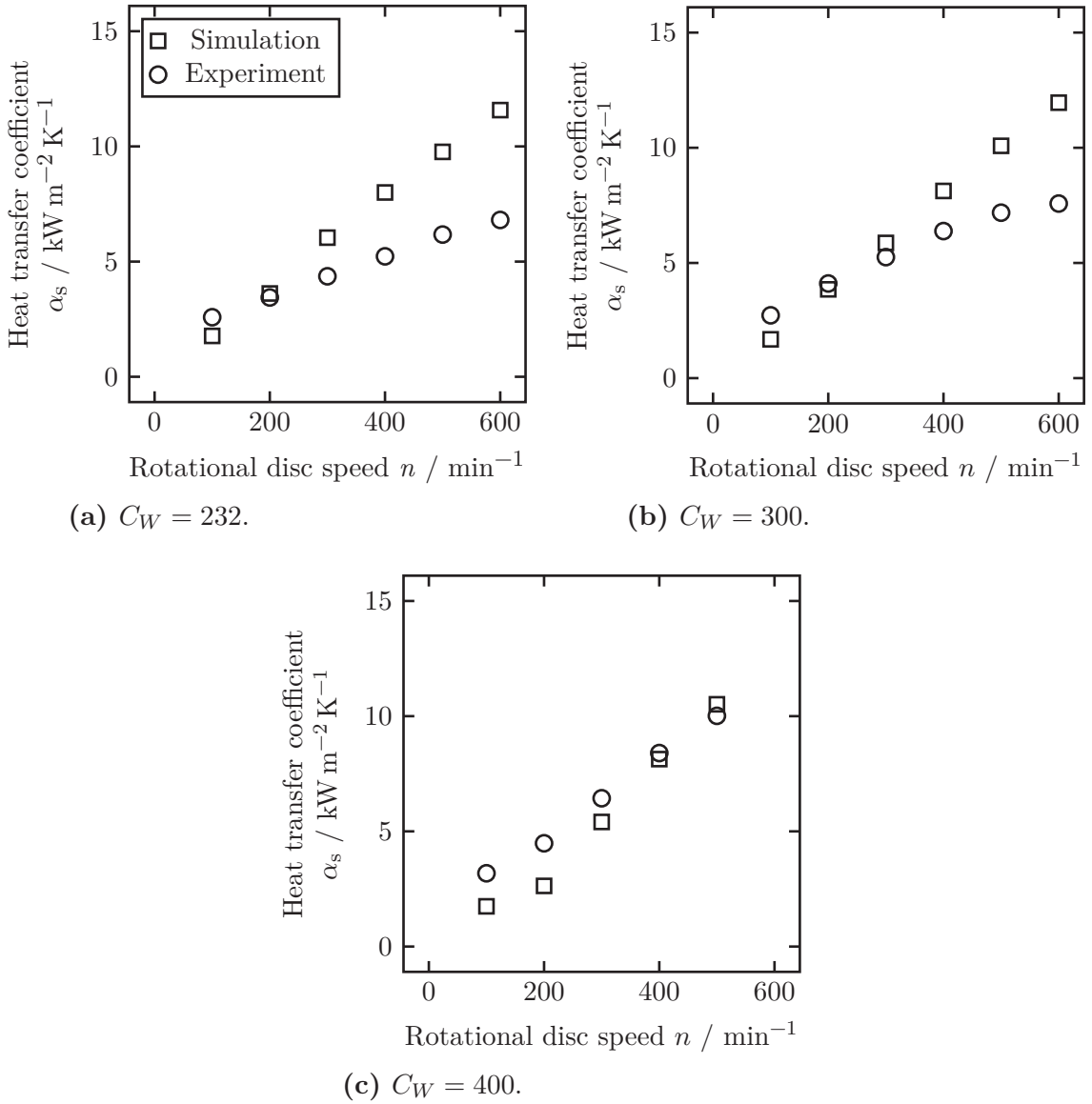

(a) $C_W = 232$.

(b) $C_W = 300$.

(c) $C_W = 400$.

Figure 4.9: Comparison between the area-averaged heat transfer coefficients from the CFD simulations and the experimentally determined heat transfer coefficients from Kleiner et al. [91] in dependence of rotational disc speed for three dimensionless throughputs.

As can be seen in Figure 4.9, the numerical results show similar trends as the results deduced from experimental data and the values are further within the same order of magnitude. An increase in average stator-side heat transfer coefficient with rising rotational Reynolds number is visible, as also observed for the experimental data [91]. The agreement between numerical and experimental results is the highest for the largest dimensionless throughput considered in this study (cf. Figure 4.9c). This phenomenon might be explained considering that the suitability of the *Lien-Leschziner* turbulence model for the simulations of this study was validated against literature results with mainly very high absolute dimensionless throughput values compared to the parameter range of this study. Moreover, according to Iacovides et al. [104], three-dimensional and buoyancy

effects, which are assumed negligible in this study, should become more important for smaller Rossby numbers (Equation (4.20)).

$$Ro = \frac{\dot{V}_\mathrm{R}}{2\,\pi\,r_{\mathrm{r,o}}^2\,(r_{\mathrm{s,i}} - r_{\mathrm{r,o}})\,\Omega} \tag{4.20}$$

It should also be taken into consideration that the data based on the experiments firstly underlies measurement uncertainties of about 7 % [91] and secondly, the experiments were evaluated with the aid of the reactor model for an RSSDR by de Beer et al. [31], which already introduces several assumptions and most importantly assumes a constant heat transfer coefficient for the entire reactor gap. In addition, in the determination of the stator-side heat transfer coefficients from the experiments, a one-dimensional enthalpy balance was solved with further simplifications making the experimental data evaluable [91]. In addition, this study is a 2.5D approach to simulate a three-dimensional reactor setup. Meshing and simulating a three-dimensional geometry of the real setup will probably increase accordance between experimental and numerical data, but also increase computation times drastically. It could also be argued that instead of a two-equation RANS approach, an RSM for turbulence modeling or even a large eddy simulation approach should be used to better resolve the complex turbulent flow in the regarded system. This would increase accuracy of the numerical results, but was not scope of this work, as it is important for industrial applications to plan and design reactor setups efficiently on the one hand and accurately enough on the other hand. Considering the simplifications made for evaluating the experimental data and for the simulations of this study, accordance between the different results (cf. Figure 4.9) is considered good and the method of a 2.5D reactor geometry simplification with a RANS turbulence modeling approach justified. Furthermore, the experimental results used for comparison in this study show a transition from a laminar to a turbulent flow regime with respect to the rotational Reynolds number at around 10^5 [91]; this is also observed for the numerical results in this study (Figure 4.10), suggesting further that the applied methodology could be used to qualitatively predict heat transfer properties in RSSDRs.

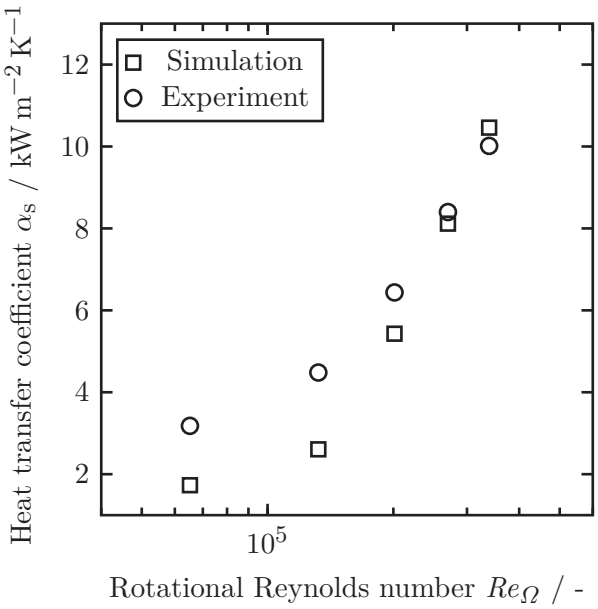

Figure 4.10: Comparison between the stator-side heat transfer coefficients from the CFD simulations and the experimentally determined heat transfer coefficients from Kleiner et al. [91] in dependence of rotational Reynolds number for a dimensionless throughput of $C_W = 400$.

Comparing the results of this study with further literature data, as was similarly done by Kleiner et al. [91] (cf. Section 3.6.4), it can be seen that the current results lie within the same order of magnitude as results for stator- or rotor-side Nusselt numbers found in literature and have similar trends with respect to the rotational Reynolds number; this is illustrated in Figure 4.11, which is a modification of Figure 3.13 in Section 3.6.4 with the addition of the theoretical data gained in this study, showing stator- and rotor-side Nusselt numbers of various rotor-stator setups found in literature [21, 56, 73, 81, 91, 94].

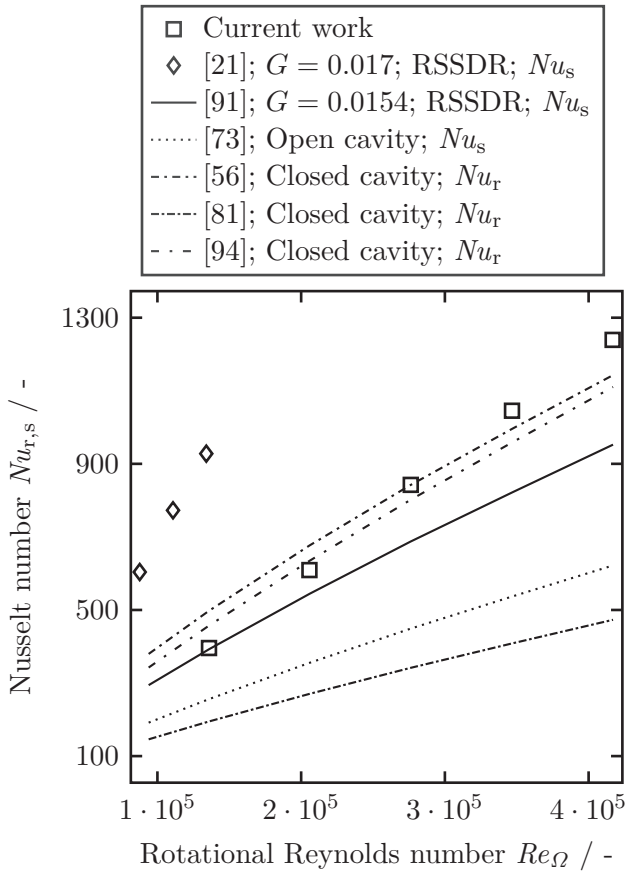

Figure 4.11: Comparison of literature results with current work. Data of stator-side Nusselt numbers of a multi-stage RSSDR by de Beer et al. [21] is shown as well as a Nusselt correlation for a single-stage RSSDR [91] and an open cavity for the turbulent regime [73]. Rotor-side Nusselt number correlations for a closed cavity within the turbulent regime by Owen [56], Nikitenko [81] and Shchukin [94] are indicated. The data is given for a dimensionless throughput of $C_W = 300$ and a Prandtl number of $Pr \approx 4$. Literature data is adjusted by $(Pr_{\text{water}}/Pr_{\text{air}})^{0.52}$, if applicable [21].

4.5 Conclusion

A 2.5D CFD study on hydrodynamics and heat transfer in an RSSDR using the open-source software OpenFOAM® was performed with a RANS turbulence modeling approach. The *Lien-Leschziner* turbulence model implemented in OpenFOAM® was used for the flow simulations of this study, as in preparatory work this model was found to be appropriate to simulate fluid flow of rotor-stator reactors with superimposed throughput.

The results of velocity profiles gained from the simulations are in qualitative agreement with literature results [58, 59, 66, 73]. The radial velocity profiles show torsional-Couette behavior for large parts of the radial gap and considered disc speeds; the tangential velocity profiles feature Stewartson like behavior at small radial positions and disc speeds and torsional-Couette behavior with increased disc speed and radial position.

The obtained temperature profiles across the gap height also agree with literature results [67, 73, 114]; the temperature profiles in the lower reactor gap show similar shapes as the tangential velocity profiles in the torsional-Couette regime [73]. A decrease in thermal boundary layer thickness with a rise in disc speed and throughput was observed and steeper axial temperature profiles were obtained with an increase in disc speed and a decreasing throughput.

Locally resolved stator-side heat transfer coefficients were determined from the simulations, which show an increase with higher rotational disc speeds and after a slight decrease at lower radial positions, an increase with rising throughput, which is in agreement with literature [67, 114]. Area-averaged stator-side heat transfer coefficients for the entire reactor gap were calculated in order to validate the results of this study against results based on experimental work by Kleiner et al. [91]; the numerical and experimental data show good agreement taking into account the assumptions in this study to reduce computational expense as well as measurement uncertainties of the experimental work and furthermore simplifications made when evaluating the experiments.

This study shows the possibility to characterize hydrodynamics and heat transfer properties of RSSDRs with the aid of a 2.5D reactor geometry and a RANS turbulence modeling approach in OpenFOAM®. It is, thus, possible to avoid expensive measurements, which are difficult to perform especially for rotor-stator reactors with small dimensions, but to simulate the conditions of interest for an industrial application and design the rotor-stator reactor setup based on numerical studies.

5 Epoxidation of methyl oleate in a rotor-stator spinning disc reactor

This chapter was published in a similar way as:

J. Kleiner, O. Hinrichsen, Epoxidation of methyl oleate in a rotor-stator spinning disc reactor. *Chem. Eng. Process.* 136 (2019) 152−162 [83].
Reprint with permission from *Elsevier*.

5.1 Abstract

The intensification of the epoxidation of methyl oleate with hydrogen peroxide and formic acid in a rotor-stator spinning disc reactor (RSSDR) was studied in dependence of temperature, rotational disc speed and reactor throughput. The application of TiO_2 as a heterogeneous catalyst immobilized with Nafion® as adhesive on the rotor disc was also examined. Optimum values for the regarded parameters with respect to conversion and yield were 80 °C, 1000 min^{-1} and 50 mL min^{-1}. The use of TiO_2 as a catalyst yielded no beneficial results as opposed to a plain steel rotor. A significant increase in yield and conversion was achieved with the RSSDR in comparison to comparative batch experiments. The average rates of epoxide production in the RSSDR are about a factor four higher than the batch experiments. In comparison to literature results of similar reaction systems, but different reactors, in particular microreactors, the RSSDR shows values in the same order of magnitude and even outperforms catalyst-coated microreactor systems. This study shows that the RSSDR with its very good heat and mass transfer properties allows to significantly intensify epoxidation of fatty acid methyl esters (FAMEs).

5.2 Introduction

Epoxidized FAMEs are starting materials for a variety of industrial products, e.g., plasticizers, stabilizers for polyvinyl chloride resins, lubricants, cosmetics, pharmaceuticals

and bio-fuel additives [32–37]. In industry, Prilezhaev epoxidation of, e.g., vegetable oils is realized by the reaction of the double bonds with peracetic or performic acid, which are generated in situ from concentrated hydrogen peroxide and acetic or formic acid, respectively, in the presence of a mineral acid [33, 85]. The generated peroxyacid migrates from the water to the oil phase and reacts with the double bond of the FAME to form an oxirane ring and the respective acid [33, 90]. While hydrogen peroxide as oxidant is very attractive, since it is transformed into water during the reaction, it introduces a safety risk, as the epoxidation of the double bond is quite exothermic ($\Delta H_R = -230.2\,\mathrm{kJ\,mol^{-1}}$ [33]). Therefore, the epoxidation is often carried out in a semi-batch operational mode, in which hydrogen peroxide is slowly fed to the reaction mixture to guarantee isothermal conditions and increase safety control [32]. Unfortunately, this usually leads to long reaction times of several hours [32, 36, 89]. The usage of a mineral acid, e.g., sulphuric acid, which is reported to work best as a homogeneous catalyst in the formation of peroxyacids, is undesirable due to its environmentally unfriendly properties as well as necessary separation and neutralization steps [32, 34]. Besides the above mentioned challenges, epoxidation of FAMEs with peroxyacids entails mixing two immiscible fluids, since solvents are to be avoided due to environmental aspects [32, 125]. Hence, good mass and heat transfer properties as well as the possibility to catalyze the reaction heterogeneously are desirable characteristics for a reactor system to carry out Prilezhaev epoxidation of a FAME such as methyl oleate (MO) also called oleic acid methyl ester to *cis*-9,10-epoxystearic acid methyl ester or epoxidized methyl oleate (EMO) with in situ generated performic acid (cf. Figure 5.1).

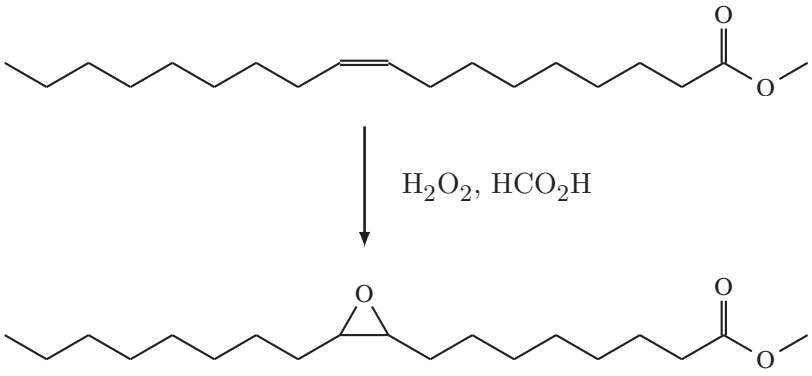

Figure 5.1: Schematic of the epoxidation of methyl oleate with hydrogen peroxide and formic acid to *cis*-9,10-epoxystearic acid methyl ester.

Figure 5.2, which is based on Campanella et al. [126], illustrates how the reaction shown in Figure 5.1 proceeds. In the aqueous phase, hydrogen peroxide and formic acid react to performic acid, which migrates from the aqueous to the organic phase, where it reacts with MO to form EMO and formic acid again. In dependence of different operating and reaction parameters (temperature, molar ratios of olefin, formic acid and hydrogen peroxide, etc.) several ring opening and side reactions (cf. Section 2.2.1) may occur, resulting in lower selectivities and yields of the target product.

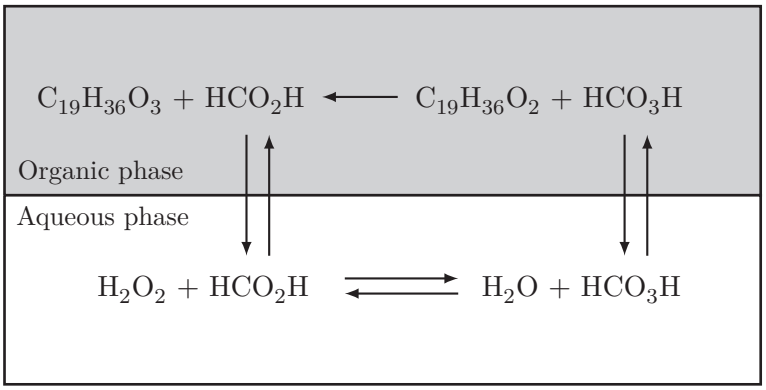

Figure 5.2: Schematic of the reaction of hydrogen peroxide and formic acid to performic acid and water in the aqueous phase, the migration of formic acid and performic acid between aqueous and organic phase, respectively, and the epoxidation of methyl oleate with performic acid in the organic phase based on Campanella et al. [126].

The RSSDR is an innovative reactor technology, which addresses intensification of heat and mass transfer limited reactions [21, 31, 91, 106] and further allows to catalyze a reaction heterogeneously [23]. Similar to microreactors, the RSSDR was engineered under the term process intensification (PI), which aims at increasing operational safety and environmental friendliness of a chemical process, while reducing equipment size and production costs [17, 35]. Many studies on RSSDRs were conducted during the past decade focusing on residence time distributions [31, 40, 42], micromixing properties [23, 24], stator- or rotor-side heat transfer [21, 29, 30, 50, 91, 106], liquid-solid [23, 25, 127], gas-liquid [26–28] and liquid-liquid mass transfer properties [45]. The latter was investigated by Visscher et al. [46] who also examined flow behavior of water and *n*-heptane mixtures and the resulting volume fractions at different operating conditions in rotor-stator reactors. They found that for low rotational disc speeds large droplets of the organic phase are present which decrease with increasing disc speed, thus, increasing the contact area between the two phases [46].

Prilezhaev epoxidation has never been carried out in an RSSDR so far. Most studies found in literature report on epoxidation of olefins in microreactors. Wan et al. [128], e.g., studied epoxidation of 1-pentene with hydrogen peroxide in a microfabricated flow reactor. He et al. [35] investigated epoxidation of soybean oil in a continuous microflow system with a continuous separation system; they used formic acid as oxygen carrier, hydrogen peroxide as oxidant and sulphuric acid as a homogeneous catalyst. Torrente-Murciano et al. [129] performed a study on biphasic epoxidation of sunflower seed oil with hydrogen peroxide and a homogeneous sodium tungsten-based catalyst in microtubular reactors without any surfactant. Prilezhaev epoxidation of a FAME in a heterogeneously catalyzed microcapillary reactor was studied by Phimsen et al. [32]; they coated the wall of the capillary reactor with TiO_2 and observed a significant increase in oxirane yield, which they explained by the beneficial role TiO_2 plays in the performic acid formation.

The usage of TiO_2 or titanium-based materials is often found for epoxidation or oxidation reactions in literature. Gallo et al. [130] investigated epoxidation of cyclooctene using Ti containing mesoporous materials. Klemm et al. [131] reported on direct gas-phase epoxidation of propene with hydrogen peroxide in a microstructured reactor on a Ti containing silicate-1 (TS-1) zeolite. Epoxidation of MO with hydrogen peroxide and Ti containing silica solids as catalyst was studied by Guidotti et al. [89], who also compared ordered and non-ordered mesoporous materials as catalysts in the epoxidation of unsaturated FAMEs [36]. TS-1 as catalyst was further used by Truter et al. [132] for selective oxidation reactions in microreactors. Parida et al. [125] studied the solvent-free epoxidation of cyclohexene with hydrogen peroxide by a Ti(IV)−Schiff base complex-intercalated layered double hydroxide catalyst. Nanosized Ti/SiO_2 was used by Kumar and Ali [133] for epoxidation of FAMEs and triglycerides.

Exploiting the advantage of a heterogeneously catalyzed epoxidation reaction in an RSSDR entails the challenge of permanently immobilizing a desired catalyst material on the rotor disc; the catalyst layer needs to adhere to the rotor disc even at high rotational disc speeds, which cause large shear forces acting on the catalyst layer. Hence, a static method as used by Phimsen et al. [32], in which they dissolved catalyst material in a volatile solvent, filled the reactor system with such solution and evaporated the solvent under vacuum conditions, is ruled out for operation with the RSSDR, since the authors reported that under microflow conditions the catalyst was peeled off after about 3 h of operation. As Haseidl et al. [23] reported using a Pt/C coated rotor disc, which they coated with a catalyst ink containing the active material as well as Nafion® as adhesive, for oxidation of glucose in an RSSDR, a similar approach was pursued in this study. TiO_2 and Nafion® in combination are often found in electrochemical applications, in which, e.g., Nafion® and TiO_2 membrane electrode assemblies are prepared via a recasting method [134, 135] or a dropcasting technique [136–138], which entail sonication for preparation of the inks and casting the mixture on a substrate for drying. The preparation of the catalyst inks as described by Park and Choi [139], first mixing Nafion® solution and TiO_2 powder and letting it dry over night, before adding water and homogenizing the mixture, was chosen for preparation in this study due to performance issues of the prepared ink. The coating of the rotor disc was similarly done as described by Haseidl et al. [23] with a rod coating apparatus.

The presented studies applying microreactor systems and Ti containing catalyst systems all aim at employing the advantages of heterogeneous catalysis and microreactor systems to overcome mass transfer limitations and guarantee good temperature control in case of the microreactor system. The same considerations apply for the RSSDR, which, besides good mass and heat transfer properties, allows easy scale-up [39] as well as higher throughputs as opposed to microreactors; it is further unsusceptible to fouling due to high shear forces and clogging, since it does not entail narrow microchannels [9]. Therefore, in this study, the intensification of the epoxidation reaction of MO with hydrogen peroxide

and formic acid in an RSSDR was investigated in dependence of rotational disc speed, temperature and volumetric throughput with and without a TiO_2 coated rotor disc as catalyst.

5.3 Methodology

5.3.1 Setup

The experimental setup used in this study is schematically illustrated in Figure 5.3. The RSSDR has a rotor radius of $r_{\mathrm{r,o}} = 65\,\mathrm{mm}$ with a rotor height of $s_{\mathrm{r}} = 8\,\mathrm{mm}$, a gap height of $s = 1\,\mathrm{mm}$, a drive shaft radius of $r_{\mathrm{r,i}} = 11\,\mathrm{mm}$ and a radial clearance between the stator housing and the outer rotor radius of $r_{\mathrm{s,o}} - r_{\mathrm{r,o}} = 1.5\,\mathrm{mm}$. The stator in which the rotor (both made of stainless steel) is cylindrically enclosed has integrated coolant channels for temperature control. Either a jacketed reaction vessel ($V = 150\,\mathrm{mL}$) or a round-bottomed flask ($V = 100\,\mathrm{mL}$) in a water bath is placed on a magnetic stirrer (MR Hei-Tec, *Heidolph*) below the outlet of the RSSDR. The hydrogen peroxide reservoir is placed next to it.

The coolant (deionized water) medium for temperature control in the RSSDR and the jacketed vessel is supplied and tempered by a thermostat (*Haake* DC50); in case the round-bottomed flask was used, the reaction vessel was tempered by a water bath controlled by the magnetic stirrer. An *ISMATEC* tooth wheel pump (type BVP-Z) controlled by a mini CORI-FLOW mass flow controller by *Bronkhorst* (type M15-ABD-33-O-S) pumps the medium through the RSSDR coolant channels, whereas the built-in pump cycle of the thermostat was used for pumping the medium through the jacket of the reaction vessel. The inlet and outlet temperatures of the coolant medium of the RSSDR were monitored with type J thermocouples (NI USBTC01, *Texas Instruments*). One peristaltic pump (TL/150, *Medorex*) pumps the reaction mixture in a cycle from the vessel through the RSSDR gap back to the vessel and another one (TL/150, *Medorex*) doses the hydrogen peroxide from the reservoir into the vessel. The rotor is powered by a *LENZE* SE RS100 motor.

5.3.2 Procedure

RSSDR experiments

The epoxidation reaction in the RSSDR was carried out by filling the desired amount of MO (technical grade, C18 : 1 > 65 %, *Alfa Aesar*) and formic acid (99 % − 100 %, *VWR*) in the jacketed vessel/round-bottomed flask located below the RSSDR. The molar

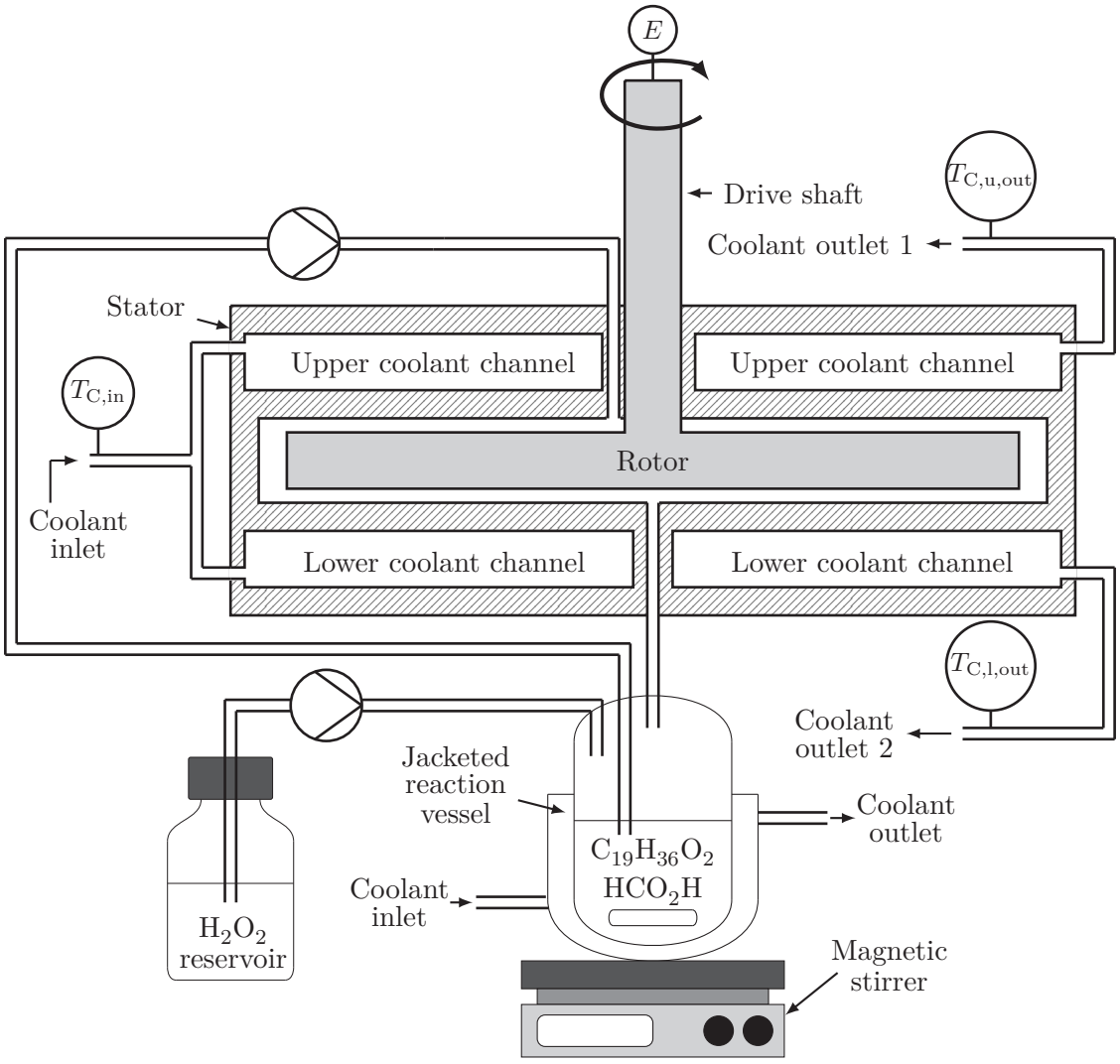

Figure 5.3: Schematic flow diagram of the experimental setup.

ratio of MO, hydrogen peroxide and formic acid in this study was mainly: $C_{19}H_{36}O_2$: H_2O_2 : HCO_2H = 1 : 4 : 4, as this (or a similar) ratio was reported to work well in Prilezhaev epoxidation [32, 35, 140], even though some authors report that the formic acid amount should not be too high, as it could lead to ring opening reactions [88, 140]. The mixture was stirred at 500 $\mathrm{min^{-1}}$ with the magnetic stirrer and tempered by a water bath or water from the thermostat flowing through the jacket of the vessel and through the coolant channels of the RSSDR (cf. Figure 5.3). The thermostat temperature was always set 0.5 K higher than the desired temperature in the reaction vessel and RSSDR to guarantee the desired temperature of the reaction mixture, which was checked several times. The mixture was pumped in a recycle from the batch through the RSSDR entering the reactor at the top near the center and leaving at the bottom center, from which it led back into the batch vessel. After 5 min, the mixture was at the desired reaction temperature and hydrogen peroxide (30 % for synthesis, *Merck*) was slowly added into the batch vessel initiating the reaction. The reaction mixture was pumped through the RSSDR in a recycle for a reaction time of 5 min. The volume flow of the added hydrogen

peroxide was adjusted to account for half of the reaction time. After a reaction was finished, the cycle was opened and the reaction mixture was immediately collected and transferred into a separating funnel placed in ice water. The water phase was discarded and the oil phase was prepared for gas chromatography (GC) analysis. The oil phase was first centrifuged (*Heraeus Pico 21*) to remove last residues of water in the phase and then a small amount of the produced oil phase was pipetted in a GC vial together with *n*-pentadecanoic acid methyl ester (97 %, *Abcr*) as internal standard and ethyl acetate (99.9 %, *VWR*) as solvent. A different parameter was varied each experiment, while the others were kept constant; temperature was varied between 50 °C and 90 °C, throughput of the recycle between 35 mL min^{-1} and 75 mL min^{-1} and the rotational disc speed between 40 min^{-1} and 3000 min^{-1}.

Batch experiments

In order to assess the performance of the RSSDR, comparative experiments with two batch reactor setups were performed. To ensure similar flow and mixing conditions in the batch vessel, batch experiments were first carried out with a reduced reaction volume and without a recycle (batch experiments). Secondly, batch experiments were performed with the same reaction volume as used in the RSSDR experiments and with a recycle; this operational configuration will be abbreviated with BWR, which stands for "batch with recycle". The respective volumes of the different reactor or peripheral parts with respective residence times are given in Table 5.1.

Table 5.1: Volumes and total residence times of the different setup parts of the experiments performed in the RSSDR with a total reaction time of 5 min.

Setup part	Volume V / mL	Residence time t_{res} / min
RSSDR	32.36	2.54
Inlet and outlet	2.05	0.16
Tubing	10.6	0.83
Batch	18.6	1.46

The two batch experiment scenarios were carried out for three different disc speeds of the magnetic stirrer: the lowest was 500 min^{-1}, which was also set fot the experiments with the RSSDR; the other speeds were 1000 min^{-1} and 1400 min^{-1}, of which the latter is the maximum speed of the magnetic stirrer.

5.3.3 Preparation of catalyst-coated rotor disc

TiO_2 (Aeroxide®, *Fisher Scientific International Inc.*) was immobilized on the surface of the rotor in the lower RSSDR gap. For further information on the used TiO_2, the reader

is referred to Tobaldi et al. [141]. A schematic of the preparation of the TiO_2 coated rotor disc is displayed in Figure 5.4.

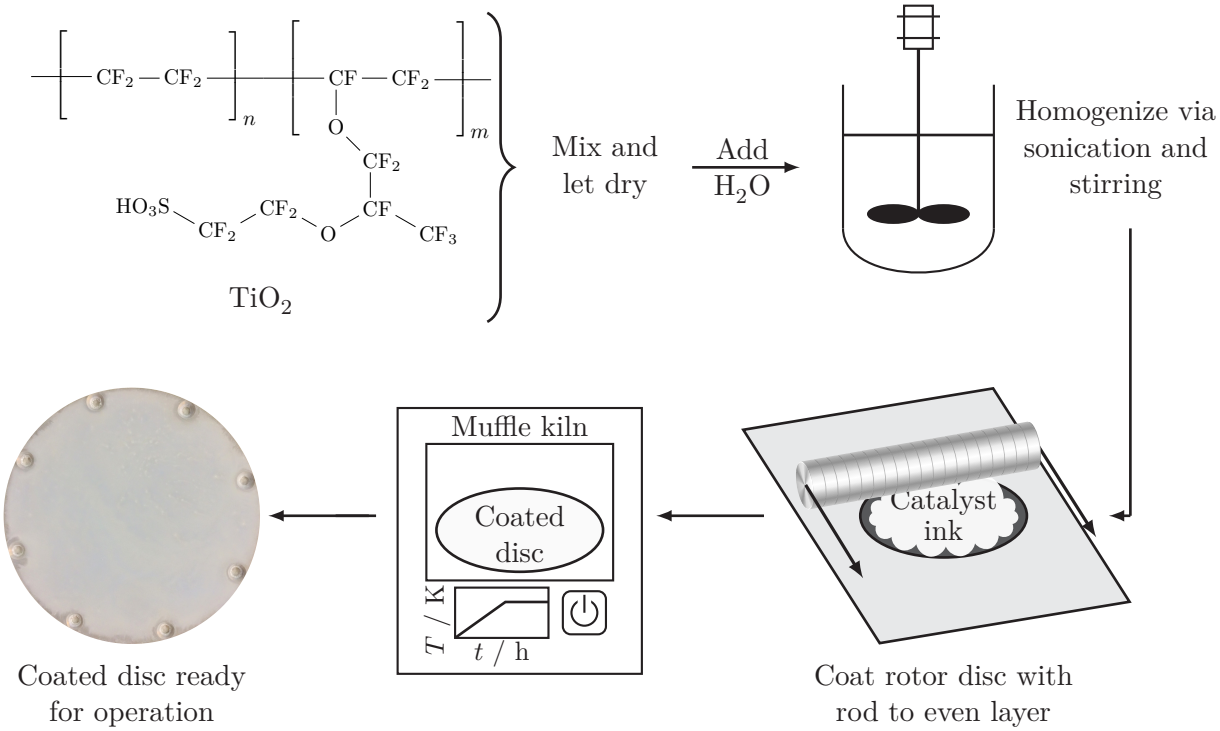

Figure 5.4: Schematic of the preparation of the TiO_2 coated rotor disc.

An ink consisting of bi-distilled water, TiO_2 and Nafion® solution (Nafion® perfluorinated resin solution, 5 wt.-%, *Sigma-Aldrich*) was created by first adding a desired amount of Nafion® solution to the TiO_2 powder and let it dry over night, as was done by Park and Choi [139]. Water was added to gain a TiO_2/H_2O ratio of 3/17, which was found to work best to create catalyst layers that would not break open. The mixture was sonicated for 10 min and stirred at 1400 min^{-1} with a magnetic stirrer for at least 1 h afterwards. 2 mL of the well dispersed ink were evenly spread on the rotor disc with a rod to create a film of 24 µm thickness and let dry before tempering the dried disc at 100 °C for 1 h to remove water and alcohol residues. The resulting TiO_2 and Nafion® amount on the coated and dried disc are: $m_{TiO_2} = 49.65$ mg and $m_{Nf} = 13.48$ mg.

5.3.4 Analysis

For analysis of the oil phase of the epoxidized product mixtures, a gas chromatograph (GC-2014 from *Shimadzu*) with a thermal conductivity sensor (TCD-2014), an autosampler (AOC-20i) and helium (5.0 purity, *Westfalen AG*) was used. A FAMEWAX column from *Restek* with a length of 30 m, an inner diameter of 0.53 mm and a film thickness of 0.5 µm was used as analysis column and an untreated fused silica column with same dimensions as

reference column (*Restek*). The GC analysis allowed the determination of the concentrations c_i of the different components of the educt and product for calculation of conversion X_{MO} (Equation (5.1)), yield Y_{EMO} (Equation (5.2)) and selectivity S_{EMO} (Equation (5.3)) of the epoxidation reaction. Therefore, the GC was calibrated (calibration data is given in Appendix A.3.2) with pure reference substances of the materials of interest (MO from *Sigma-Aldrich*, EMO from *BIOZOL Diagnostica Vertrieb GmbH*).

$$X_{\mathrm{MO}} = \frac{c_{\mathrm{MO},0} - c_{\mathrm{MO}}}{c_{\mathrm{MO},0}} \tag{5.1}$$

$$Y_{\mathrm{EMO}} = \frac{c_{\mathrm{EMO}} - c_{\mathrm{EMO},0}}{c_{\mathrm{MO},0}} = \frac{c_{\mathrm{EMO}}}{c_{\mathrm{MO},0}}\,, \quad \text{with } c_{\mathrm{EMO},0} = 0 \tag{5.2}$$

$$S_{\mathrm{EMO}} = \frac{c_{\mathrm{EMO}} - c_{\mathrm{EMO},0}}{c_{\mathrm{MO},0} - c_{\mathrm{MO}}} = \frac{c_{\mathrm{EMO}}}{c_{\mathrm{MO},0} - c_{\mathrm{MO}}}\,, \quad \text{with } c_{\mathrm{EMO},0} = 0\,, \tag{5.3}$$

where the index "0" stands for initial conditions.

The majority of the experiments were carried out in duplicate, some even in triplicate, and each oil phase of an experiment was examined twice with GC analysis. The data points shown in the figures in Section 5.4 are the calculated mean values of the respective repetition experiments and GC analysis and the error bars the average deviation from the respective mean value.

5.4 Results and discussion

Sections 5.4.1 and 5.4.2 are about preliminary findings supporting the results discussed further on starting with Section 5.4.3; the discussion in the former sections is, hence, not as elaborate as in the latter ones dealing with the main results (Sections 5.4.3 to 5.4.8) presented in this study.

5.4.1 Preliminary batch kinetic experiment

Figure 5.5 shows the temporal concentration profiles of MO and EMO of an experiment carried out in the round-bottomed vessel at a temperature of $T = 60\,^{\circ}\mathrm{C}$, a stirrer speed of $n = 1200\,\mathrm{min}^{-1}$ and a hydrogen peroxide flow of $3.12\,\mathrm{mL\,min}^{-1}$, resulting in a total of 2.5 min during which hydrogen peroxide was added to the batch vessel. After the addition of hydrogen peroxide, the reaction was continued for another 27.5 min. As can be seen in Figure 5.5, a linear increase and decrease is observable for the first 800 s for the concentration profiles of EMO and MO, respectively. The absolute slopes decrease

for both concentration profiles towards higher reaction times. Hence, the average rates of MO consumption and EMO production can be regarded as constant for the first 13 min of the reaction (cf. gray area in Figure 5.5). Thus, $\mathrm{d}c_i/\mathrm{d}t$ can be approximated as $\Delta c_i/\Delta t$ for the first 13 min, resulting in:

$$\frac{\mathrm{d}c_{\mathrm{MO}}}{\mathrm{d}t} \approx \frac{\Delta c_{\mathrm{MO}}}{\Delta t} = -1.5184\,\mathrm{mmol\,L^{-1}\,s^{-1}}\,, \tag{5.4}$$

$$\frac{\mathrm{d}c_{\mathrm{EMO}}}{\mathrm{d}t} \approx \frac{\Delta c_{\mathrm{EMO}}}{\Delta t} = 1.2354\,\mathrm{mmol\,L^{-1}\,s^{-1}}\,. \tag{5.5}$$

For the other experiments carried out in this study, a set reaction time of 5 min was chosen and the average rates of epoxide production can, thus, be determined by dividing the produced amount of EMO by the respective residence time. As indicated by the slopes (Equations (5.4) and (5.5)), MO consumption is a bit higher than EMO formation, suggesting that either side products are formed to a small extent or the formed EMO reacts further in a consecutive reaction.

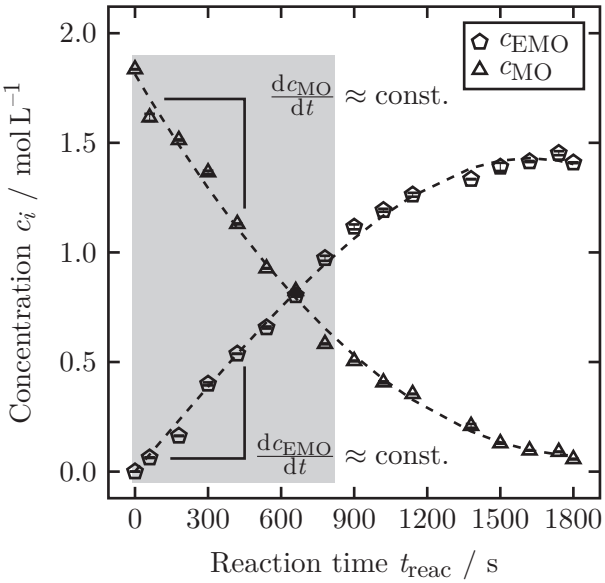

Figure 5.5: Concentration profiles of methyl oleate and epoxidized methyl oleate over time. The experiment was carried out in the round-bottomed vessel at the following operating conditions: $T = 60\,^{\circ}\mathrm{C}, n = 1200\,\mathrm{min^{-1}}$.

5.4.2 Rheological characterization of the studied reaction mixtures

Viscosity measurements of oil phases of different compositions were performed with an *Anton Paar* MCR 302 rheometer at a temperature of 50 °C within a shear rate range of $1500\,\mathrm{s^{-1}}$ and $10\,\mathrm{s^{-1}}$. Figure 5.6 shows the calculated shear stress τ in dependence of shear rate γ for three different EMO mass fractions w_{EMO}. All data sets show the behavior of a

Newtonian fluid, as would be expected [142] and an increase in slope, i.e., viscosity with an increase in EMO mass fraction, which is also in accordance with literature [143].

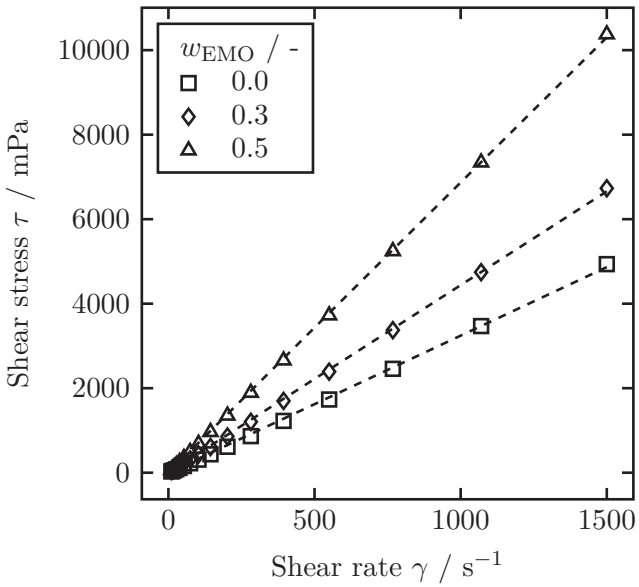

Figure 5.6: Shear stress in dependence of shear rate for three epoxidized methyl oleate mass fractions.

Figure 5.7 displays dynamic viscosity in dependence of EMO mass fraction for three shear rates. A linear increase with a rise in EMO fraction is observable. The fact that two slopes are visible in Figure 5.7 is due to the methyl linoleate content in the mixtures with EMO mass fractions of 0.4 and 0.5 being lower compared to the mixtures with lower EMO content. This is because during the reaction, methyl linoleate, which is present in small quantities in the technical grade educt, also reacts with some of the reactants and it has a lower viscosity than EMO and MO [143, 144].

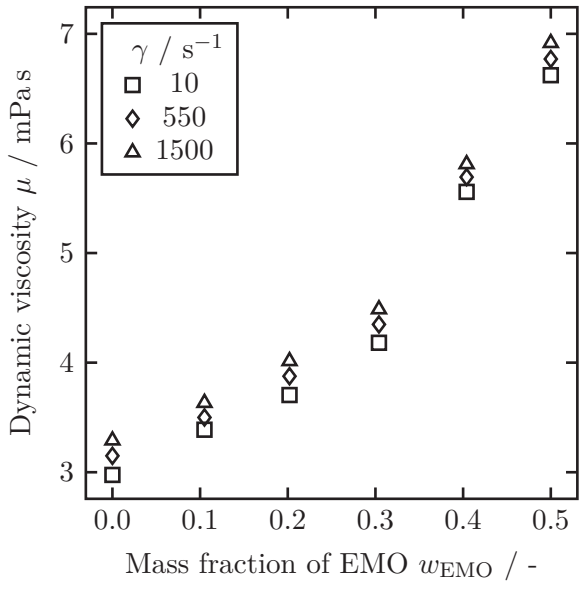

Figure 5.7: Dynamic viscosity in dependence of epoxidized methyl oleate mass fraction for three shear rates.

5.4.3 RSSDR - Effect of temperature

The effect of the reaction temperature on MO conversion, EMO yield and exemplarily selectivity of EMO is given in Figure 5.8. With increasing temperature, conversion and yield rise until maxima are reached at a temperature of about 80 °C, after which both quantities decrease with a further rise in temperature (cf. Figure 5.8).

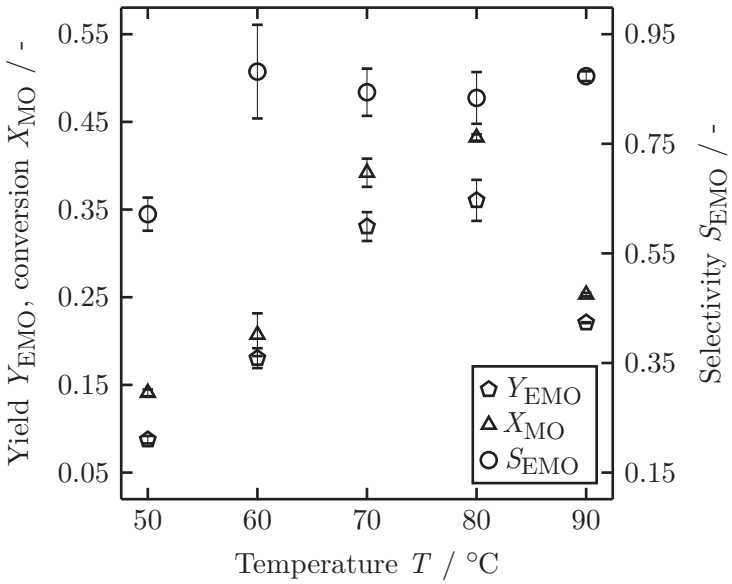

Figure 5.8: Conversion of methyl oleate, yield and selectivity of epoxidized methyl oleate in dependence of temperature for a throughput of $\dot{V}_R = 50\,mL\,min^{-1}$ and a rotational disc speed of $n = 500\,min^{-1}$.

With respect towards selectivity, an increase with a rise in temperature is observed at first up to 60 °C, after which selectivity stays almost at the same level. This behavior suggests that at higher temperatures the decrease in yield and conversion is rather attributed to a decay of hydrogen peroxide at high temperatures than due to side or consecutive reactions, as observed by Phimsen et al. [32] or He et al. [35]. This explanation is supported by the increased observation of bubble formation with higher reaction temperatures. The temperature maximum for EMO yield is close to values found in literature; He et al. [35], e.g., report an optimum reaction temperature of 75 °C for epoxidation of soybean oil in a microflow system, although other references report that the reaction temperature during epoxidation of FAMEs should not exceed 70 °C [88]. This is due to increased epoxy ring opening reactions and the decomposition of peroxyacids at higher temperatures [88]. The observed maximum at 80 °C in this study, despite the high temperature, could be explained given the surplus of formic acid and hydrogen peroxide (molar ratio: $C_{19}H_{36}O_2 : H_2O_2 : HCO_2H = 1 : 4 : 4$). Thus, abundant hydrogen peroxide and formic acid to form performic acid are present, in spite of the hydrogen peroxide decay. The used hydrogen peroxide in this study was stabilized for synthesis by the manufacturer, which is why no further measures were taken to additionally stabilize

hydrogen peroxide by, e.g., ethylenediaminetetraacetic acid (EDTA), as was suggested by Phimsen et al. [32]. In a test experiment, in which 3 vol.-% of a 0.1 M EDTA solution were added to the hydrogen peroxide, no beneficial effect of the EDTA could be seen. The same was observed using a molar ratio of $C_{19}H_{36}O_2 : H_2O_2 : HCO_2H = 1 : 6 : 4$ in order to further compensate the decay of hydrogen peroxide.

5.4.4 RSSDR - Effect of rotational disc speed

The effect of rotational disc speed on yield of EMO and MO conversion was studied for volumetric throughputs of $50\,\mathrm{mL\,min^{-1}}$ and $75\,\mathrm{mL\,min^{-1}}$. The results are depicted in Figure 5.9.

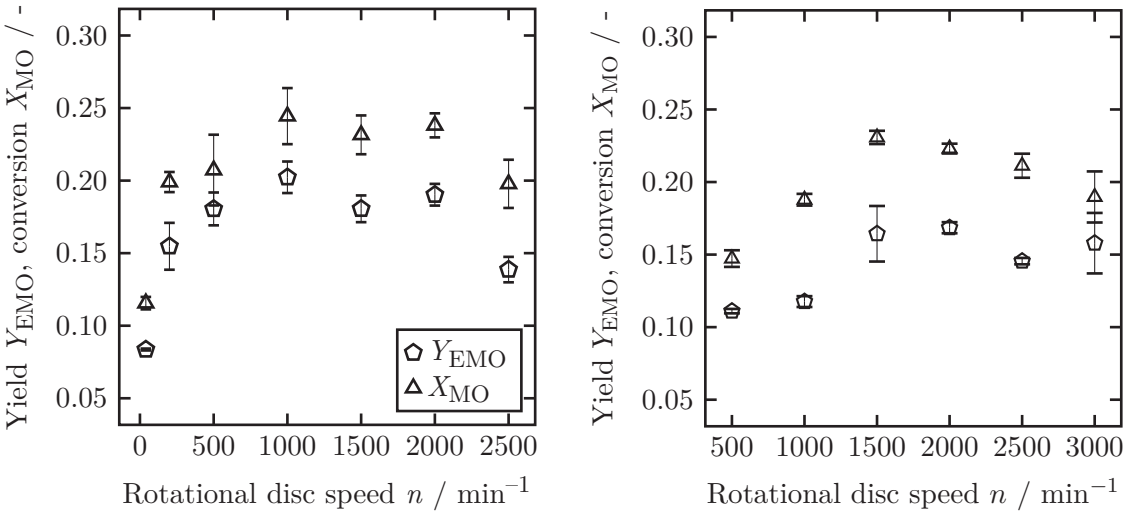

(a) $\dot{V}_R = 50\,\mathrm{mL\,min^{-1}}$. **(b)** $\dot{V}_R = 75\,\mathrm{mL\,min^{-1}}$.

Figure 5.9: Conversion of methyl oleate and yield of epoxidized methyl oleate in dependence of rotational disc speed for two volumetric throughputs at a set temperature of $T = 60\,°C$.

An increase in rotational disc speed causes a rise in MO conversion as well as in EMO yield until maxima are reached at around $1000\,\mathrm{min^{-1}}$ for a throughput of $\dot{V}_R = 50\,\mathrm{mL\,min^{-1}}$ (cf. Figure 5.9a) and $1500\,\mathrm{min^{-1}}$ for $\dot{V}_R = 75\,\mathrm{mL\,min^{-1}}$ (cf. Figure 5.9b). After the respective extrema, yield and conversion decrease with a further increase in rotational disc speed (cf. Figure 5.9). The initial increase with a rise in disc speed is attributed to an improved mass and heat transfer in the reactor gap [22, 26–28, 45]. High angular velocities of the rotor cause high shear forces within the reactor gap, which results in a well dispersed mixture of the water and oil phase [46] providing a large specific surface area for mass exchange as well as faster mass transfer due to a decreased boundary layer thickness at the phase boundary. Furthermore, large rotational disc speeds improve the stator-side heat transfer coefficient in the reactor gap [21, 41, 91, 106], which allows better temperature control of the reaction mixture in the gap; thus, local deviations from

the desired temperature, which would lead to side or consecutive reactions or hydrogen peroxide decay, are avoided and ideal reaction conditions provided for the epoxidation.

The decrease in MO conversion and EMO yield with a further increase in rotational disc speed after the extrema at around $1000\,\mathrm{min}^{-1}$ or $1500\,\mathrm{min}^{-1}$ could be explained by the power input in the reactor gap medium induced by the rotor. The power input in the reactor gap scales to a power of three with angular velocity [65, 91] (cf. Section 2.1.4). The development of the overall dissipative power input due to rotation with increasing rotational disc speed is exemplarily given in Table 5.2. A strong increase in dissipative power input with a rise in rotational disc speed is observed, which could explain the decrease in yield and conversion at higher disc speeds; the potential of the RSSDR to remove heat from the reactor gap through the stator walls to the coolant channels decreases at a certain disc speed because the dissipative power input overrules the improved heat transfer properties, which are brought about by the high degree of turbulence caused by the high angular velocities of the rotor. This becomes obvious when regarding the effectiveness factor η of the RSSDR as a heat exchanger via Equation (5.6) [145].

Table 5.2: Overall dissipative power input due to rotation at different rotational disc speeds for an exemplary reaction mixture; material properties were retrieved from the manufacturers, the VDI Wärmeatlas for formic acid [146] and estimation of the mixture's viscosity [147].

n / min^{-1}	P_{rot} / W
40	0.001
200	0.051
500	0.491
1000	2.771
1500	7.702
2000	15.54
2500	26.44
3000	42.35

$$\eta = \frac{T_{\mathrm{R,in}} - T_{\mathrm{R,out}}}{T_{\mathrm{R,in}} - T_{\mathrm{C,in}}} \tag{5.6}$$

The parameters in Equation (5.6) are the inlet $T_{\mathrm{R,in}}$ and outlet temperature $T_{\mathrm{R,out}}$ of the reactor gap medium, respectively, as well as the inlet temperature of the coolant channels $T_{\mathrm{C,in}}$. The effectiveness factors for rotational disc speeds between $40\,\mathrm{min}^{-1}$ and $3900\,\mathrm{min}^{-1}$ were calculated for dimensionless throughputs C_W (Equation (2.3) in Section 2.1.2) of 100 and 232 and Prandtl numbers Pr (Equation (2.6) in Section 2.1.3) of circa 4, 6.5 and 9.8 based on the experimental data on single-phase stator-side heat transfer in RSSDRs presented in Chapter 3. The results are shown in Figure 5.10; an increase in effectiveness with increasing disc speed is observable up to disc speeds

between $1000\,\mathrm{min}^{-1}$ and $2000\,\mathrm{min}^{-1}$ for the relevant operating conditions, after which the effectiveness decreases with a further rise in disc speed. The volumetric throughputs studied in this chapter correspond approximately to dimensionless throughputs between $C_W = 2.9 - 10.7$ and the Prandtl number of an exemplary reaction mixture values about 10. The material properties for this estimation were retrieved from the manufacturers of the respective chemicals, the VDI Wärmeatlas [146] for formic acid data, the calculation of the viscosity μ of a mixture (Equation (5.7) [147]) as well as from viscosity measurements of the oil phase at different epoxide concentrations (cf. Section 5.4.2). The parameters x_i and μ_i in Equation (5.7) stand for the mole fraction and the viscosity of the component i, respectively.

$$\frac{\mu}{\mathrm{Pa\,s}} = \sum_i x_i \ln \frac{\mu_i}{\mathrm{Pa\,s}} \tag{5.7}$$

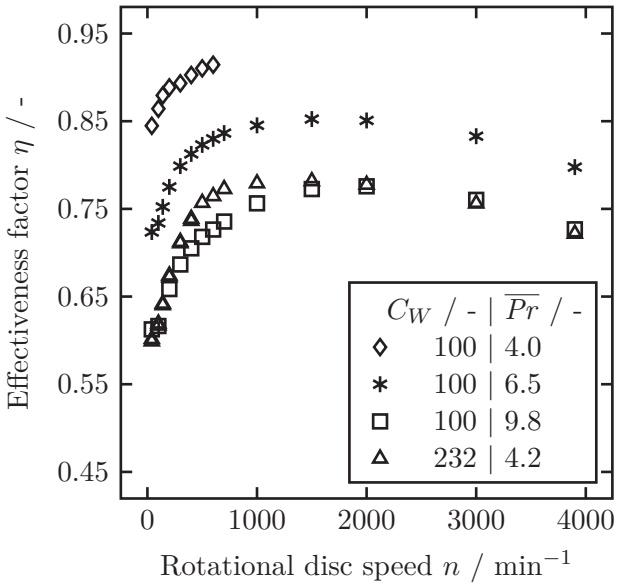

Figure 5.10: Effectiveness of heat exchange properties of the RSSDR in dependence of rotational disc speed for constant dimensionless throughputs C_W and Prandtl numbers Pr based on experiments by Kleiner et al. [91] presented in Chapter 3 on heat transfer properties of the studied RSSDR.

The relevant dimensionless throughputs of this study are of course low in comparison to the throughputs regarded in the heat transfer study in Chapter 3. However, it was not possible to investigate low throughputs as, e.g., $C_W = 10$, since the temperature difference between hot and cold outlet media was already very small at $C_W = 100$ and $Pr \approx 4$, which is why the effectiveness could only be determined up to a disc speed of $600\,\mathrm{min}^{-1}$ at these conditions (cf. Figure 5.10) [91]. Also, the study was performed with deionized water and water/glycerol mixtures, which mix better than the regarded water and oil phases of this study.

Nonetheless, the development of the effectiveness with increasing disc speed (Figure 5.10) serves as a good explanation as to why EMO yield and MO conversion decrease with a rise in disc speed after around a maximum between $1000\,\mathrm{min^{-1}}$ and $1500\,\mathrm{min^{-1}}$; the maxima of yield, conversion and effectiveness in Figures 5.9 and 5.10 are within a range of rotational disc speeds after which the dissipative power input reaches values (cf. Table 5.2) which could lead to noticeable temperature increases of the reactor gap medium; this counteracts the effort of removing the heat release of the reaction (assuming a conversion of about 20 %, the heat release due to the epoxidation reaction during the reaction time of 5 min values around 9 W). Thus, isothermal reaction conditions can no longer be guaranteed. This effect appears to cause the decay of hydrogen peroxide, which is then no longer locally available for the epoxidation reaction, since yield and conversion are decreased. Furthermore, an increased bubble formation was observable during the experiments the higher the rotational disc speed. The results at higher disc speeds (above $2000\,\mathrm{min^{-1}}$) should consequently be considered carefully, since the set temperature, which poses no difficulty to be maintained at lower rotational disc speeds, can no longer be guaranteed and a direct comparison between high and low rotational disc speeds should be done carefully. Nevertheless, the results in Figure 5.9 show the possibility to intensify the epoxidation reaction in an RSSDR, but only to a certain extent. It also becomes obvious that the used RSSDR in its current configuration is limited due to the dissipative power input, which needs to be considered at higher rotational disc speeds, as was also observed in different studies on RSSDRs in literature [9, 41]. The development of the effectiveness in Figure 5.10 further shows that after a rotational disc speed of about $400\,\mathrm{min^{-1}}$ the slope of the effectiveness in dependence of disc speed is quite low compared to at very small disc speeds; hence, the intensification of the epoxidation shown in Figure 5.9 can rather be attributed to the enhanced mixing and mass transfer caused by the high degree of turbulence due to rotation.

The observation that the maximum with respect towards EMO yield and MO conversion is shifted a little towards higher disc speeds with increasing throughput (cf. Figures 5.9a and 5.9b) further indicates the aforementioned argument, as a higher throughput correlates with a smaller residence time in the RSSDR per cycle, allowing less time for the reaction mixture to be heated by the dissipative power input causing the decay of hydrogen peroxide. However, taking into account the small differences in yield and conversion around disc speeds between $1000\,\mathrm{min^{-1}}$ and $2000\,\mathrm{min^{-1}}$ for a throughput of $50\,\mathrm{mL\,min^{-1}}$ (cf. Figure 5.9a), it is rather difficult to say with certainty that the extremum for said throughput is at a disc speed of $1000\,\mathrm{min^{-1}}$ and not in between $1000\,\mathrm{min^{-1}}$ and $1500\,\mathrm{min^{-1}}$. In any case, qualitatively speaking, a maximum with respect towards yield and conversion coinciding with a maximum of the heat exchange effectiveness is observable.

5.4.5 RSSDR - Effect of throughput

The influence of the volumetric throughput of the recycle loop on EMO yield and MO conversion is demonstrated in Figure 5.11. The experiments were carried out at a rotational disc speed of $1000\,\mathrm{min}^{-1}$ in order to guarantee sufficient homogenization in the batch vessel below the RSSDR and as a consequence thereof transport of both phases from the batch vessel to the RSSDR, even for the lowest regarded throughput.

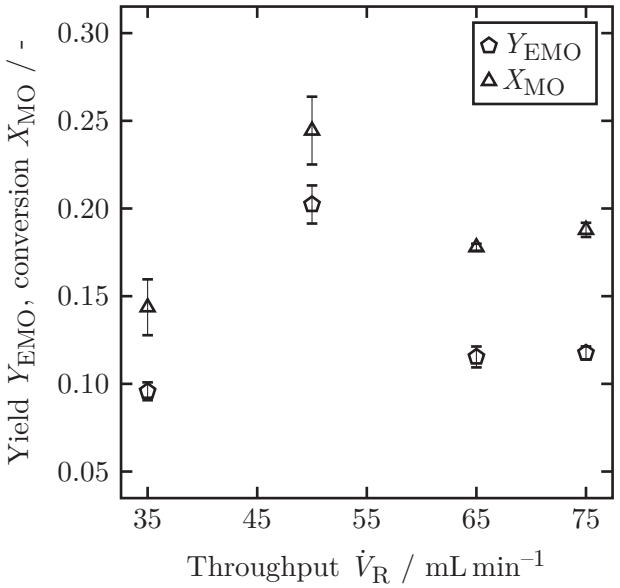

Figure 5.11: Conversion of methyl oleate and yield of epoxidized methyl oleate in dependence of throughput for a temperature of $T = 60\,°\mathrm{C}$ and a rotational disc speed of $n = 1000\,\mathrm{min}^{-1}$.

An increase in EMO yield and MO conversion was observed when increasing the throughput from $35\,\mathrm{mL\,min}^{-1}$ to $50\,\mathrm{mL\,min}^{-1}$, after which a further increase in throughput results in a decrease in EMO yield and MO conversion (cf. Figure 5.11). This behavior could be explained considering that the reduced residence time per recycle loop is too low at $65\,\mathrm{mL\,min}^{-1}$ and $75\,\mathrm{mL\,min}^{-1}$ to gain yields and conversions as high as at $50\,\mathrm{mL\,min}^{-1}$, which appears to be the optimum throughput for the regarded operating conditions in the semi-batch operated setup with recycle.

The influence of throughput variation on the flow conditions in the RSSDR is considered to be negligible at a disc speed of $1000\,\mathrm{min}^{-1}$ for the regarded throughputs; this is because the transition radii (Equation (2.4) [31] in Section 2.1.2), indicating the transition between plug flow (low radial positions) and ideally stirred region (large radial positions) in the reactor gap, for the regarded parameter range are $r_{\mathrm{trans}} \leq 0.46\,r_{\mathrm{r,o}}$ for all measurements, meaning that the majority of the reactor gap is always rotation-governed.

At lower throughputs, the residence time per cycle in the peripheral tubing is longer and both water and oil phase demix stronger compared to conditions at higher throughputs.

In a similar way, at very low throughputs, the phases in the batch vessel demix more than at higher throughputs even though it was made sure that both phases in the vessel were sufficiently mixed for a transport of both phases through the tubes and the RSSDR. A separate consideration of the throughput effect on the interior of the RSSDR, the peripheral tubing and the batch vessel is not possible with the current methodology and should, therefore, be examined in a further study with continuous operational mode. As the investigation of volumetric throughput as an influencing parameter on the epoxidation of FAMEs in an RSSDR was merely a side interest and circumstantially investigated in order to find the optimum throughput for the recycle flow of the applied semi-batch operational mode with recycle, a detailed investigation and discussion given the explained circumstances is not possible at this point and should be pursued in a further study.

5.4.6 RSSDR - Effect of a titanium dioxide coated rotor disc

After the parameter study without any heterogeneous catalyst, test experiments with a TiO_2 coated rotor disc (lower reactor gap only) were carried out for a throughput of $\dot{V}_R = 50\,mL\,min^{-1}$, a temperature of 60 °C and different rotational disc speeds. The results of conversion, yield and selectivity of these experiments are compared to the results from experiments at same reaction conditions without a TiO_2 coated disc (Figure 5.12). Figure 5.12a reveals that MO conversion is about the same for the experiments with and without a coated rotor disc. This means that the TiO_2 does not fulfill its purpose under the investigated reaction conditions. It does not catalyze the examined epoxidation reaction, but neither any other reaction of the educt, otherwise conversion would have to be higher compared to the experiments with a plain steel rotor. However, EMO yield and selectivity are slightly decreased for the experiments with a coated rotor disc, thus, another product must be favored as opposed to the experiments with a plain rotor. It can also be noticed that the carbon balance could not be closed within the frame of measurement uncertainty. This suggests the formation of products, which are not detectable with the current analysis method, as the retention times of these products are likely to be prolonged compared to, e.g., EMO. Since the current analysis times are already very long and easy quantification of other species would be difficult, no further measures were taken to investigate this reaction pathway, as the scope of the experiments with a TiO_2 coated rotor was to find out, if the application of this catalyst would further enhance the epoxidation's progression.

The results given in Figure 5.12 could imply that the chosen catalyst, though reported to be suitable in literature [32], is not beneficial under the applied conditions and the bulk reaction, intensified by the advantageous mass transfer properties of the RSSDR, is already very fast. As the TiO_2 layer on the rotor has to endure strong shear forces, quite a high Nafion® to TiO_2 ratio ($m_{Nf}/m_{TiO_2} = 0.27$) had to be used for the catalyst ink.

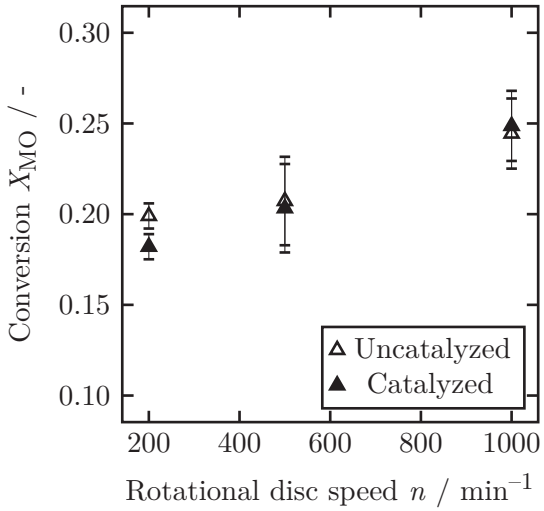

(a) Conversion of MO.

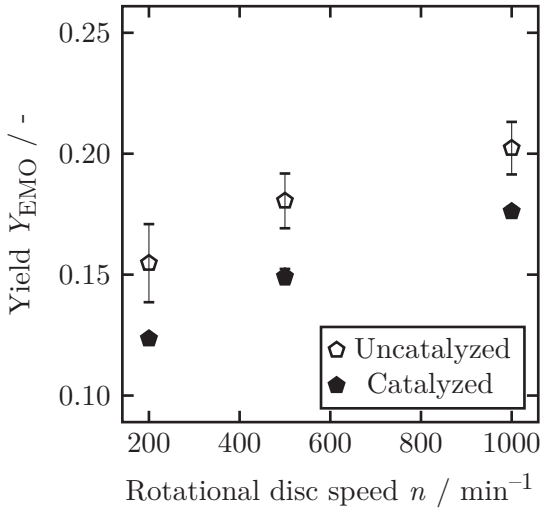

(b) Yield of EMO.

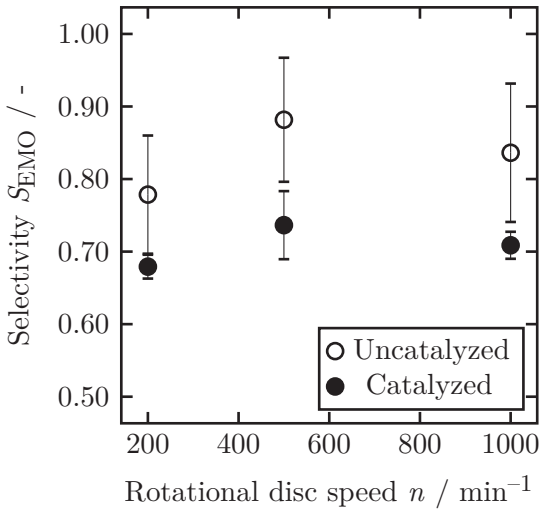

(c) Selectivity of EMO.

Figure 5.12: Conversion of methyl oleate, yield and selectivity of epoxidized methyl oleate in dependence of rotational disc speed from experiments with and without a TiO_2 coated rotor disc. The used Nafion®/TiO_2 and TiO_2/H_2O ratio value 0.27 and 3/17, respectively.

Since the experiments with and without a TiO_2 coated rotor disc do not result in same yields and selectivities, it can be concluded that despite the high Nafion® amount the TiO_2 was still accessible for the reaction mixture and that the results in Figure 5.12 are not due to bad TiO_2 accessibility. Instead, the Nafion® may modify the surface charge of the coated rotor disc [139] in a way that a different reaction was slightly favored compared to the experiments with a plain steel rotor. As Phimsen et al. [32] report on positive effects of TiO_2 as catalyst for the same reaction system with similar reaction conditions, except for the reactor system, it can be assumed that the addition of Nafion® leads to the results of a slightly decreased yield and selectivity of the desired product. Unfortunately, it is not possible to coat the rotor disc with only a plain layer

of TiO_2 particles, as it would be sheared off due to the high rotational disc speeds. However, regarding the intensifying properties of the RSSDR with respect to the studied reaction by comparing the experiments with the RSSDR without TiO_2 coated disc with batch experiments at similar reaction conditions and calculating average rates of epoxide production, it becomes obvious that with the current RSSDR setup there is no need to catalyze the reaction further. The latter is because the epoxidation of MO carried out in an RSSDR is already strongly intensified without an additional heterogeneous catalyst. Also, any reactor system being immobilized on the rotor disc would probably be sheared off at a certain point of time, as Phimsen et al. [32] reported that the catalyst (TiO_2) was peeled off after around 3 h of operation at microflow conditions, which are by extension less turbulent compared to conditions in the rotor-stator gap at moderate to high disc speeds. Hence, any attempt similar to the one applied in this work to immobilize a catalyst on the rotor disc seems obsolete.

5.4.7 Comparison of different reactor setups

As stated before, to assess the RSSDR's performance, comparative experiments with a simple batch reaction vessel with and without the recycle were performed. The most suitable benchmark are the batch experiments with recycle carried out in the round-bottomed reaction vessel, which was placed under the RSSDR during the experiments for the latter reactor system. Assuming that hardly any reaction takes place in the tubes connecting the different reactor system parts, the direct intensification of the epoxidation reaction can be determined. The results of the batch experiments with recycle in comparison to the RSSDR experiments at same operating conditions (detailed experimental conditions are given in Table 5.3) are given in Figure 5.13.

A slight increase in EMO yield and MO conversion with an increase in disc speed of the magnetic stirrer was observed for the BWR configuration, but the results are very low in comparison to the RSSDR experiments (cf. Figure 5.13). Regarding the highest values of yield and conversion for the two reactor systems, respectively, the achieved yield with the RSSDR is by a factor of 6.8 larger compared to the BWR system; maximum conversion reached with the RSSDR is 2.9 times the conversion at same conditions in the batch vessel. In this calculation the amount of yield and conversion resulting from the reaction taking place in the round-bottomed vessel at a stirrer speed of 500 min^{-1} is of course subtracted from the respective values yielded in the RSSDR.

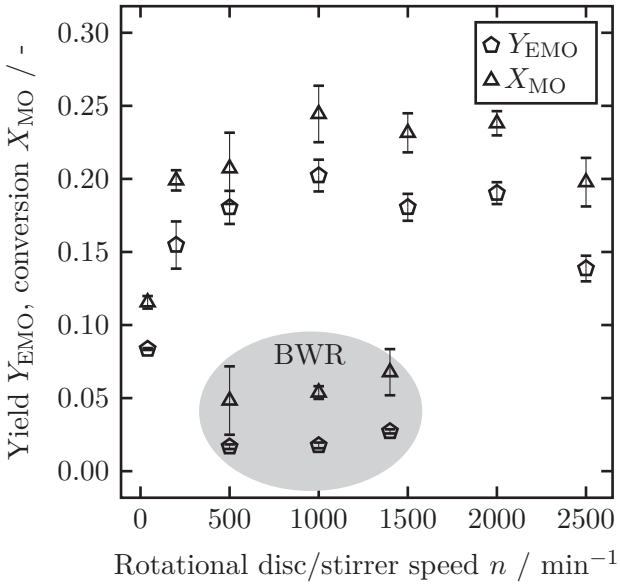

Figure 5.13: Conversion of methyl oleate and yield of epoxidized methyl oleate in dependence of rotational disc speed at a throughput of $\dot{V}_R = 50\,mL\,min^{-1}$ and a temperature of $T = 60\,°C$ from RSSDR experiments and comparative batch with recycle (BWR) experiments.

Table 5.3: Reaction conditions of the comparative experiments with the different reactor setups. All experiments were carried out at a temperature of $T = 60\,°C$ and a reaction time of $t_{reac} = 5\,min$. The best conditions of the comparative experiments were always chosen for comparison, e.g., the batch experiments at the highest rotor speed causing the best homogenization of the oil and water phase.

Reactor type	Disc/stirrer speed n / min^{-1}	Throughput $\dot{V}_R$ / mL min^{-1}	Residence time* t_{res} / min	Volume V / mL
RSSDR	1000	50	2.54	63.6
RSSDR/TiO_2	1000	50	2.54	63.6
Batch	1400	0	5**	18.6
BWR	1400	50	1.46	63.6

*Residence time in this context means the total time the mixture is in the reactor of interest.
**The residence time for the batch reactor equals the reaction time.

Obviously, the reaction mixture prevails a little longer in the RSSDR than in the batch vessel under these operating conditions (cf. Table 5.1), which is why a comparison of the different reaction rates is even more suitable for an assessment of the different reactor performances. The respective average reaction rates of epoxide production (Equation (5.8)) are calculated by dividing the produced amount of EMO by the time the reaction mixture prevailed in the respective reactor system (cf. Table 5.3). The rates from the experiments with the RSSDR are reduced by the rate being attributed to the reaction taking place in the round-bottomed vessel at same reaction conditions. The average reaction rates can be determined as described above, as a simple kinetic experiment performed with the round-bottomed vessel, no throughput and high stirrer speed showed that the reaction

rates of MO consumption and EMO production stayed constant for the first 13 min during the experiment with an overall reaction time of 30 min (cf. Section 5.4.1). To account for the enhanced mass transfer in the RSSDR as compared to the batch reactor and the fact that about half the reaction/residence time in the RSSDR is needed to produce similar amounts of EMO as in the batch reactor, this way of determining the rates was only applied for reaction times up to 5 min for the RSSDR. The resulting average epoxide production rates at the respective best mixing conditions are given in Figure 5.14.

$$r_{\mathrm{EMO}} = \frac{\mathrm{d}c_{\mathrm{EMO}}}{\mathrm{d}t} \approx \frac{\Delta c_{\mathrm{EMO}}}{\Delta t} = \frac{c_{\mathrm{EMO}} - c_{\mathrm{EMO},0}}{t_{\mathrm{res}}} = \frac{c_{\mathrm{EMO}}}{t_{\mathrm{res}}} \quad \forall \quad t_{\mathrm{reac}} \leq 5\,\mathrm{min} \tag{5.8}$$

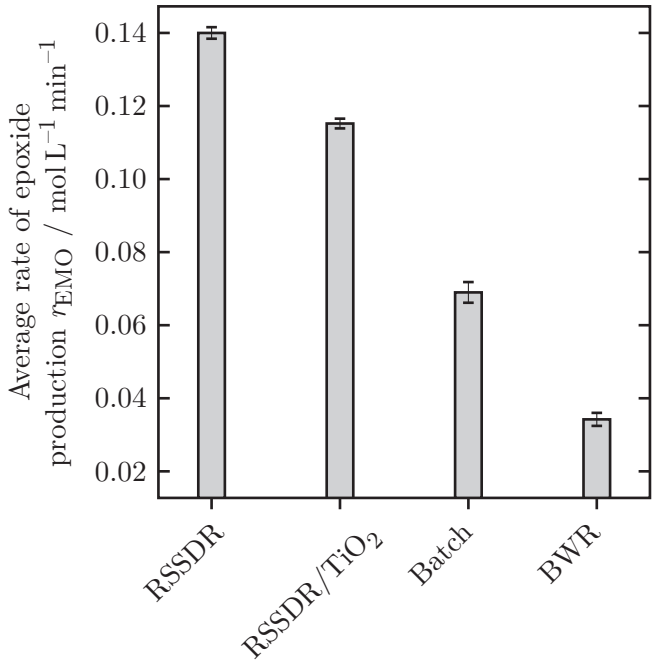

Figure 5.14: Average rates of epoxidized methyl oleate production for the different setups. The rates for the catalyzed and uncatalyzed RSSDR were calculated from experiments at the reaction conditions given in Table 5.3.

As can be seen in Figure 5.14, the average rate of epoxide production is the highest for the RSSDR at about 0.14 mol L^{-1} min^{-1}, followed by the RSSDR with TiO_2 coated rotor disc, the batch reactor without recycle and last the batch experiment with recycle at around 0.034 mol L^{-1} min^{-1}. The latter is about a factor four lower compared to the average epoxide production of the RSSDR, showing that the RSSDR strongly increases the epoxidation of MO in comparison to the studied batch reactor setup. It should also be noted that the reference batch experiments were carried out under ideal mixing conditions as opposed to other batch experiments with, e.g., an overhead stirrer [32]. A similar experiment, in which an overhead propeller stirrer at high disc speeds was used, was also performed in this study. However, this mixing device did not allow sufficient mixing of

the oil and water phase to create a well homogenized dispersion, which of course led to long reaction times to achieve comparable conversions and which would, therefore, be no suitable benchmark to compare the RSSDR to.

5.4.8 Comparison to other reactor types

In a comparison to other reactors found in literature used for epoxidation of FAMEs, the results of this study show that the RSSDR runs well within and/or outperforms average epoxidation rates yielded with microreactors. Torrente-Murciano et al. [129] observed double bond epoxidation rates of about 3.8 mmol L^{-1} min^{-1} at a conversion of around 0.05 in a microtubular recycle reactor at a temperature of 60 °C and a residence time of 10.6 min in the epoxidation of sunflower oil with hydrogen peroxide using a homogeneous tungsten-based catalyst. However, they calculated the reaction rates by multiplying the reaction rate as calculated in this study by the ratio of the volume of the oil phase and the reactor volume. As the volume of the RSSDR is circa the same as the used volume of the oil phase, a quantitative comparison of this work with their results is still possible. The reaction rate reported by Torrente-Murciano et al. [129] is still quite low compared to the results achieved in a batch reactor in the epoxidation of MO with hydrogen peroxide and formic acid at a temperature of 60 °C and a molar ratio of $C_{19}H_{36}O_2 : H_2O_2 : HCO_2H = 1 : 4 : 4$ by Phimsen et al. [32]. They report reaction rates, which were calculated based on either the volume of the used microreactor or the used reactant volume in case a batch reactor was used, of 0.006 mol L^{-1} min^{-1} at a reaction time of 15 min for the batch reactor and a highest rate of 0.14 mol L^{-1} min^{-1} for a residence time of 2.7 min, a conversion of 0.47 and an oxirane yield of 0.43 achieved in their TiO_2 coated capillary microreactor [32]. The latter reactor achieves about the same rate as observed in this study. Unfortunately, Phimsen et al. [32] do not state, which isomers of the methyl oleate educt and the epoxidized product they regarded. Similar as in this study, they used an educt of technical grade purity. In the educt used in this study, slight amounts of the *trans* isomer of methyl oleate besides the *cis* isomer were present. The presence of the *trans* isomer was observed when examining the used educt test-wise with a GC-MS system (7890B GC system with an FID, an autosampler unit and a DB-5 column and a 5977A MSD system from *Agilent Technologies*), as no pure reference substance of the *trans* isomer could be supplied. For the *cis* isomer, the reference substance could be supplied, allowing to calibrate the used GC system for quantification and clear assignment of the substance. The same problem applied for the epoxidized product. Since the *cis*-9,10-epoxystearic acid methyl ester was purchasable and it was the main product, it made sense, to concentrate on the *cis* educt and the more likely product, respectively. However, assuming that the response factors for the different isomers are about the same regarding *cis* and *trans* isomers, the achieved reaction rates of this study are even a little higher compared to Phimsen et al. [32]. The average epoxide production rate for the RSSDR at the operating conditions

given in Table 5.3 values 0.16 mol L^{-1} min^{-1}, which is about 15 % higher compared to the case in which only the *cis* isomers were regarded. Qualitatively speaking, the results of this study whether *cis* and *trans* or only the *cis* molecules are considered yield the same results; Figure 5.8 is exemplarily supplied in the Appendix A.3.1 again with consideration of *cis* and *trans* isomers.

5.5 Conclusion

The intensification of the epoxidation of MO with hydrogen peroxide and formic acid in an RSSDR in a recycle operational mode was investigated in dependence of temperature, rotational disc speed, throughput and TiO_2 as a heterogeneous catalyst. Local extrema of conversion and yield were observed with respect towards temperature, rotational disc speed and throughput, with the respective extremum conditions being 80 °C, 1000 min^{-1} and 50 mL min^{-1}. The use of TiO_2 as a heterogeneous catalyst immobilized on the rotor disc using Nafion® yielded similar conversions compared to experiments at same conditions with a plain steel plate as rotor. However, selectivity and yield were decreased in the experiments with the coated rotor disc. Therefore, and due to the fact that any type of catalyst layer immobilized on the rotor in a similar way as in this study will most likely be sheared off after a certain amount of time during longer operation times, it can be suggested that the RSSDR itself could be used without any further usage of heterogeneous catalysts. This is because it already intensifies the epoxidation significantly and, in addition, it is advantageous that no application of a further catalyst, besides the acid catalyst, is necessary, as it facilitates operation, since it does not have to be dealt with deactivation or catalyst loss, etc., and it is less cost-intensive. In comparison to batch experiments carried out as a benchmark in this study, the RSSDR considerably outperforms the batch experiments; the average rate of epoxide production is by a factor of four higher compared to the most suitable batch comparative experiment and values about 0.14 mol L^{-1} min^{-1}. This value matches reaction rates found in literature for the same reaction, but carried out in a heterogeneously catalyzed microreactor [32]. Thus, it can be concluded that the RSSDR due to its beneficial mass and heat transfer properties allows a distinct intensification of the epoxidation of MO in contrast to batch and even some microreactors found in literature. However, due to performance issues of the experiments, a semi-batch operational mode with recycle through the RSSDR was used to carry out the parameter study. As the RSSDR is designed to perform as a continuous reactor, which makes it also attractive for industrial processes, the operational procedure of the experiments of this study should be changed towards a continuous mode with a split recycle stream for any application outside the laboratory.

6 Summary and outlook

In this thesis, the characteristics of a rotor-stator spinning disc reactor (RSSDR) in terms of hydrodynamics and reaction engineering were investigated. To do so, an existing RSSDR setup was further developed to allow temperature control of the reactor gap and examination of the heat transfer properties of said setup. As the studied RSSDR is a complex reactor type with small dimensions, which does not allow to easily measure locally resolved temperature distributions, a computational fluid dynamics approach was also pursued to regard the flow and heat transfer properties of the RSSDR setup. An example reaction, i.e., Prilezhaev epoxidation of methyl oleate (MO), which is very exothermic and needs excellent mixing and mass transfer properties, was carried out in the RSSDR to demonstrate the process-intensifying potential of the RSSDR for heat and mass transfer limited reaction systems.

In Chapter 3, the single-phase stator-side heat transfer of an RSSDR was investigated in dependence of dimensionless throughput, Prandtl number, rotational Reynolds number and aspect ratio. Two stator housings, allowing the examination of two different aspect ratios, made of an aluminum alloy were designed in order to provide good temperature control of the reactor gap by introducing coolant channels and reducing the thermal resistance of the stator housing. The experiments were evaluated by the use of the prevailing reactor model for RSSDRs as a base for a simple reactor modeling. Besides the accurate measurement of all inlet and outlet temperatures, volumetric throughputs and pressure drop, the correct determination of heat loss to the environment and especially the correct consideration of the dissipative power input due to rotation posed a challenge in this study.

An increase in Nusselt number with an increase in either one of the regarded parameters was observed. With respect to the rotational Reynolds number, laminar and turbulent flow regimes could be identified, which coincide with a throughput- and a rotation-governed heat transfer regime. The critical Reynolds numbers value about 10^5 and 10^6 for the small and large setup, respectively. A Nusselt number correlation for the turbulent regime was established in dependence of the aspect ratio, dimensionless throughput, rotational Reynolds number and Prandtl number, describing the experimental data within 20 % accuracy. A maximum stator-side Nusselt number of 1346 was achieved at a rotational Reynolds number of $Re_\Omega = 4.2 \cdot 10^5$, a dimensionless throughput of $C_W = 232$, a Prandtl number of $Pr = 13$ for the smaller setup with an aspect ratio of $G =$

0.0154. A distinct intensification of the heat transfer properties by means of high disc speeds of the rotor and therewith a high degree of turbulence in the reactor gap was observed, increasing the overall volumetric heat transfer coefficient from $1.27\,\mathrm{MW\,m^{-3}\,K^{-1}}$ to $2.16\,\mathrm{MW\,m^{-3}\,K^{-1}}$ for a rise in rotational Reynolds number from $Re_\Omega = 2.71 \cdot 10^4$ to $4.25 \cdot 10^5$. In comparison to another RSSDR, the setup investigated in this work allows overall volumetric heat transfer coefficients, which are twice as high and considerably larger compared to conventional tube reactors. This study also revealed that a variation of the aspect ratio, which was realized by a variation in radius in this work, yields different results compared to a variation in gap height. This should be considered in future studies and maybe further investigated by a variation of the aspect ratio via changing the radius and the gap height in one comprehensive study.

An optimization of the reactor setup geometry should also be considered with the aim of reducing the thermal resistances in the stator housing and coolant channels and increasing the heat exchange area in order to be able to also use the setup at very high rotational disc speeds and still retain a good temperature control. As this would probably be difficult to be performed experimentally, a numerical approach should be pursued as was done in Chapter 4 of this work.

In Chapter 4, a computational fluid dynamics study of the flow and heat transfer properties of an RSSDR using the open-source software OpenFOAM® is presented. Due to the complex turbulent flow in a rotor-stator gap, in a first step, it was essential to find an appropriate turbulence model. A Reynolds-averaged Navier−Stokes (RANS) approach was pursued in order to keep computation times low. Also, rotational symmetry was assumed and the three-dimensional setup simplified as a two-dimensional axisymmetric (2.5D) model geometry. By means of simulating different rotor-stator geometries found in literature, for which experimental data for pressure drop and velocity profiles exist, a turbulence model study was performed to identify the *Lien-Leschziner* turbulence model, a two equation $k-\varepsilon$ model, as the one representing the literature data best. This model was then used in the flow simulation of the studied RSSDR model geometry using the *simpleFoam* solver from OpenFOAM® at different rotational disc speeds and dimensionless throughputs. The retrieved radial velocity profiles from the simulations show torsional-Couette behavior for the majority of the radial gap and simulated rotational disc speeds; the tangential velocity profiles resemble a Stewartson type flow at low rotational disc speeds and radial positions, which changes towards a torsional-Couette flow as the radial position or disc speed increases.

The cold-flow simulations were used for simulating the conjugate heat transfer of the RSSDR model using a modified *chtMultiRegionSimpleFoam* solver from OpenFOAM®. The modified solver considers dissipative power inputs, which is relevant for higher rotational disc speeds when regarding RSSDRs. Thus, radially resolved temperature distributions and heat transfer coefficients could be determined, which are not easily

accessible experimentally. The simulated temperature profiles qualitatively agree with literature results and show a similar profile as the tangential velocity component in the torsional-Couette regime. The axial temperature profiles are generally steep, which is pronounced more strongly at higher radial positions and rotational disc speeds, with boundary layers present at the rotor and stator side, which decrease with increasing disc speed and throughput. Local stator-side heat transfer coefficients were calculated from the temperature fields, which increase with increasing rotational disc speed and throughput, where the throughput influence ceases at higher radial positions. In order to validate the numerical results, area-averaged stator-side heat transfer coefficients for the entire reactor gap were determined and compared to the results presented in Chapter 3, which shows good agreement. The results in Chapter 4 demonstrate the possibility to simulate hydrodynamics and heat transfer of the studied RSSDR of this work as a 2.5D geometry using the open-source software OpenFOAM® and a RANS approach for turbulence modeling. Expensive measurements can, thus, be avoided and the variety of parameters and parameter ranges can easily be extended.

However, only a small parameter space was studied as a proof of principle and because experimental data for validation was available. This parameter space should be extended and a comprehensive study of different flow conditions by a variation of rotational Reynolds number, dimensionless throughput and aspect ratio should be performed. Thus, the existing flow map for rotor-stator cavities, which only characterizes the flow in dependence of aspect ratio and rotational Reynolds number, can be improved and developed towards a three-dimensional map of the flow in a rotor-stator cavity showing the dependences of aspect ratio, rotational Reynolds number and dimensionless throughput. To do so, further turbulence model studies should be performed, since not every turbulence model describes the turbulent flow accurately enough across a large range of the rotational Reynolds number; a Reynolds stress model or the transition to a large eddy simulation approach could even be considered in order to further improve accuracy when developing a new flow map. Simulating the flow at various operating conditions, these flow fields can also be used for simulating the residence time behavior at a variety of different conditions by means of a transient tracer simulation. Thus, the prevailing reactor model for the RSSDR could be improved in terms of extending the parameter range and maybe finding an improved correlation for the transition radius, which does not allow theoretical transition radius values larger than the actual radius of an RSSDR setup.

With regard to the simulation of the heat transfer, constant material properties were assumed in a first attempt, which of course introduces errors, but keeps computation times low and is justifiable for low to moderate temperature changes. However, if more accurate results are needed when simulating, e.g., an industrial application in an RSSDR setup, temperature dependence of the material properties should be included in the computations and a simultaneous solution of flow and enthalpy favored.

After characterization of the heat transfer in an RSSDR in Chapters 3 and 4 in this thesis and investigation of the mixing as well as mass transfer properties in an earlier thesis at the Chair I of Technical Chemistry at the Technical University of Munich, the observed beneficial heat and mass transfer properties of the RSSDR were tested by intensifying the epoxidation of a fatty acid methyl ester (FAME). The epoxidation of MO with hydrogen peroxide as oxygen donor and formic acid as oxygen carrier is very exothermic and two immiscible fluids must be mixed; hence, excellent mixing and mass transfer is needed. Good temperature control is further necessary due to the exothermicity of the epoxidation reaction and because concentrated hydrogen peroxide is involved, which decomposes under strong heat release at higher temperatures. These aspects make the RSSDR an ideal candidate for the execution of this epoxidation reaction, which is why in Chapter 5 the intensification of the epoxidation of MO in an RSSDR carried out in a semi-batch operational mode with recycle in dependence of rotational disc speed, temperature and volumetric throughput with and without a catalyst-coated rotor disc was examined.

A stator setup made of stainless steel being resistant to the aggressive media of this study was first designed in analogy to the aluminum stator housings with integrated coolant channels of Chapter 3. For all three investigated parameters, optimum values with respect towards epoxide yield and MO conversion were observed, with the optimum conditions for the studied experiments being at a rotational disc speed of $1000\,\mathrm{min^{-1}}$, a temperature of 80 °C and a throughput of $50\,\mathrm{mL\,min^{-1}}$. Applying TiO_2 as a heterogeneous catalyst immobilized with Nafion® on the lower part of the rotor disc revealed no beneficial results; similar conversions were achieved with and without the coated rotor disc, but selectivities and yields of the epoxide were decreased slightly when using the coated rotor disc. The reason for this could not be identified in this work, but probably requires a detailed study focusing mainly on the optimization of the chosen catalyst and the coating technique. The experiments with the catalyst were merely supposed to be a first feasibility study, if a heterogeneous catalyst could be used and if the immobilization with Nafion® could be a practical coating technique.

Nonetheless, focusing on the results without a catalyst-coated rotor disc, a significant intensification of the epoxidation of MO by means of applying an RSSDR could be observed. In comparison to batch experiments, carried out as benchmark in this study, yield and conversion were distinctly increased by the RSSDR and average reaction rates about $0.14\,\mathrm{mol\,L^{-1}\,min^{-1}}$ were detected for the RSSDR being four times the ones measured for the batch benchmark experiments. The average reaction rates of the RSSDR match and exceed rates of microreactor systems found in literature. Therefore, the presented study in Chapter 5 clearly shows that the epoxidation of MO with hydrogen peroxide and formic acid carried out in an RSSDR in a semi-batch recycle mode is significantly intensified in comparison to batch reactors. In contrast to microreactor systems, which show comparable reaction rates, the RSSDR allows larger throughputs. However, in order

to use this advantage, the operational mode applied in this study in order to allow easy procedure of a parameter study should be changed to a continuous mode with a split recycle stream. Then, the influence of the reactor throughput could also be investigated further, as in this study superimposed influences of the flow conditions in the RSSDR, the peripheral tubing and residence time in the batch vessel, which influences the demixing of the oil and water phase, could only be examined. In case a continuous operational mode is applied, the increased disposal of oil and water phase of course poses a new issue to consider.

Another interesting idea would be to carry out the studied reaction system in an improved RSSDR setup, which allows temperature control up to a maximum rotational disc speed of 4000 min^{-1}. Even though a coolant medium was flowing through the stator housing in the study presented in Chapter 5 in order to control the desired reaction temperature and remove excess heat from the epoxidation reaction, hydrogen peroxide decay and dissipative power input due to rotation, at a certain limiting rotational disc speed the effectiveness of the used RSSDR as a heat exchanger decreased with a further increase in rotational disc speed; this is assumed to cause the decrease in yield and conversion at higher rotational disc speeds. Thus, if maybe a stator-rotor-stator spinning disc reactor with increased heat exchange area and small wall thicknesses could be used so that the maximum effectiveness would be shifted towards higher rotational disc speeds than ca. 1500 min^{-1}, the beneficial effects of good temperature control, fast mixing and mass transfer could be examined separately. However, it should be considered, whether or not it makes sense and whether or not the better mixing at very high rotational disc speeds is worth the effort to further improve an RSSDR setup in terms of its heat exchange effectiveness in order to remove extra heat, which is generated at very high rotational disc speeds.

A Appendix

Parts of the appendix appeared in a similar way in the following publications:

J. Kleiner, B. Münch, F. Rößler, J. Fernengel, F. Habla, O. Hinrichsen, CFD simulation of single-phase heat transfer in a rotor-stator spinning disc reactor. *Chem. Eng. Process.* 131 (2018) 150−160 [106].
Reprint with permission from *Elsevier*.

J. Kleiner, O. Hinrichsen, Epoxidation of methyl oleate in a rotor-stator spinning disc reactor. *Chem. Eng. Process.* 136 (2019) 152−162 [83].
Reprint with permission from *Elsevier*.

A.1 Single-phase stator-side heat transfer in a rotor-stator spinning disc reactor

A.1.1 Empirical correlations for heat loss to the environment

Heat loss to the environment of the studied rotor-stator setups was determined as described in Sections 3.5.2 and 3.6.1. The resulting empirical correlations, which describe the majority of the experimental data within 10 % accuracy, for heat loss to the environment for the small and large setup are given in Equations (A.1) and (A.2).

Small setup

$$\frac{P_{\mathrm{loss}}}{\mathrm{W}}(G = 0.0154) = 3.1848 \left(\frac{T_{\mathrm{R,in}}}{^{\circ}\mathrm{C}} - \frac{T_{\mathrm{amb}}}{^{\circ}\mathrm{C}} \right)^{0.5478} \tag{A.1}$$

Large setup

$$\frac{P_{\text{loss}}}{\text{W}}(G = 0.0074) = 0.4821 \left(\frac{T_{\text{R,in}}}{^\circ\text{C}} - \frac{T_{\text{amb}}}{^\circ\text{C}}\right)^{1.3293} \tag{A.2}$$

A.1.2 Material properties

Coolant medium

Density: Polynomial fitted for data set from VDI Wärmeatlas [148].

$$\frac{\varrho_{\text{C}}}{\text{kg m}^{-3}} = A \left(\frac{\overline{T}_{\text{C}}}{^\circ\text{C}}\right)^3 + B \left(\frac{\overline{T}_{\text{C}}}{^\circ\text{C}}\right)^2 + C \frac{\overline{T}_{\text{C}}}{^\circ\text{C}} + D \tag{A.3}$$

Specific heat at constant pressure: Polynomial fitted for data set from VDI Wärmeatlas [148].

$$\frac{c_{p,\text{C}}}{\text{J kg}^{-1}\,\text{K}^{-1}} = A \left(\frac{\overline{T}_{\text{C}}}{^\circ\text{C}}\right)^3 + B \left(\frac{\overline{T}_{\text{C}}}{^\circ\text{C}}\right)^2 + C \frac{\overline{T}_{\text{C}}}{^\circ\text{C}} + D \tag{A.4}$$

Table A.1: Parameters for the material properties given in Equations (A.3) to (A.4).

Parameter	ϱ_{C}	$c_{p,\text{C}}$
A	$1.64100 \cdot 10^{-5}$	$-1.34877 \cdot 10^{-4}$
B	$-5.99673 \cdot 10^{-3}$	$3.44218 \cdot 10^{-2}$
C	$2.06240 \cdot 10^{-2}$	$-2.11000 \cdot 10^{0}$
D	$1.00002 \cdot 10^{3}$	$4.21490 \cdot 10^{3}$

Reactant medium

Density: Polynomial fitted for data set from the NIST databank and VDI Wärmeatlas [148] and weighted with the respective mass fraction.

$$\begin{aligned}\frac{\varrho_{\text{R}}}{\text{kg m}^{-3}} = &\left(A \left(\frac{\overline{T}_{\text{R}}}{^\circ\text{C}}\right)^3 + B \left(\frac{\overline{T}_{\text{R}}}{^\circ\text{C}}\right)^2 + C \frac{\overline{T}_{\text{R}}}{^\circ\text{C}} + D\right) w_{\text{gly}} \\ &+ \left(E \left(\frac{\overline{T}_{\text{R}}}{^\circ\text{C}}\right)^3 + F \left(\frac{\overline{T}_{\text{R}}}{^\circ\text{C}}\right)^2 + G \frac{\overline{T}_{\text{R}}}{^\circ\text{C}} + H\right) (1 - w_{\text{gly}})\end{aligned} \tag{A.5}$$

Specific heat at constant pressure: Polynomial fitted for data sets from the NIST databank and VDI Wärmeatlas [148] and weighted with the respective mass fraction.

$$\begin{aligned}\frac{c_{p,\mathrm{R}}}{\mathrm{J\,kg^{-1}\,K^{-1}}} = &\left(A\left(\frac{\overline{T}_\mathrm{R}}{^\circ\mathrm{C}}\right)^4 + B\left(\frac{\overline{T}_\mathrm{R}}{^\circ\mathrm{C}}\right)^3 + C\left(\frac{\overline{T}_\mathrm{R}}{^\circ\mathrm{C}}\right)^2 + D\,\frac{\overline{T}_\mathrm{R}}{^\circ\mathrm{C}} + E\right) w_\mathrm{gly} \\ &+ \left(F\left(\frac{\overline{T}_\mathrm{R}}{^\circ\mathrm{C}}\right)^3 + G\left(\frac{\overline{T}_\mathrm{R}}{^\circ\mathrm{C}}\right)^2 + H\,\frac{\overline{T}_\mathrm{R}}{^\circ\mathrm{C}} + I\right)(1 - w_\mathrm{gly})\end{aligned} \tag{A.6}$$

Dynamic viscosity: Polynomials fitted for data sets from the NIST databank for different temperatures and linearly interpolated between those temperatures.

$$\begin{aligned}\frac{\mu_\mathrm{R}}{\mathrm{mPa\,s}} = &\left(A\,x_\mathrm{gly}^5 + B\,x_\mathrm{gly}^4 + C\,x_\mathrm{gly}^3 + D\,x_\mathrm{gly}^2 + E\,x_\mathrm{gly} + F\right) \\ &+ \Big[\left(G\,x_\mathrm{gly}^5 + H\,x_\mathrm{gly}^4 + I\,x_\mathrm{gly}^3 + J\,x_\mathrm{gly}^2 + K\,x_\mathrm{gly} + L\right) \\ &- \left(A\,x_\mathrm{gly}^5 + B\,x_\mathrm{gly}^4 + C\,x_\mathrm{gly}^3 + D\,x_\mathrm{gly}^2 + E\,x_\mathrm{gly} + F\right)\Big] \\ &\Big/ \left(\frac{T_2}{^\circ\mathrm{C}} - \frac{T_1}{^\circ\mathrm{C}}\right)\left(\frac{\overline{T}_\mathrm{R}}{^\circ\mathrm{C}} - \frac{T_1}{^\circ\mathrm{C}}\right)\end{aligned} \tag{A.7}$$

Thermal conductivity: Polynomials fitted for data sets from the NIST databank for different temperatures and linearly interpolated between those temperatures.

$$\begin{aligned}\frac{\lambda_\mathrm{R}}{\mathrm{W\,m^{-1}\,K^{-1}}} = &\left(A\,x_\mathrm{gly}^5 + B\,x_\mathrm{gly}^4 + C\,x_\mathrm{gly}^3 + D\,x_\mathrm{gly}^2 + E\,x_\mathrm{gly} + F\right) \\ &+ \Big[\left(G\,x_\mathrm{gly}^5 + H\,x_\mathrm{gly}^4 + I\,x_\mathrm{gly}^3 + J\,x_\mathrm{gly}^2 + K\,x_\mathrm{gly} + L\right) \\ &- \left(A\,x_\mathrm{gly}^5 + B\,x_\mathrm{gly}^4 + C\,x_\mathrm{gly}^3 + D\,x_\mathrm{gly}^2 + E\,x_\mathrm{gly} + F\right)\Big] \\ &\Big/ \left(\frac{T_2}{^\circ\mathrm{C}} - \frac{T_1}{^\circ\mathrm{C}}\right)\left(\frac{\overline{T}_\mathrm{R}}{^\circ\mathrm{C}} - \frac{T_1}{^\circ\mathrm{C}}\right)\end{aligned} \tag{A.8}$$

Table A.2: Parameters for the material properties given in Equations (A.5) to (A.8).

Parameter	ϱ_R	$c_{p,\mathrm{R}}$	μ_R	λ_R
A	$4.43543 \cdot 10^{-5}$	$3.46000 \cdot 10^{-7}$	$9.69981 \cdot 10^{1}$	$-3.13441 \cdot 10^{0}$
B	$-6.62856 \cdot 10^{-3}$	$-1.71183 \cdot 10^{-4}$	$4.97165 \cdot 10^{1}$	$9.04026 \cdot 10^{0}$
C	$-3.27061 \cdot 10^{-1}$	$2.87369 \cdot 10^{-2}$	$1.12999 \cdot 10^{2}$	$-1.01697 \cdot 10^{1}$
D	$1.26989 \cdot 10^{3}$	$3.70659 \cdot 10^{0}$	$1.29454 \cdot 10^{1}$	$5.86310 \cdot 10^{0}$
E	$1.64100 \cdot 10^{-5}$	$2.26576 \cdot 10^{3}$	$1.03327 \cdot 10^{1}$	$-1.93619 \cdot 10^{0}$
F	$-5.99673 \cdot 10^{-3}$	$-1.34877 \cdot 10^{-4}$	$5.82770 \cdot 10^{-1}$	$6.21780 \cdot 10^{-1}$
G	$2.06240 \cdot 10^{-2}$	$3.44218 \cdot 10^{-2}$	$-1.45720 \cdot 10^{2}$	$-3.04760 \cdot 10^{0}$
H	$1.00002 \cdot 10^{3}$	$-2.11000 \cdot 10^{0}$	$4.14684 \cdot 10^{2}$	$8.91657 \cdot 10^{0}$
I	-	$4.21490 \cdot 10^{3}$	$-2.30502 \cdot 10^{2}$	$-1.01907 \cdot 10^{1}$
J	-	-	$1.05869 \cdot 10^{2}$	$5.96792 \cdot 10^{0}$
K	-	-	$-2.72397 \cdot 10^{0}$	$-1.99650 \cdot 10^{0}$
L	-	-	$6.98560 \cdot 10^{-1}$	$6.35210 \cdot 10^{-1}$
T_1	-	-	$3.98500 \cdot 10^{1}$	$4.00000 \cdot 10^{1}$
T_2	-	-	$4.98500 \cdot 10^{1}$	$5.00000 \cdot 10^{1}$

A.2 CFD simulation of single-phase heat transfer in a rotor-stator spinning disc reactor

A.2.1 Investigation of different turbulence models for fluid flow in rotor-stator cavities

In a preliminary study, in order to find a suitable Reynolds-averaged Navier−Stokes (RANS) turbulence model, the flow in different rotor-stator setups found in literature was simulated using different turbulence models. The methodology was analogous to the simulations of the study described in Chapter 4. Two-dimensional axial symmetry was assumed and, therefore, 5° wedge segments of the regarded setups were meshed using the *blockMesh* utility and simulated using the *simpleFoam* solver from OpenFOAM®. The geometric configurations and material properties were taken from the respective literature references [59]. The simulated data was evaluated appropriately, thus, allowing to compare radial and tangential velocities as well as the dimensionless pressure coefficient C_p (Equation (A.9)) with literature data.

$$C_p = \frac{2\,p}{\varrho\,\Omega^2\,r_{\mathrm{r,o}}^2} - \left[\frac{2\,p}{\varrho\,\Omega^2\,r_{\mathrm{r,o}}^2}\right]_{r/r_{\mathrm{r,o}}=0.92} \tag{A.9}$$

Figures A.1 and A.2 exemplarily show a comparison between the simulated results of this preliminary study and experimental work as well as simulation results with an implemented Reynolds stress model (RSM) by Poncet et al. [59]. Figure A.1 presents a comparison of the radial and tangential velocity profiles across the gap height evaluated at two different radial positions between experiments and simulation data with the implemented RSM from Poncet et al. [59] and the results of this study simulated with different turbulence models. While Figures A.1a and A.1b do not reveal a good agreement between the experimental data and simulation results, where the simulations appear all to predict the same trends for the radial velocity profiles, Figures A.1c and A.1d show good agreement between the experimental data and the simulation results of this study with the *Lien-Leschziner* and the *Launder-Sharma* turbulence model.

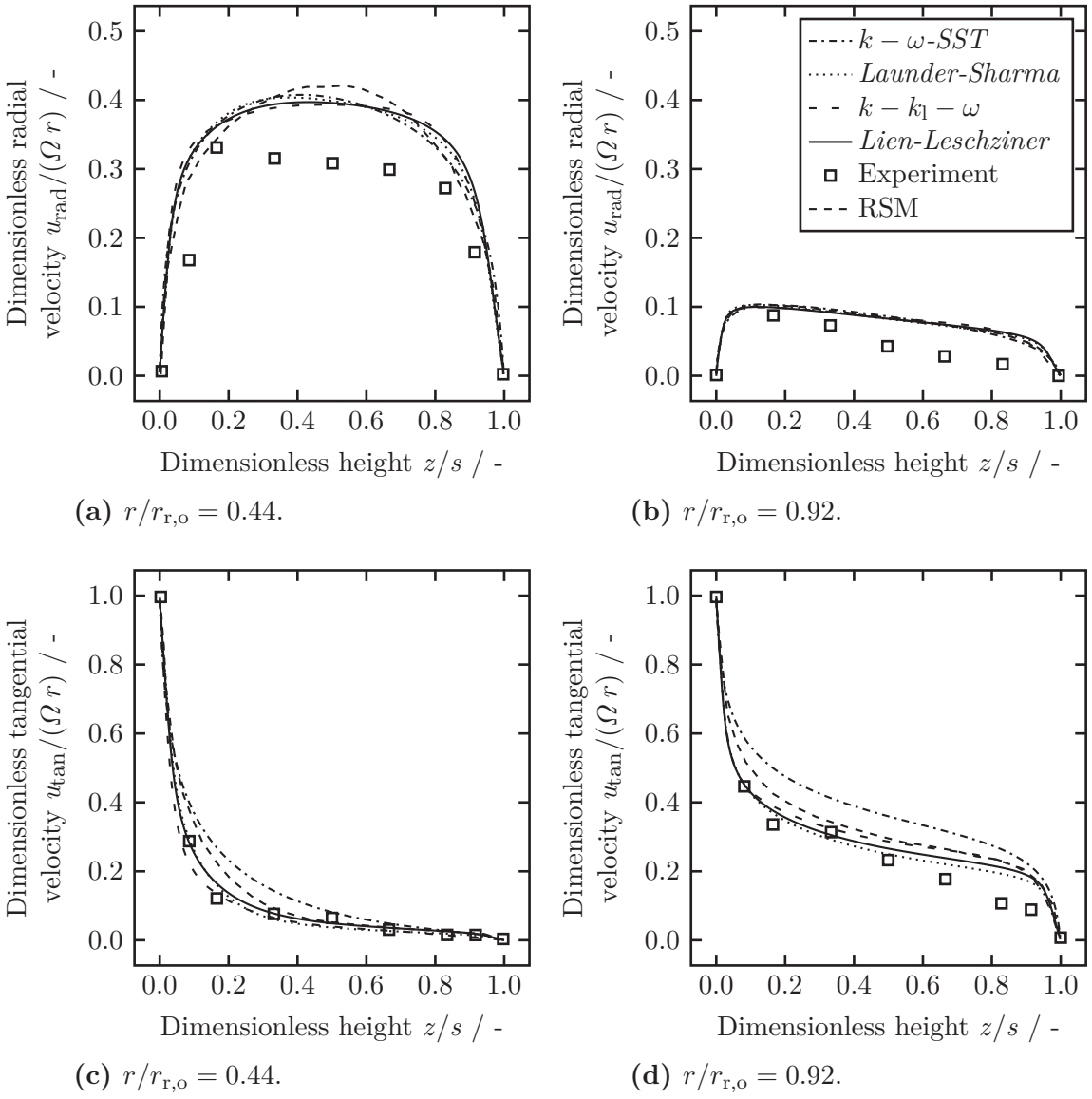

(a) $r/r_{\mathrm{r,o}} = 0.44$. **(b)** $r/r_{\mathrm{r,o}} = 0.92$.

(c) $r/r_{\mathrm{r,o}} = 0.44$. **(d)** $r/r_{\mathrm{r,o}} = 0.92$.

Figure A.1: Dimensionless radial (a) and (b) and tangential (c) and (d) velocity profiles in dependence of dimensionless gap height for $C_W = 5159$, $Re_\Omega = 1.038 \cdot 10^6$ and $G = 0.012$ for two dimensionless radii; the results are from simulations with different turbulence models, which are compared to experimental data as well as RSM simulations from Poncet et al. [59].

In Figure A.2, the dimensionless pressure coefficient in dependence of radial position is illustrated for two configurations with an aspect ratio of $G = 0.012$ for $C_W = 0, Re_\Omega = 4.15 \cdot 10^6$ (Figure A.2a) and $C_W = 2579, Re_\Omega = 4.15 \cdot 10^6$ (Figure A.2b). For the latter two configurations, the simulations with the *Launder-Sharma* model, which showed good agreement for the configuration considered in Figure A.1, did not converge due to instabilities. Hence, this model was omitted from further studies. As can be seen from the data comparison in Figure A.2, the *Lien-Leschziner* turbulence model appears to be most suitable for the description of the experimental results.

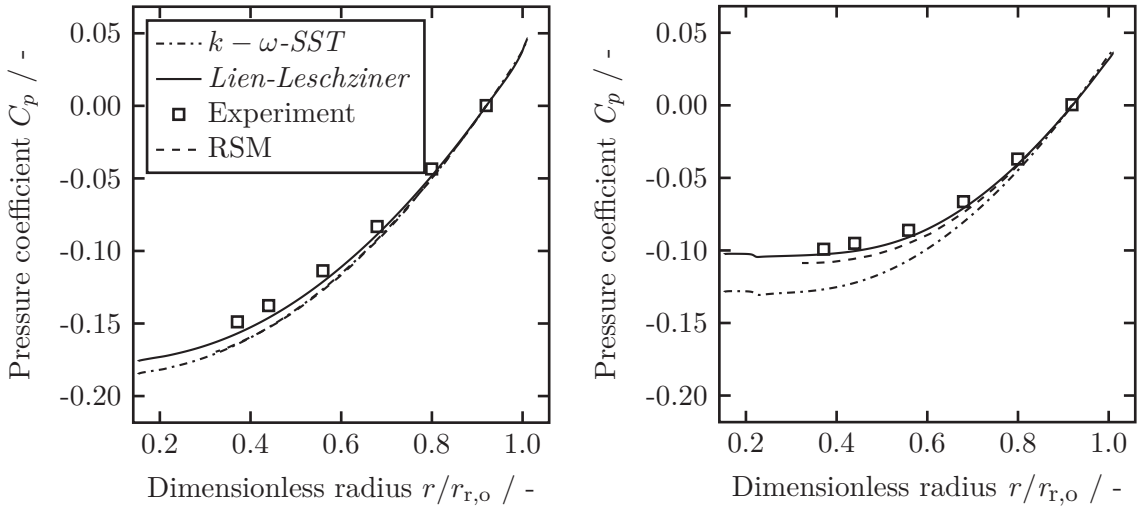

(a) $C_W = 0$, $Re_\Omega = 4.15 \cdot 10^6$. **(b)** $C_W = 2579$, $Re_\Omega = 4.15 \cdot 10^6$.

Figure A.2: Dimensionless pressure coefficient in dependence of dimensionless radius for different dimensionless throughputs for $G = 0.012$; the results are from simulations with different turbulence models, which are compared to experimental data as well as RSM simulations from Poncet et al. [59].

A.2.2 Additional temperature profiles in the upper reactor gap

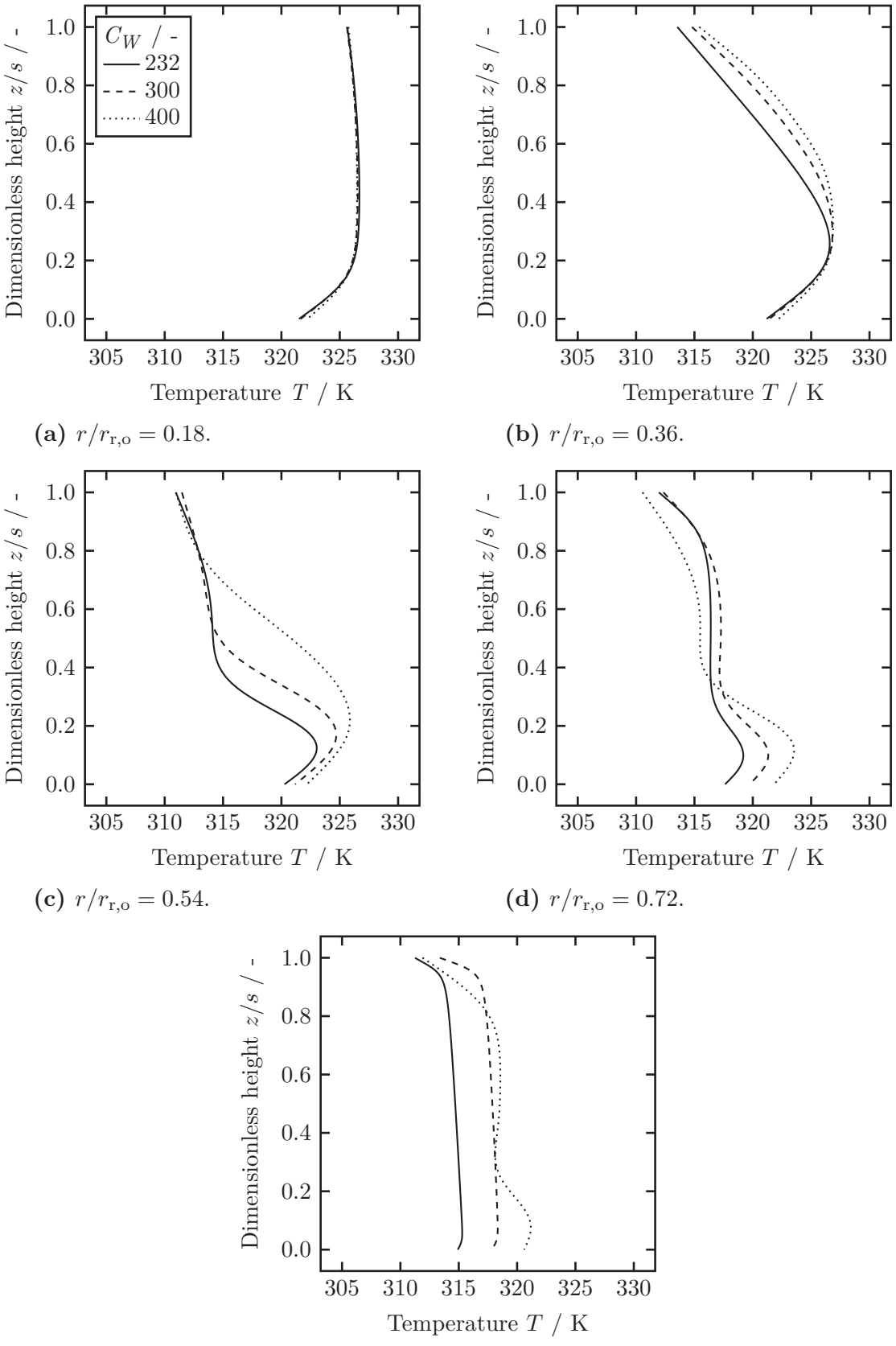

(a) $r/r_{\mathrm{r,o}} = 0.18$.

(b) $r/r_{\mathrm{r,o}} = 0.36$.

(c) $r/r_{\mathrm{r,o}} = 0.54$.

(d) $r/r_{\mathrm{r,o}} = 0.72$.

(e) $r/r_{\mathrm{r,o}} = 0.90$.

Figure A.3: Temperature profiles across the upper reactor gap height at different dimensionless radii for a disc speed of $n = 300\,\mathrm{min}^{-1}$ and three dimensionless throughputs.

A.2.3 Exemplary results from mesh convergence study

Figure A.4 shows radial and axial velocity profiles across the upper reactor gap height at a disc speed of $n = 1000\,\mathrm{min}^{-1}$ ($Re_\Omega \approx 6.83 \cdot 10^5$), a dimensionless throughput of $C_W = 400$ and dimensionless radii of 0.44 and 0.92 for four different cell numbers.

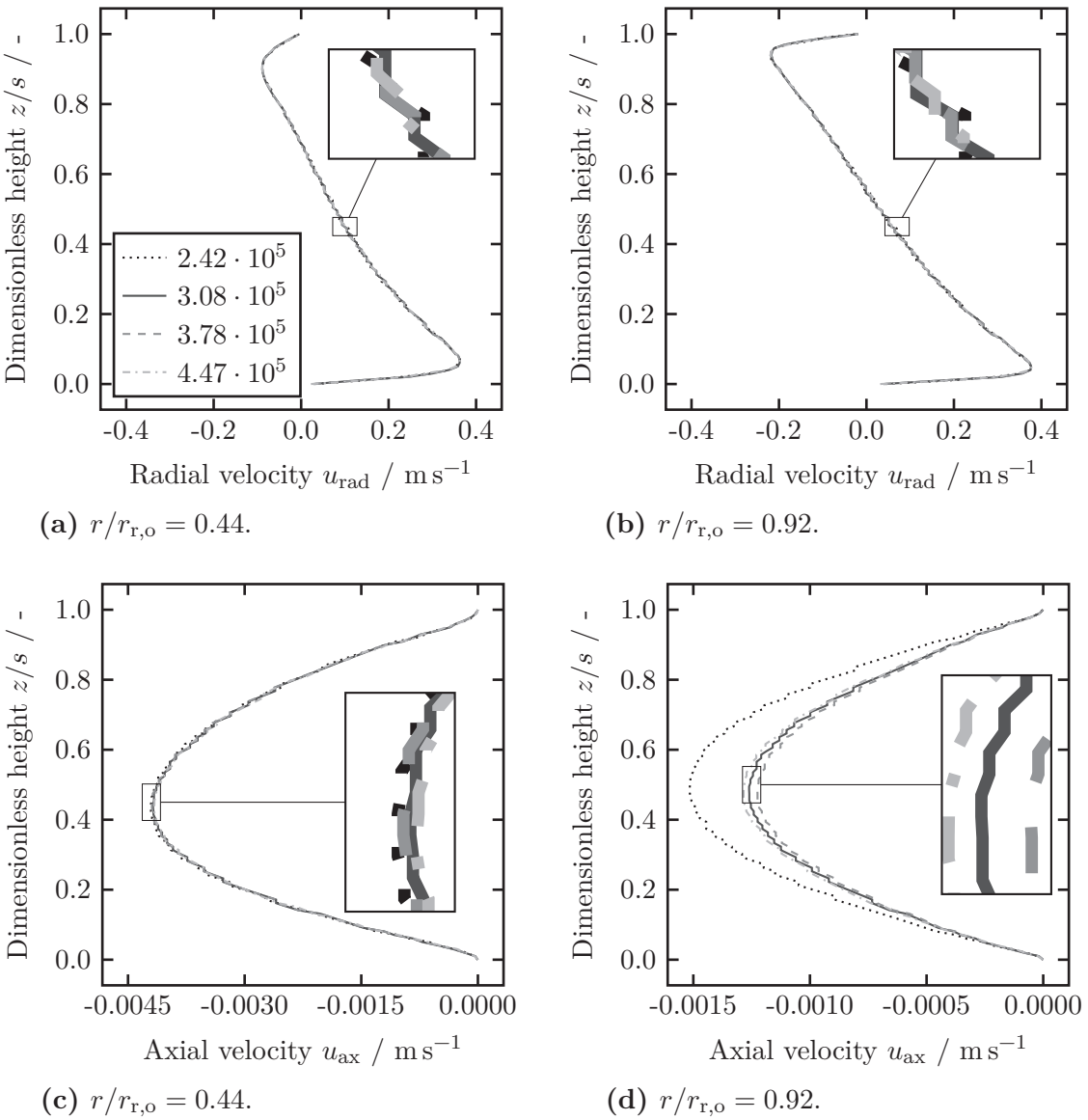

(a) $r/r_{\mathrm{r,o}} = 0.44$. **(b)** $r/r_{\mathrm{r,o}} = 0.92$.

(c) $r/r_{\mathrm{r,o}} = 0.44$. **(d)** $r/r_{\mathrm{r,o}} = 0.92$.

Figure A.4: Radial (a) and (b) and axial (c) and (d) velocity profiles across the upper reactor gap height at a disc speed of $n = 1000\,\mathrm{min}^{-1}$ ($Re_\Omega = 6.83 \cdot 10^5$), a dimensionless throughput of $C_W = 400$ and two dimensionless radii for four different cell numbers.

With regard to the radial velocity profiles, almost no difference of the results with different meshes is visible (cf. Figures A.4a and A.4b). Similar results were obtained for the tangential velocity profiles. Figure A.4d shows that the meshes with cell numbers $3.08{\cdot}10^5$, $3.78{\cdot}10^5$ and $4.47{\cdot}10^5$ slightly differ in the axial velocity profile at a dimensionless radius of 0.92. The results of the mesh with $3.08 \cdot 10^5$ cells are closer to the results of the

finest mesh displayed in Figure A.4d. Hence, the mesh with $3.08 \cdot 10^5$ cells was chosen for the reactor gap as best compromise between accuracy and computational resource saving for the computations of the study presented in Chapter 4.

A.3 Epoxidation of methyl oleate in a rotor-stator spinning disc reactor

A.3.1 Exemplary results considering *cis* and *trans* isomers

Figure A.5 shows methyl oleate conversion and yield and selectivity of the epoxidized methyl oleate considering *cis* and *trans* isomers for evaluation of the oil phases of the reaction mixtures in dependence of temperature. The qualitative behavior shown in Figure A.5 is similar to the one in Figure 5.8 (cf. Section 5.4.3). Quantitatively speaking, the single data points of yield and selectivity are slightly higher in Figure A.5 in contrast to Figure 5.8, which is expected, as not only the *cis* educt and the more likely *cis* product are regarded.

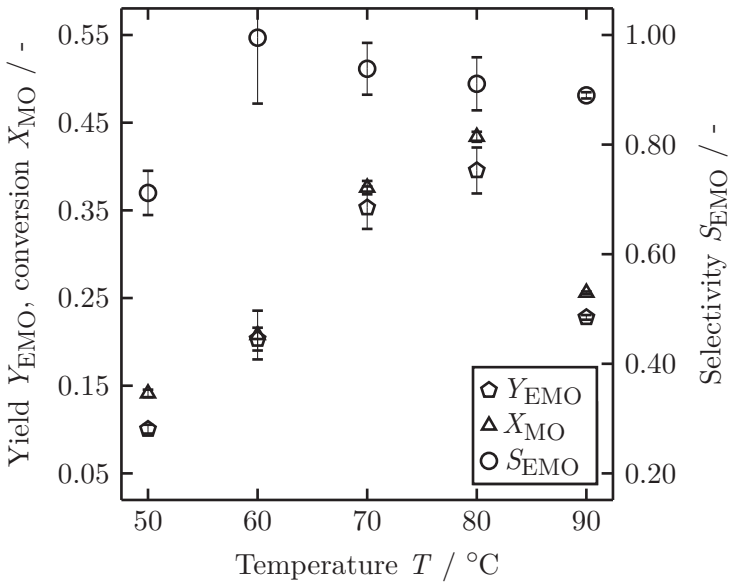

Figure A.5: Conversion of methyl oleate, yield and selectivity of epoxidized methyl oleate in dependence of temperature for a throughput of $\dot{V}_R = 50\,mL\,min^{-1}$ and a rotational disc speed of $n = 500\,min^{-1}$ taking into account *cis* and *trans* isomers.

A.3.2 Calibration data for gas chromatograph analysis

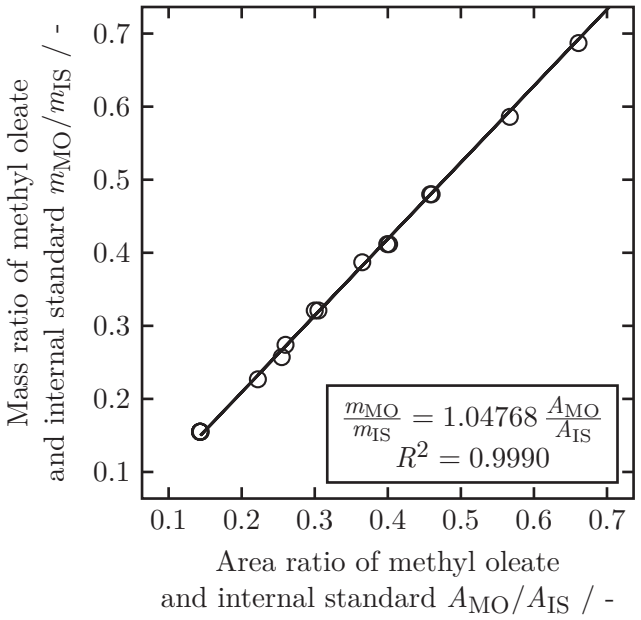

Figure A.6: Calibration data for methyl oleate.

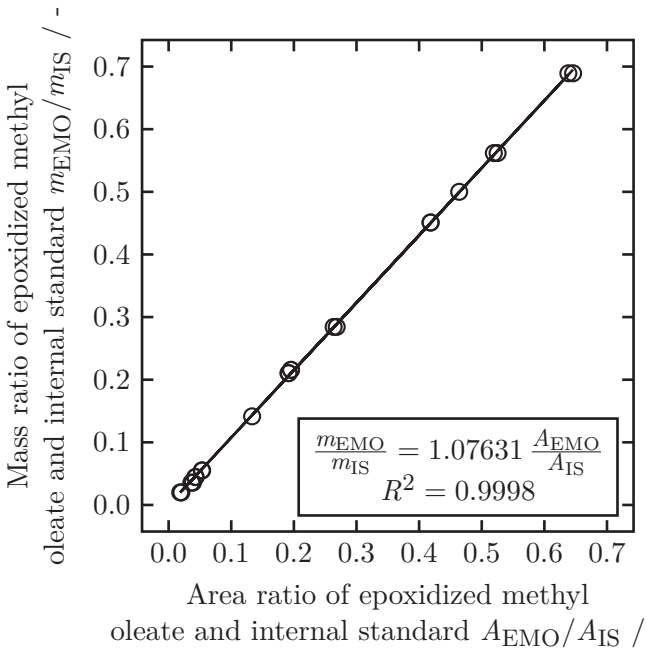

Figure A.7: Calibration data for epoxidized methyl oleate.

B Bibliography

[1] DLR Projektträger / Deutsche IPCC-Koordinierungsstelle. Sonderbericht 1,5 °C globale Erwärmung – SR1.5. Website. https://www.de-ipcc.de/256.php; accessed on 10/18/2018.

[2] R. H. Ahrens. *Das Ziel vor Augen*. VDI nachrichten, 10/12/2018.

[3] Klimakiller als Klimaretter. Website. https://www.tum.de/die-tum/aktuelles/pressemitteilungen/detail/article/31444/; accessed on 10/21/2018.

[4] !nnovA^2 - Innovative Apparate- und Anlagenkonzepte zur Steigerung der Effizienz von Produktionsprozessen. Website. https://www.apt.mw.tum.de/forschung/themen/nnova2/; accessed on 10/21/2018.

[5] Bundesministerium für Bildung und Forschung. Kopernikus-Projekt ENSURE. Website. https://www.kopernikus-projekte.de/projekte/neue-netzstrukturen; accessed on 10/21/2018.

[6] Bundesministerium für Bildung und Forschung. Kopernikus-Projekt P2X. Website. https://www.kopernikus-projekte.de/projekte/power-to-x; accessed on 10/21/2018.

[7] Bundesministerium für Bildung und Forschung. Kopernikus-Projekt SynErgie. Website. https://www.kopernikus-projekte.de/projekte/industrieprozesse; accessed on 10/21/2018.

[8] Bundesministerium für Bildung und Forschung. Kopernikus-Projekt ENavi. Website. https://www.kopernikus-projekte.de/projekte/systemintegration; accessed on 10/21/2018.

[9] F. Haseidl. Weiterentwicklung der Spinning-Disc-Technologie. Ph.D. Thesis. Technische Universität München, 2015.

[10] F. J. Keil. Process intensification. *Rev. Chem. Eng.* 34 (2) (2018) 135–200.

[11] J. J. Klemeš et al. *Process Integration and Intensification*. Berlin: De Gruyter Graduate, 2014.

[12] Working Party on Process Intensification. Website. https://efce.info/Working+Parties/Process+Intensification/Discussion+Forum/EUROPIN.html; accessed on 10/19/2018.

[13] Themes and Projects. Website. https://dechema.de/dechema_eV/en/Research/Research+Promotion+at+DECHEMA/Themes+and+Projects-p-123251.html; accessed on 10/19/2018.

[14] Z. Leszczynski. Role of chemical-engineering and chemical process machinery in industrial application and in process intensification. *Przem. Chem.* 52 (1973) 161–163.

[15] W. T. Cross and C. Ramshaw. Process Intensification: Laminar Flow Heat Transfer. *Chem. Eng. Res. Des.* 64 (1986) 293.

[16] T. Van Gerven and A. Stankiewicz. Structure, Energy, Synergy, Time – The Fundamentals of Process Intensification. *Ind. Eng. Chem. Res.* 48 (5) (2009) 2465–2474. DOI: 10.1021/ie801501y.

[17] A. I. Stankiewicz and J. A. Moulijn. Process Intensification: Transforming Chemical Engineering. *Chem. Eng. Prog.* 1 (2000) 22–34.

[18] EUROPEAN ROADMAP FOR PROCESS INTNSIFICATION. Creative Energy - Energy Transition. Website. https://efce.info/efce_media/-p-531.pdf; accessed on 10/19/2018.

[19] F. Visscher et al. Rotating reactors - A review. *Chem. Eng. Res. Des.* 91 (10) (2013) 1923–1940. DOI: 10.1016/j.cherd.2013.07.021.

[20] Pliny the Elder. *Naturalis Historia: The Elder Pliny's chapters on chemical subjects*. Translated by K. C. Baily. London: Arnold, 1929.

[21] M. M. de Beer et al. Single phase fluid-stator heat transfer in a rotor-stator spinning disc reactor. *Chem. Eng. Sci.* 119 (2014) 88–98.

[22] M. Meeuwse, J. van der Schaaf and J. C. Schouten. Mass Transfer in a Rotor-Stator Spinning Disk Reactor with Cofeeding of Gas and Liquid. *Ind. Eng. Chem. Res.* 49 (4) (2010) 1605–1610. DOI: 10.1021/ie901301m.

[23] F. Haseidl, P. Schuh and K. O. Hinrichsen. Further Development and Characterization of a Rotor-Stator Spinning Disc Reactor. *Chem. Ing. Tech.* 87 (6) (2015) 830–836. DOI: 10.1002/cite.201400136.

[24] A. N. Manzano Martinez et al. Micromixing in a Rotor-Stator Spinning Disc Reactor. *Ind. Eng. Chem. Res.* 56 (45) (2017) 13454–13460. DOI: 10.1021/acs.iecr.7b01324.

[25] M. Meeuwse et al. Liquid-Solid Mass Transfer and Reaction in a Rotor-Stator Spinning Disc Reactor. *Ind. Eng. Chem. Res.* 49 (21) (2010) 10751–10757. DOI: 10.1021/ie1003366.

[26] M. Meeuwse et al. Gas-liquid mass transfer in a rotor-stator spinning disc reactor. *Chem. Eng. Sci.* 65 (1) (2010) 466–471. DOI: 10.1016/j.ces.2009.06.006.

[27] M. Meeuwse et al. Effect of rotor-stator distance and rotor radius on the rate of gas-liquid mass transfer in a rotor-stator spinning disc reactor. *Chem. Eng. Process.* 50 (10) (2011) 1095–1107. DOI: 10.1016/j.cep.2011.05.022.

[28] F. Haseidl, J. Pottbäcker and O. Hinrichsen. Gas–Liquid mass transfer in a rotor–stator spinning disc reactor: Experimental study and correlation. *Chem. Eng. Process.* 104 (2016) 181–189. DOI: 10.1016/j.cep.2016.03.003.

[29] M. M. de Beer et al. Intensification of convective heat transfer in a stator-rotor-stator spinning disc reactor. *AIChE J.* 61 (7) (2015) 2307–2318.

[30] M. M. de Beer et al. Forced convection boiling in a stator-rotor-stator spinning disc reactor. *AIChE J.* 62 (10) (2016) 3763–3773.

[31] M. M. de Beer et al. Engineering model for single-phase flow in a multi-stage rotor-stator spinning disc reactor. *Chem. Eng. J.* 242 (2014) 53–61.

[32] S. Phimsen et al. Epoxidation of methyl oleate in a TiO_2 coated-wall capillary microreactor. *Chem. Eng. J.* 314 (2017) 594–599. DOI: 10.1016/j.cej.2016.12.017.

[33] E. Santacesaria et al. Biphasic Model Describing Soybean Oil Epoxidation with H_2O_2 in Continuous Reactors. *Ind. Eng. Chem. Res.* 51 (26) (2012) 8760–8767. DOI: 10.1021/ie2016174.

[34] S. Dinda et al. Epoxidation of cottonseed oil by aqueous hydrogen peroxide catalysed by liquid inorganic acids. *Bioresour. Technol.* 99 (9) (2008) 3737–3744. DOI: 10.1016/j.biortech.2007.07.015.

[35] W. He et al. Epoxidation of Soybean Oil by Continuous Micro-Flow System with Continuous Separation. *Org. Process Res. Dev.* 17 (9) (2013) 1137–1141. DOI: 10.1021/op400050n.

[36] M. Guidotti et al. Epoxidation of unsaturated FAMEs obtained from vegetable source over Ti(IV)-grafted silica catalysts: A comparison between ordered and non-ordered mesoporous materials. *J. Mol. Catal. A: Chem.* 250 (1) (2006) 218–225. DOI: 10.1016/j.molcata.2006.01.032.

[37] J. Sepulveda, S. Teixeira and U. Schuchardt. Alumina-catalyzed epoxidation of unsaturated fatty esters with hydrogen peroxide. *Appl. Catal., A* 318 (2007) 213–217. DOI: 10.1016/j.apcata.2006.11.004.

[38] F. Visscher. Liquid-liquid processes in spinning disc equipment. Ph.D. Thesis. Eindhoven University of Technology, 2013.

[39] M. Meeuwse, J. van der Schaaf and J. C. Schouten. Multistage Rotor-Stator Spinning Disc Reactor. *AIChE J.* 58 (1) (2012) 247–255. DOI: 10.1002/aic.12586.

[40] F. Visscher et al. Residence time distribution in a single-phase rotor-stator spinning disk reactor. *AIChE J.* 59 (7) (2013) 2686–2693. DOI: 10.1002/aic.14036.

[41] M. M. de Beer. Hydrodynamics and heat transfer of single and multiphase flows in rotor-stator spinning disc reactors. Ph.D. Thesis. Eindhoven University of Technology, 2016.

[42] F. Haseidl, P. König and O. Hinrichsen. Single-Phase Flow Residence-Time Distributions in a Rotor-Stator Spinning Disc Reactor. *Chem. Eng. Technol.* 39 (12) (2016) 2435–2443. DOI: 10.1002/ceat.201600247.

[43] K. M. P. van Eeten et al. A numerical study on gas–liquid mass transfer in the rotor–stator spinning disc reactor. *Chem. Eng. Sci.* 129 (0) (2015) 14–24. DOI: 10.1016/j.ces.2015.02.020.

[44] M. M. de Beer et al. Bubble formation in co-fed gas–liquid flows in a rotor-stator spinning disc reactor. *Int. J. Multiphase Flow* 83 (2016) 142–152. DOI: 10.1016/j.ijmultiphaseflow.2016.03.013.

[45] F. Visscher et al. Liquid-liquid mass transfer in a rotor-stator spinning disc reactor. *Chem. Eng. J.* 185 (2012) 267–273. DOI: 10.1016/j.cej.2012.01.002.

[46] F. Visscher et al. Water and *n*-Heptane Volume Fractions in a Rotor-Stator Spinning Disc Reactor. *Ind. Eng. Chem. Res.* 51 (51) (2012) 16670–16676. DOI: 10.1021/ie301439s.

[47] F. Visscher et al. Liquid–liquid flow in an impeller–stator spinning disc reactor. *Chem. Eng. Process.* 71 (2013) 107–114. DOI: 10.1016/j.cep.2013.01.015.

[48] J. van der Schaaf et al. Device for multiphase and single phase contacting. Patent. WO/2012/150226 A1. 30/4/2012.

[49] Y. Wang et al. Liquid-liquid extraction in a novel rotor-stator spinning disc extractor. *Sep. Purif. Technol.* 207 (2018) 158–165. DOI: 10.1016/j.seppur.2018.05.053.

[50] M. M. de Beer et al. Convective condensation in a stator-rotor-stator spinning disc reactor. *AIChE J.* 62 (10) (2016) 3784–3796.

[51] S. Jović et al. A new hydrate based process for drying liquids. *Chem. Eng. Res. Des.* 115 (2016) 423–432. DOI: 10.1016/j.cherd.2016.09.015.

[52] S. Jović. Intensification of chlorine processing. Ph.D. Thesis. Eindhoven University of Technology, 2016.

[53] P. Granados Mendoza. Intensification of the chlor-alkali process using a rotor-stator spinning disc membrane electrochemical reactor. Ph.D. Thesis. Eindhoven University of Technology, 2016.

[54] P. Granados Mendoza et al. Intensification of the chlor-alkali process by using a spinning disc membrane electrolyzer. *Chem. Eng. Res. Des.* 128 (2017) 120–129. DOI: 10.1016/j.cherd.2017.10.001.

[55] S. Moshtarikhah. Spinning disc membrane electrolyzer: performance of cation-exchange membrane. Ph.D. Thesis. Eindhoven University of Technology, 2016.

[56] J. M. Owen and R. H. Rogers. *Flow and Heat Transfer in Rotating Disc Systems, Vol.1 : Rotor-Stator Systems*. Taunton, U. K.: Research Studies Press, 1989.

[57] S. Poncet, M. P. Chauve and P. Le Gal. Turbulent rotating disk flow with inward throughflow. *J. Fluid Mech.* 522 (2005) 253–262. DOI: 10.1017/S0022112004002046.

[58] S. Poncet, M. P. Chauve and R. Schiestel. Batchelor versus Stewartson flow structures in a rotor-stator cavity with throughflow. *Phys. Fluids* 17 (7) (2005) 75–110.

[59] S. Poncet, R. Schiestel and M. P. Chauve. Centrifugal flow in a rotor-stator cavity. *J. Fluids Eng.* 127 (4) (2005) 787–794. DOI: 10.1115/1.1949645.

[60] U. Phadke and J. Owen. Aerodynamic aspects of the sealing of gas-turbine rotor-stator systems: Part 1: The behavior of simple shrouded rotating-disk systems in a quiescent environment. *Int. J. Heat Fluid Flow* 9 (2) (1988) 98–105.

[61] T. von Kármán. Über laminare und turbulente Reibung. *Z. Angew. Math. Mech.* 1 (4) (1921) 233–252.

[62] K. Stewartson. On the flow between two rotating coaxial disks. *Math. Proc. Cambridge Philos. Soc.* 49 (1953) 333–341.

[63] G. K. Batchelor. Note on a Class of Solutions of the Navier−Stokes Equations Representing Steady Rotationally-Symmetric Flow. *Q. J. Mech. Appl. Math.* 4 (1951) 29–41.

[64] S. Haddadi and S. Poncet. Turbulence Modeling of Torsional Couette Flows. *Int. J. Rotating Mach.* 347 (2008) 104–108.

[65] J. Daily and R. Nece. Chamber Dimension Effects on Induced Flow and Frictional Resistance of Enclosed Rotating Disks. *J. Fluids Eng.* 82 (1960) 217–230.

[66] U. T. Bödewadt. Die Drehströmung über festem Grunde. *Z. Angew. Math. Mech.* 20 (1) (1940) 241–253.

[67] M. Djaoui, A. Dyment and R. Debuchy. Heat transfer in a rotor-stator system with a radial inflow. *Eur. J. Mech. B-Fluids* 20 (3) (2001) 371–398. DOI: 10.1016/S0997-7546(01)01133-5.

[68] J. M. Lopez. Characteristics of endwall and sidewall boundary layers in a rotating cylinder with a differentially rotating endwall. *J. Fluid Mech.* 359 (1998) 49–79. DOI: 10.1017/S002211209700829x.

[69] J. F. Brady and L. Durlofsky. On Rotating-Disk Flow. *J. Fluid Mech.* 175 (1987) 363–394. DOI: 10.1017/S0022112087000430.

[70] J. Daily and R. Arndt. *Enclosed Rotating Disks with Superposed Throughflow: A Survey of Basic Effects*. Department of Civil Engineering, Massachusetts Institute of Technology, 1962.

[71] H. Iacovides and I. Theofanopoulos. Turbulence modeling of axisymmetric flow inside rotating cavities. *Int. J. Heat Fluid Flow* 12 (1) (1991) 2–11.

[72] H. Schlichting and K. Gersten. *Boundary-Layer Theory*. 9th edition. Berlin Heidelberg: Springer-Verlag, 2017. DOI: 10.1007/978-3-662-52919-5.

[73] S. Poncet and R. Schiestel. Numerical modeling of heat transfer and fluid flow in rotor-stator cavities with throughflow. *Int. J. Heat Mass Transfer* 50 (7-8) (2007) 1528–1544. DOI: 10.1016/j.ijheatmasstransfer.2006.08.028.

[74] J. Owen, C. Haynes and F. Bayley. Heat transfer from an air-cooled rotating disk. *Proc. R. Soc. London, Ser. A* 336 (1607) (1974) 453–473.

[75] R. Boutarfa and S. Harmand. Local convective heat transfer for laminar and turbulent flow in a rotor-stator system. *Exp. Fluids* 38 (2) (2005) 209–221. DOI: 10.1007/s00348-004-0900-5.

[76] J. M. Owen. The effect of forced flow on heat transfer from a disc rotating near a stator. *Int. J. Heat Mass Transfer* 14 (8) (1971) 1135–1147. DOI: 10.1016/0017-9310(71)90209-2.

[77] A. V. Mirzamoghadam and Z. Xiao. Flow and Heat Transfer in an Industrial Rotor-Stator Rim Sealing Cavity. *J. Eng. Gas Turbines Power* 124 (2002) 125–132. DOI: 10.1115/1.1400754.

[78] J. Owen and C. Haynes. Design formulae for the heat loss and frictional resistance of air-cooled rotating discs. *Improvements in fluid machines and systems for energy conversion.* Vol. 4. Milan: Hoepli, 1976.

[79] J. Pellé and S. Harmand. Heat transfer measurements in an opened rotor-stator system air-gap. *Exp. Therm. Fluid Sci.* 31 (3) (2007) 165–180. DOI: 10.1016/j.expthermflusci.2006.03.018.

[80] S. Harmand et al. Review of fluid flow and convective heat transfer within rotating disk cavities with impinging jet. *Int. J. Therm. Sci.* 67 (2013) 1–30. DOI: 10.1016/j.ijthermalsci.2012.11.009.

[81] N. Nikitenko. Experimental investigation of heat exchange of a disk and a screen. *J. Eng. Phys* 6 (6) (1963) 1–11.

[82] L. A. Dorfman. *Hydrodynamic resistance and the heat loss of rotating solids*. Oliver & Boyd, 1963.

[83] J. Kleiner and O. Hinrichsen. Epoxidation of methyl oleate in a rotor-stator spinning disc reactor. *Chem. Eng. Process.* 136 (2019) 152–162. DOI: 10.1016/j.cep.2019.01.004.

[84] T. Laue and A. Plagens. *Namen- und Schlagwort-Reaktionen der Organischen Chemie*. 5th edition. Wiesbaden: Vieweg+Teubner, 2009.

[85] S.-C. Chua, X. Xu and Z. Guo. Emerging sustainable technology for epoxidation directed toward plant oil-based plasticizers. *Process Biochem.* 47 (10) (2012) 1439–1451. DOI: 10.1016/j.procbio.2012.05.025.

[86] L. Kürti and B. Czakó. *Strategic Applications of Named Reactions in Organic Synthesis*. Amsterdam: Elsevier, 2005.

[87] J. Clayden, N. Greeves and S. Warren. *Organic Chemistry*. 2nd edition. New York: Oxford University Press Inc., 2012.

[88] T. S. Omonov, E. Kharraz and J. M. Curtis. The epoxidation of canola oil and its derivatives. *RSC Adv.* 6 (95) (2016) 92874–92886. DOI: 10.1039/C6RA17732H.

[89] M. Guidotti et al. Epoxidation of methyl oleate with hydrogen peroxide. The use of Ti-containing silica solids as efficient heterogeneous catalysts. *Green Chem.* 13 (7) (2011) 1806–1811. DOI: 10.1039/C1GC15151G.

[90] J. C. de Haro et al. Modelling the epoxidation reaction of grape seed oil by peracetic acid. *J. Cleaner Prod.* 138 (2016) 70–76. DOI: 10.1016/j.jclepro.2016.05.015.

[91] J. Kleiner, F. Haseidl and O. Hinrichsen. Rotor-Stator Spinning Disc Reactor: Characterization of the Single-Phase Stator-Side Heat Transfer. *Chem. Eng. Technol.* 40 (11) (2017) 2123–2133. DOI: 10.1002/ceat.201700422.

[92] C. Ramshaw. Process Intensification - a Game for N Players. *Chem. Eng. (London)* (416) (1985) 30–33.

[93] C. Ramshaw. Process intensification and Green Chemistry. *Green Chem.* 1 (1) (1999) G15–G17. DOI: DOI10.1039/gc990g15.

[94] V. Shchukin and V. Olimpiev. Heat transfer of disc rotating in a housing with transitional and turbulent boundary layers. *Soviet Aeronautics* 18 (1975) 77–81.

[95] D. A. Howey, A. S. Holmes and K. R. Pullen. Radially resolved measurement of stator heat transfer in a rotor-stator disc system. *Int. J. Heat Mass Transfer* 53 (1-3) (2010) 491–501. DOI: 10.1016/j.ijheatmasstransfer.2009.09.006.

[96] Z. X. Yuan, N. Saniei and X. T. Yan. Turbulent heat transfer on the stationary disk in a rotor-stator system. *Int. J. Heat Mass Transfer* 46 (12) (2003) 2207–2218. DOI: 10.1016/S0017-9310(02)00525-2.

[97] J. Pellé and S. Harmand. Heat transfer study in a rotor-stator system air-gap with an axial inflow. *Appl. Therm. Eng.* 29 (8-9) (2009) 1532–1543. DOI: 10.1016/j.applthermaleng.2008.07.014.

[98] J. M. Owen. The Reynolds analogy applied to flow between a rotating and a stationary disc. *Int. J. Heat Mass Transfer* 14 (3) (1971) 451–460. DOI: 10.1016/0017-9310(71)90163-3.

[99] V. M. Kapinos. Heat transfer from a disc rotating in a housing with a radial flow of coolant. *J. Eng. Phys.* 8 (1) (1965) 35–38. DOI: 10.1007/bf00833673.

[100] J. P. Yu, E. M. Sparrow and E. R. G. Eckert. Experiments on a Shrouded, Parallel Disk System with Rotation and Coolant Throughflow. *Int. J. Heat Mass Transfer* 16 (2) (1973) 311–&. DOI: 10.1016/0017-9310(73)90060-4.

[101] F. Kreith, E. Doughman and H. Kozlowski. Mass and Heat Transfer From an Enclosed Rotating Disk With and Without Source Flow. *J. Heat Transfer* 85 (2) (1963) 153–162. DOI: 10.1115/1.3686038.

[102] S. Soo and N. Princeton. Laminar flow over an enclosed rotating disk. *Trans. ASME* 80 (2) (1958) 287–296.

[103] M. Baerns et al. *Technische Chemie*. 2nd edition. Weinheim: Wiley-VCH, 2013.

[104] H. Iacovides and J. W. Chew. The Computation of Convective Heat-Transfer in Rotating Cavities. *Int. J. Heat Fluid Flow* 14 (2) (1993) 146–154. DOI: 10.1016/0142-727x(93)90022-F.

[105] P. Trambouze and J.-P. Euzen. *Chemical reactors*. Paris: Editions Technip, 2004.

[106] J. Kleiner et al. CFD simulation of single-phase heat transfer in a rotor-stator spinning disc reactor. *Chem. Eng. Process.* 131 (2018) 150–160. DOI: 10.1016/j.cep.2018.07.010.

[107] L. Schouveiler, P. Le Gal and M. P. Chauve. Instabilities of the flow between a rotating and a stationary disk. *J. Fluid Mech.* 443 (2001) 329–350.

[108] A. Cros et al. Effects of wall compliance on the laminar-turbulent transition of torsional Couette flow. *J. Fluid Mech.* 481 (2003) 177–186. DOI: 10.1017/S0022112003003999.

[109] M. Itoh et al. Experiments on Turbulent-Flow Due to an Enclosed Rotating-Disk. *Exp. Therm. Fluid Sci.* 5 (3) (1992) 359–368. DOI: 10.1016/0894-1777(92)90081-F.

[110] L. Elena and R. Schiestel. Turbulence modeling of rotating confined flows. *Int. J. Heat Fluid Flow* 17 (3) (1996) 283–289. DOI: 10.1016/0142-727X(96)00032-X.

[111] R. Debuchy, F. A. Nour and G. Bois. An Analytical Modeling of the Central Core Flow in a Rotor-Stator System With Several Preswirl Conditions. *J. Fluids Eng.* 132 (6) (2010). DOI: Artn061102-110.1115/1.4001576.

[112] K. M. P. van Eeten et al. Boundary layer development in the flow field between a rotating and a stationary disk. *Phys. Fluids* 24 (2012) 33601-1–33601-18.

[113] E. M. Sparrow and J. L. Goldstein. Effect of Rotation and Coolant Throughflow on the Heat Transfer and Temperature Field in an Enclosure. *J. Heat Transfer* 98 (3) (1976) 387–394. DOI: 10.1115/1.3450565.

[114] G. P. Beretta and E. Malfa. Flow and heat transfer in cavities between rotor and stator disks. *Int. J. Heat Mass Transfer* 46 (15) (2003) 2715–2726. DOI: 10.1016/S0017-9310(03)00065-6.

[115] R. Schiestel, L. Elena and T. Rezoug. Numerical Modeling of Turbulent Flow and Heat Transfer in Rotating Cavities. *Numer. Heat Transfer, Part A* 24 (1) (1993) 45–65. DOI: 10.1080/10407789308902602.

[116] B. Launder, S. Poncet and E. Serre. Laminar, Transitional, and Turbulent Flows in Rotor-Stator Cavities. *Annu. Rev. Fluid Mech.* 42 (1) (2010) 229–248. DOI: 10.1146/annurev-fluid-121108-145514.

[117] T. Holzmann. *Mathematics, numerics, derivations and OpenFOAM®*. 4th edition. Leoben: Holzmann CFD, 2017.

[118] C. J. Greenshields. *OpenFOAM User Guide*. 5th edition. The OpenFOAM Foundation, 2017.

[119] F. S. Lien. Computational modelling of 3D flow in complex ducts and passages. Ph.D. Thesis. Manchester University, 1992.

[120] F. S. Lien and M. A. Leschziner. A Pressure-Velocity Solution Strategy for Compressible Flow and Its Application to Shock/Boundary-Layer Interaction Using Second-Moment Turbulence Closure. *J. Fluids Eng.* 115 (4) (1993) 717–725. DOI: 10.1115/1.2910204.

[121] R. Schwarze. *CFD-Modellierung*. Berlin Heidelberg: Springer-Verlag, 2013.

[122] J. H. Ferziger and M. Perič. *Computational Methods for Fluid Dynamics*. 3rd edition. Berlin Heidelberg New York: Springer-Verlag, 2002.

[123] F. Menter, M. Kuntz and R. Langtry. Ten years of industrial experience with the SST turbulence model. *Proceedings of the fourth international symposium on turbulence, heat and mass transfer*. Antalya, Turkey, 2003 625–632.

[124] W. Polifke and J. Kopitz. *Wärmeübertragung: Grundlagen, analytische und numerische Methoden*. 2nd edition. München: Pearson Studium, 2009.

[125] K. M. Parida, M. Sahoo and S. Singha. A novel approach towards solvent-free epoxidation of cyclohexene by Ti(IV)–Schiff base complex-intercalated LDH using H_2O_2 as oxidant. *J. Catal.* 276 (1) (2010) 161–169. DOI: 10.1016/j.jcat.2010.09.012.

[126] A. Campanella, C. Fontanini and M. A. Baltanás. High yield epoxidation of fatty acid methyl esters with performic acid generated in situ. *Chem. Eng. J.* 144 (3) (2008) 466–475. DOI: 10.1016/j.cej.2008.07.016.

[127] P. Granados Mendoza et al. Liquid–solid mass transfer to a rotating mesh electrode in a rotor–stator spinning disc configuration. *Int. J. Heat Mass Transfer* 104 (2017) 650–657. DOI: 10.1016/j.ijheatmasstransfer.2016.08.076.

[128] Y. S. S. Wan et al. 1-Pentene epoxidation in catalytic microfabricated reactors. *J. Catal.* 223 (2) (2004) 241–249. DOI: 10.1016/j.jcat.2003.11.001.

[129] L. Torrente-Murciano et al. Biphasic Epoxidation Reaction in the Absence of Surfactants - Integration of Reaction and Separation Steps in Microtubular Reactors. *ACS Sustainable Chem. Eng.* 4 (6) (2016) 3245–3249. DOI: 10.1021/acssuschemeng.6b00280.

[130] J. M. R. Gallo, I. S. Paulino and U. Schuchardt. Cyclooctene epoxidation using Nb-MCM-41 and Ti-MCM-41 synthesized at room temperature. *Appl. Catal., A* 266 (2) (2004) 223–227. DOI: 10.1016/j.apcata.2004.02.010.

[131] E. Klemm et al. Direct Gas-Phase Epoxidation of Propene with Hydrogen Peroxide on TS-1 Zeolite in a Microstructured Reactor. *Ind. Eng. Chem. Res.* 47 (6) (2008) 2086–2090. DOI: 10.1021/ie071343+.

[132] L. A. Truter et al. TS-1 coated microreactor for selective oxidations. *Appl. Catal., A* 490 (2015) 139–145. DOI: 10.1016/j.apcata.2014.11.019.

[133] D. Kumar and A. Ali. Ti/SiO_2 as a Nanosized Solid Catalyst for the Epoxidation of Fatty Acid Methyl Esters and Triglycerides. *Energy Fuels* 26 (5) (2012) 2953–2961. DOI: 10.1021/ef300127c.

[134] Y. Devrim. Preparation and Testing of Nafion/Titanium Dioxide Nanocomposite Membrane Electrode Assembly by Ultrasonic Coating Technique. *J. Appl. Polym. Sci.* 131 (15) (2014) 40541-1–40541-10. DOI: ARTN4054110.1002/app.40541.

[135] M. Ercelik et al. Investigation of Nafion based composite membranes on the performance of DMFCs. *Int. J. Hydrogen Energy* 42 (4) (2017) 2658–2668. DOI: 10.1016/j.ijhydene.2016.06.215.

[136] B. Seger and P. V. Kamat. Fuel Cell Geared in Reverse: Photocatalytic Hydrogen Production Using a TiO_2/Nafion/Pt Membrane Assembly with No Applied Bias. *J. Phys. Chem. C* 113 (43) (2009) 18946–18952. DOI: 10.1021/jp907367k.

[137] N. Wehkamp et al. Directly deposited Nafion/TiO_2 composite membranes for high power medium temperature fuel cells. *RSC Adv.* 6 (29) (2016) 24261–24266. DOI: 10.1039/C5RA27462A.

[138] M. Wang, D. Guo and H. Li. High activity of novel Pd/TiO_2 nanotube catalysts for methanol electro-oxidation. *J. Solid State Chem.* 178 (6) (2005) 1996–2000. DOI: 10.1016/j.jssc.2005.04.006.

[139] H. Park and W. Choi. Photocatalytic Reactivities of Nafion-Coated TiO_2 for the Degradation of Charged Organic Compounds under UV or Visible Light. *J. Phys. Chem. B* 109 (23) (2005) 11667–11674. DOI: 10.1021/jp051222s.

[140] D. Derawi and J. Salimon. Optimization on Epoxidation of Palm Olein by Using Performic Acid. *E-J. Chem.* 7 (4) (2010) 1440–1448. DOI: 10.1155/2010/384948.

[141] D. M. Tobaldi et al. Fully quantitative X-ray characterisation of Evonik Aeroxide TiO_2 P25®. *Mater. Lett.* 122 (2014) 345–347. DOI: 10.1016/j.matlet.2014.02.055.

[142] J. A. Rodrigues et al. Correlating chemical structure and physical properties of vegetable oil esters. *J. Am. Oil Chem. Soc.* 83 (4) (2006) 353–357. DOI: 10.1007/s11746-006-1212-0.

[143] S. Johan and J. Mats. A study of fatty acid methyl esters with epoxy or alkyne functionalities. *J. Am. Oil Chem. Soc.* 78 (12) (2001) 1191–1196. DOI: 10.1007/s11745-001-0412-y.

[144] M. J. Pratas et al. Densities and Viscosities of Fatty Acid Methyl and Ethyl Esters. *J. Chem. Eng. Data* 55 (9) (2010) 3983–3990. DOI: 10.1021/je100042c.

[145] W. Roetzel and B. Spang. C1: Berechnung von Wärmeübertragern. *VDI-Wärmeatlas*. 11th edition. Berlin Heidelberg: Springer-Verlag, 2013. Chap. C 37–73.

[146] M. Kleiber and R. Joh. D3.1: Flüssigkeiten und Gase. *VDI-Wärmeatlas*. 11th edition. Berlin Heidelberg: Springer-Verlag, 2013. Chap. D 357–464.

[147] M. Kleiber and R. Joh. D1: Berechnungsmethoden für Stoffeigenschaften. *VDI-Wärmeatlas*. 11th edition. Berlin Heidelberg: Springer-Verlag, 2013. Chap. D 139–174.

[148] W. Wagner. Dba: Stoffwerte von Wasser. *VDI-Wärmeatlas*. 10th edition. Berlin Heidelberg: Springer-Verlag, 2006. Chap. D 1–15.

Nomenclature

Latin Symbols

A	Area	m^2
$A - L$	Parameters in polynomials for material properties	-
a	Thermal diffusivity	$\mathrm{m}^2\,\mathrm{s}^{-1}$
a, b, c	Constants	-
C	Constant	$\mathrm{kg}\,\mathrm{m}^{-8/3}\,\mathrm{s}^{-3}$
C_m	Momentum coefficient	-
$\tilde{C}_{\varepsilon 1}, \tilde{C}_{\varepsilon 2}$	Coefficients in ε transport equation	-
$\tilde{C}_\mu$	Coefficient in Boussinesq viscosity relation	-
c	Concentration	$\mathrm{mol}\,\mathrm{L}^{-1}$
c_p	Specific heat at constant pressure	$\mathrm{J}\,\mathrm{kg}^{-1}\,\mathrm{K}^{-1}$
c_{trans}	Parameter in transition radius correlation	-
ΔH_{R}	Reaction enthalpy	$\mathrm{J}\,\mathrm{mol}^{-1}$
h	Specific enthalpy	$\mathrm{J}\,\mathrm{kg}^{-1}$
I	Turbulence intensity	-
i	Counter variable	-
k	Turbulent kinetic energy	$\mathrm{m}^2\,\mathrm{s}^{-2}$
L_{t}	Turbulence length scale	m
l_{n}	Normal distance from wall	m
l_{n}^*	Dimensionless normal distance from wall	-
M	Tip-friction torque	$\mathrm{kg}\,\mathrm{m}^2\,\mathrm{s}^{-2}$
m	Mass	kg
n	Rotational disc/stirrer speed	min^{-1}
P	Power	W
P_k	Production of turbulence energy	$\mathrm{J}\,\mathrm{kg}^{-1}\,\mathrm{s}^{-1}$
P_k'	Turbulent fluctuation of production of turbulence energy	$\mathrm{J}\,\mathrm{kg}^{-1}\,\mathrm{s}^{-1}$
P_{loss}	Heat loss to the environment	W
P_{rot}	Dissipative power input due to rotation	W
$P_{\Delta p}$	Dissipative power input due to pressure drop	W
p	Pressure	Pa

Δp	Pressure drop	Pa
$\dot{Q}_\mathrm{r}$	Heat flow through the rotor	W
$\dot{Q}_\mathrm{s}$	Heat flow through the stator	W
$\dot{q}$	Heat flux	$\mathrm{W\,m^{-2}}$
R_th	Thermal resistance	$\mathrm{K\,W^{-1}}$
r	Radius / radial position	m
r_EMO	Average rate of epoxide production	$\mathrm{mol\,L^{-1}\,min^{-1}}$
S	Selectivity	-
s	Gap height	m
s_i	Height of layer i	m
T	Temperature	K
$\overline{T}$	Mean temperature	K
T^*	Dimensionless temperature	-
t	Time	s
t_reac	Reaction time	s
t_res	Residence time	s
U	Overall heat transfer coefficient	$\mathrm{W\,m^{-2}\,K^{-1}}$
u	Velocity	$\mathrm{m\,s^{-1}}$
$\mathbf{u}$	Velocity vector	$\mathrm{m\,s^{-1}}$
u_τ	Friction velocity	$\mathrm{m\,s^{-1}}$
V	Volume	$\mathrm{m^3}$
$\dot{V}$	Volumetric throughput	$\mathrm{m^3\,s^{-1}}$
w	Mass fraction	-
X	Conversion	-
x	Mole fraction	-
Y	Yield	-
y	Wall-normal coordinate	m
y^+	Dimensionless wall distance	-
z	Axial direction / position	m

Greek Symbols

α	Heat transfer coefficient	$\mathrm{W\,m^{-2}\,K^{-1}}$
α_loc	Local heat transfer coefficient	$\mathrm{W\,m^{-2}\,K^{-1}}$
γ	Shear rate	$\mathrm{s^{-1}}$
$\delta_{i,j}$	Kronecker delta	-
ε	Turbulent dissipation	$\mathrm{m^2\,s^{-3}}$
η	Effectiveness	-

λ	Thermal conductivity	$\mathrm{W\,m^{-1}\,K^{-1}}$
μ	Dynamic viscosity	$\mathrm{Pa\,s}$
ν	Kinematic viscosity	$\mathrm{m^2\,s^{-1}}$
ν_t	Kinematic eddy viscosity	$\mathrm{m^2\,s^{-1}}$
ϱ	Density	$\mathrm{kg\,m^{-3}}$
τ	Shear stress	Pa
$\boldsymbol{\tau}_{i,j}$	Reynolds stress tensor	$\mathrm{m^2\,s^{-2}}$
Ω	Angular velocity	$\mathrm{rad\,s^{-1}}$
ω	Specific rate of dissipation	$\mathrm{s^{-1}}$

Subscript

air	Air
alu	Aluminum alloy
b	Bulk
bc	Boundary condition for rotor and inlet in study of Poncet et al. [73]
C	Coolant
c	Coolant side
crit	Critical
EMO	Epoxidized methyl oleate
eff	Effective
gly	Glycerol
IS	Internal standard
i	Inner
in	Inlet
l	Lower
limit	Limit
liq	Liquid
MO	Methyl oleate
Nf	Nafion®
o	Outer
out	Out
R	Reactant
r	Rotor
rad	Radial
s	Stator
sol	Solid
steel	Steel

TiO_2	Titanium dioxide
tan	Tangential
trans	Transition
u	Upper
water	Water
0	Initial condition
1	Lower boundary for linear interpolation
2	Upper boundary for linear interpolation

Dimensionless Numbers

C_p	Dimensionless pressure coefficient
C_W	Dimensionless throughput
G	Aspect ratio / gap ratio
Nu	Nusselt number
Nu_{loc}	Local Nusselt number
Pr	Prandtl number
$\overline{Pr}$	Mean Prandtl number
Re_{t}	Local turbulent Reynolds number
Re_{Ω}	Rotational Reynolds number
Ro	Rossby number

Abbreviations

BWR	Batch with recycle
CFD	Computational fluid dynamics
CSTR	Continuous stirred tank reactor
DI	Deionized
EDTA	Ethylenediaminetetraacetic acid
EMO	Epoxidized methyl oleate
FAME	Fatty acid methyl ester
FID	Flame ionization detector
GC	Gas chromatograph
IPCC	Intergovernmental Panel on Climate Change
MO	Methyl oleate

MS	Mass spectrometer
PFR	Plug flow reactor
PI	Process intensification
RANS	Reynolds-averaged Navier−Stokes
RSM	Reynolds stress model
RSSDR	Rotor-stator spinning disc reactor
SDR	Spinning disc reactor
SIMPLE	Semi-implicit method for pressure-linked equations
SRSSDR	Stator-rotor-stator spinning disc reactor
TCD	Thermal conductivity sensor
TS-1	Ti containing silicate-1
2.5D	Two-dimensional axisymmetric

List of Figures

List of Tables

Publications

Journal publications

- J. Kleiner, F. Haseidl, O. Hinrichsen, Rotor-Stator Spinning Disc Reactor: Characterization of the Single-Phase Stator-Side Heat Transfer, *Chem. Eng. Technol.* 40 (11) (2017) 2123−2133.
- J. Kleiner, B. Münch, F. Rößler, J. Fernengel, F. Habla, O. Hinrichsen, CFD simulation of single-phase heat transfer in a rotor-stator spinning disc reactor, *Chem. Eng. Process.* 131 (2018) 150−160.
- J. Kleiner, O. Hinrichsen, Epoxidation of methyl oleate in a rotor-stator spinning disc reactor. *Chem. Eng. Process.* 136 (2019) 152−162.

Conference papers

Oral presentations

- J. Kleiner, F. Haseidl, O. Hinrichsen, Characterization of the single-phase stator-side heat transfer in a rotor-stator spinning disc reactor, 8th Asian-Pacific Chemical Reaction Engineering Symposium (APCRE) 2017, Shanghai, China
- J. Kleiner, O. Hinrichsen, Experimental and theoretical investigation of heat transfer in a rotor-stator spinning disc reactor, Jahrestreffen Reaktionstechnik 2018, Würzburg, Germany

Poster presentations

- J. Kleiner, F. Haseidl, O. Hinrichsen, Charakterisierung des Wärmedurchgangs am Spinning-Disc-Reaktor nach dem Rotor-Stator-Prinzip, Jahrestreffen Reaktionstechnik 2016, Würzburg, Germany
- F. Haseidl, J. Kleiner, P. König, O. Hinrichsen, Single-Phase Flow Residence Time Distribution in a Rotor-Stator Spinning Disc Reactor, 24th International Symposium on Chemical Reaction Engineering (ISCRE) 2016, Minneapolis, USA
- J. Kleiner, F. Haseidl, O. Hinrichsen, Heat Transport in a Rotor-Stator Spinning Disc Reactor, Jahrestreffen Reaktionstechnik 2017, Würzburg, Germany
- J. Kleiner, B. Münch, F. Rößler, J. Fernengel, F. Habla, O. Hinrichsen, Rotor-stator spinning disc reactor: CFD simulation of the heat transfer, Jahrestreffen Reaktionstechnik 2018, Würzburg, Germany
- J. Kleiner, B. Münch, F. Rößler, J. Fernengel, F. Habla, O. Hinrichsen, CFD simulation of hydrodynamics and heat transfer in a rotor-stator spinning disc reactor, 25th International Symposium on Chemical Reaction Engineering (ISCRE) 2018, Florence, Italy

Licensing information

License for Chapter 3

JOHN WILEY AND SONS LICENSE TERMS AND CONDITIONS

Dec 31, 2018

This Agreement between Mrs. Julia Kleiner ("You") and John Wiley and Sons ("John Wiley and Sons") consists of your license details and the terms and conditions provided by John Wiley and Sons and Copyright Clearance Center.

License Number	4499361297057
License date	Dec 31, 2018
Licensed Content Publisher	John Wiley and Sons
Licensed Content Publication	Chemical Engineering & Technology
Licensed Content Title	Rotor-Stator Spinning Disc Reactor: Characterization of the Single-Phase Stator-Side Heat Transfer
Licensed Content Author	Julia Kleiner, Franz Haseidl, Olaf Hinrichsen
Licensed Content Date	Oct 12, 2017
Licensed Content Volume	40
Licensed Content Issue	11
Licensed Content Pages	11
Type of use	Dissertation/Thesis
Requestor type	Author of this Wiley article
Format	Print and electronic
Portion	Full article
Will you be translating?	No
Title of your thesis / dissertation	Reaction engineering and hydrodynamics of a rotor-stator spinning disc reactor
Expected completion date	Jan 2019
Expected size (number of pages)	160
Requestor Location	Mrs. Julia Kleiner Lehrstuhl I für Technische Chemie Technische Universität München Lichtenberstraße 4 Garching, Bavaria 85748 Germany Attn: Mrs. Julia Kleiner
Publisher Tax ID	EU826007151

License for Chapter 4

License for Chapter 5

Declaration

The submitted thesis was supervised by Prof. Dr.-Ing. Kai-Olaf Hinrichsen.

Affirmation

Hereby, I affirm that I am the sole author of this thesis. To the best of my knowledge, I affirm that this thesis does not infringe upon anyone's copyright nor violate any proprietary rights. I affirm that any ideas, techniques, quotations, or any other material, are in accordance with standard referencing practices.

Moreover, I affirm that, so far, the thesis has not been forwarded to a third party nor is it published. I obeyed all study regulations of the Technische Universität München.

Remarks about the internet

Throughout the work, the internet was used for research and verification. Many of the keywords provided herein, references and other information can be verified on the internet. However, no sources are given, because all statements made in this work are fully covered by the cited literature sources.

Garching, September 22, 2019 Julia Kleiner